Boron and nitrogen in diamond: an *ab initio* simulation, plasma emission spectroscopy and material deposition & characterisation study

By

ALEXANDER CROOT

Department of Physics
UNIVERSITY OF BRISTOL

A dissertation submitted to the University of Bristol
in accordance with the requirements of the degree of
DOCTOR OF PHILOSOPHY in the Faculty of Science.

JUNE 2018

Word count: 27328

ABSTRACT

This thesis firstly presents a comprehensive approach to modelling of boron and nitrogen co-dopant clusters in diamond. Using the CRYSTAL14 code, a range of 22 defects comprising up to 5 B and N atoms were studied using a hybrid density functional theory (DFT)-Hartree Fock (HF) level of theory. Results take the form of structures, including symmetry and bond-lengths, formation and binding energies, and finally electrical characteristics derived from density of states spectra. The latter were compared with results of the empirical marker method carried out using the CASTEP DFT code; good agreement was found.

The second part of this work is an optical emission spectroscopy study of diamond chemical vapour deposition (CVD) plasmas. Diborane and nitrogen gases were systematically added firstly to a hydrogen plasma, and then to a hydrogen-methane plasma. Many trends in the relative intensities of the atomic and diatomic emissions were directly relatable to previous studies on individual boron or nitrogen additions to CVD plasmas. When co-introduced, nitrogen suppressed boron-related emissions considerably in the absence of methane, but upon introduction of methane this effect was significantly reduced. The interaction of boron and nitrogen in the gas-phase, undergoing analogous chemistry to carbon, is hypothesised as an explanation. The introduction of carbon to the plasma provides a significant sink for reactive nitrogen-containing species in HCN, thus reducing the suppression of boron-containing species emissions by nitrogen.

A study of diamond CVD and materials characterisation forms the third part of the thesis. Samples were grown with diborane and/or nitrogen on silicon, polycrystalline diamond and single crystal diamond, allowing a range of characterisation techniques with each substrate type. Five gas compositions were used when growing each sample set: low boron+nitrogen, high boron+nitrogen, (and controls) nitrogen, low boron and high boron. Tested properties of the grown films include growth rate, morphology, Raman spectra, dopant concentrations, temperature dependent resistivity and thermionic emission data. Many measured properties are a consequence of the dominant dopant in either the plasma during growth or within the sample. For example the growth rate at high temperature is enhanced upon introduction of nitrogen, but for the same films the majority electrical carriers have boron acceptor-like activation energies. Unexpectedly, a film with boron acceptors as the dominant charge carrier produced a far larger thermionic emission current than one purely doped with nitrogen.

I have a great many people to whom I owe a debt of gratitude. These colleagues and friends have made the past three and a half years a journey I'm proud to have taken. My thanks...

To Dr Neil Fox for the passion that first interested me in a PhD, his valuable supervision and for giving me the opportunity to do the work I've done.

To Prof Mike Ashfold for all his support offered when I've needed it and being happy to humour my ideas. And also to Prof Neil Allan who kindly guided the computational part of my work.

To Drs Zamir Othman and Ben Truscott for mentoring me through my first two PhD years and the many lessons that came alongside. Zamir taught me the value of simplicity in an experiment and that it doesn't have to tell you everything - it telling you anything indicates success. Ben taught me that if you want to do something you should just do it, if you can't then learn how and if you can't learn how then you should pay someone who does it for a living. There are many more.

To Dr James Smith, your knowledge of electronics and all things technical has been invaluable and I feel I learnt as much from you as from anyone. Also thanks to Ed Aldred, for willingly lending either a hand in the lab or an ear to chat to, to Dr Peter Heard for everything to do with SIMS and to Ed Mahoney for all the OES training.

Being in a group for roughly the same length of time as each of its other members gives you the spooky feeling that it's suddenly a whole different group when you reach the end of your time in it. This doesn't mean it felt any different as time progressed and I owe my thanks to every member I've spent time alongside - both academically 'older' and 'younger' members. It has been a great to work with such talented, interesting and fun people. This extends to my project students, truly some of the best (you know who you are). At the risk of sounding cliché, I am probably most proud of the work I've done with others during my years in Bristol.

Finally, to everyone outside of university: my family for asking so many times to finally explain what I'm doing (and of course being so supportive!); my friends for all their support and for showing the exact amount of interest in my work that keeps me both sane and properly distracted from my work outside of work hours; to chem-phys, the bunch, to everyone else - thanks.

AUTHOR'S DECLARATION

I declare that the work in this dissertation was carried out in accordance with the requirements of the University's Regulations and Code of Practice for Research Degree Programmes and that it has not been submitted for any other academic award. Except where indicated by specific reference in the text, the work is the candidate's own work. Work done in collaboration with, or with the assistance of, others, is indicated as such. Any views expressed in the dissertation are those of the author.

SIGNED: .... DATE: ....

TABLE OF CONTENTS

LIST OF ACRONYMS

- CBM . . . . Conduction band minimum

- CRDS . . . . Cavity ring-down spectroscopy

- CVD . . . . Chemical vapour deposition

- DFT . . . . Density functional theory

- DOS . . . . Density of states

- EED . . . . Electron energy distribution

- EMM . . . . Empirical marker method

- GGA . . . . Generalised gradient approximation

- HF . . . . Hot filament or Hartree-Fock

- HPHT . . . . High-pressure high-temperature

- HSE-06 . . . . Heyd-Scuseria-Ernzerhof

- MP . . . . Microwave plasma

- NEA . . . . Negative electron affinity

- OES . . . . Optical emission spectroscopy

- PBE . . . . Perdew-Burke-Ernzerhof

- Ppm . . . . Parts per million

- RT . . . . Room temperature

- SC . . . . Single crystal

- SCF . . . . Self-consistent field

- SEM . . . . Scanning electron microscopy

- SIMS . . . . Secondary ion mass spectrometry

- TE . . . . Thermionic emission

- TVDP . . . . Temperature dependent VDP

- VBM . . . . Valence band maximum

- VDP . . . . Van der Pauw

1

INTRODUCTION

1.1   Diamond and its properties

Popular profound statements such as "a diamond is forever"[i] fail to capture the simplicity and elegance of the diamond tetrahedral bonding structure. The four bonds of each carbon atom, equal in length and angle from one another as shown in figure 1.1, provide diamond with a range of impressive physical and chemical properties. These characteristics include, but are not limited to; the highest known bulk modulus at 440 GPa [8], the highest bulk thermal conductivity at 2 kW m^{-1} K^{-1} and extreme resistance to both chemical and radioactive wear [9, 10]. These properties and others afford diamond a place in both mechanical applications, such as for cutting tools [11] and in electrical applications, such as heat spreaders, sensors and detectors [12, 13].

The advantages of diamond in various situations are somewhat offset by its thermodynamic instability. Unlike in other group 14 elements silicon and germanium, at standard conditions the carbon sp^3 hybridised tetrahedral structure is unstable with respect to the layered sp^2 hybridised hexagonal sheet structure, graphite [14]. Although not insurmountable, a large kinetic barrier lies between diamond and graphite, meaning under appropriate conditions diamond crystals can be synthesised and while they may not be 'forever', they can, with the appropriate preparation, be incorporated into various

---

[i]Named by one advertising company as the 'top' marketing slogan of the 20th century: http://adage.com/article/special-report-the-advertising-century/ad-age-advertising-century-top-10-slogans/140156/
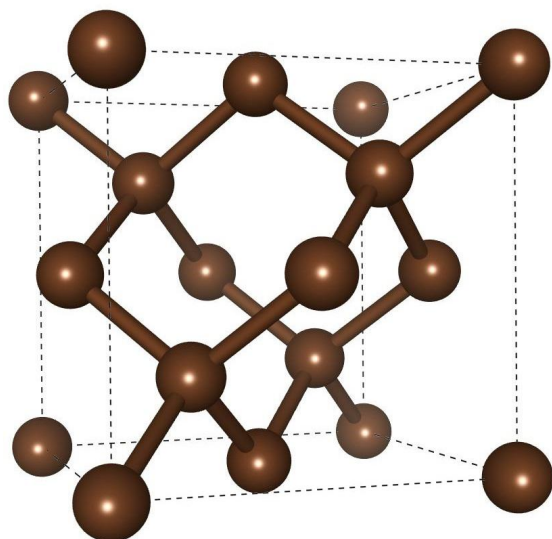
Figure 1.1: The eight atom conventional unit cell of diamond, showing its tetrahedral (1.55 Å) bonding structure.

applications.

1.2 Synthesis of diamond

1.2.1 High pressure-high temperature synthesis

Before the mid 20th century the only successful synthesis of diamond was by naturally occurring processes such as the high temperatures and pressures in the Earth's mantle. Researchers from General Electric were the first to emulate this process, turning various forms of carbon into diamond in its area of stability on the carbon temperature-pressure phase diagram [15, 16].

Upwards of 10^4 atm and 1500 °C are often used in mechanical presses to stabilise diamond during this high pressure-high temperature (HPHT) method. HPHT allows synthesis of crystals ranging from nm to mm in size and is commonly used to produce diamond for both mechanical applications and the gemstone industry.

Since nitrogen is so abundant in the air surrounding common HPHT processes, it is often incorporated into the diamond lattice (replacing carbon) with concentrations on the order of 100 ppm [17], a somewhat alterable number through variation of conditions such as the metal-based carbon solvent used. Different HPHT process conditions leave the incorporated nitrogen in a range of states [18], with common conditions[ii] resulting in high C-centre, or single substitutional nitrogen, concentrations. Other defects such as A-centres (a nitrogen pair) and B-centres (a vacancy surrounded by four nitrogen atoms)

[ii]Such as those used to produce commercial HPHT diamond substrates

can also be synthesised dependent on the growth or annealing temperature and pressure [19].

The main drawback of HPHT diamond synthesis is limited control of the properties of the resulting material. Size, shape and incorporation of impurities are all desirable characteristics for applications beyond those that make use of its extreme hardness and desirable appearance.

1.2.2 Chemical vapour deposition

Whilst HPHT allows synthesis in the diamond-stable part of the carbon phase diagram, chemical vapour deposition (CVD) produces the material in a meta-stable region. First demonstrated at a similar time to HPHT synthesis [20], CVD synthesis was far from ubiquitous in diamond production until advances during the 1980s saw faster growth rates and greater research focus on the method [21]. In the present day, CVD can produce films of diamond with rates and properties dictated by the process conditions during growth.

The CVD process is described further in section 2.2, but briefly: hydrogen and (usually) methane gases are passed over a substrate upon which diamond is to be grown; high temperature activation decomposes hydrogen into H atoms, which in turn break down methane into various species including methyl radicals. These radicals deposit on the surface of the substrate provided there is a free site to bond with - usually created by H abstraction. Graphitic carbon has a lower barrier to reaction with H atoms [22]; so hydrogen also works to etch unwanted sp^2 phases from the produced material, making it possible to grow diamond under conditions where it is unstable with respect to graphite. The conditions used are often pressure < 0.3 atm with thermal gas-activation and substrate temperatures of ~ 2500 °C and 800 - 1000 °C respectively. Possible substrates include metals, silicon and diamond itself.

Gas activation, the driving force behind diamond CVD, can be achieved by various means, with the current two most common methods being hot filament (HF) and microwave plasma (MP). Each has advantages over the other, with HF-CVD usually having cheaper apparatus, the capability to grow over larger areas and running at lower power per substrate area. MP-CVD is advantageous owing to higher growth rates, easily detected species presence thanks to intrinsic plasma emission and an optically detectable substrate temperature owing to lack of nearby filament black-body emission.

The key advantage of CVD is control over the producible material properties, such as size, orientation and impurity concentration, as well as the possibility to grow thin films.

3

HPHT, however, is still of relevance to the production and processing of diamond and this thesis contains results pertaining to both methods.

1.3   Diamond in electronics

Various properties of diamond make it attractive for electronic applications, such as the combination of its unmatched thermal conductivity and enormous resistivity ($\geq 10^{13}$ Ω cm) for use in spreading heat in electronic devices. Its high electron saturation velocity and electric breakdown field make diamond a potential material for both high frequency and high voltage electronic applications [23].

A large (5.47 eV at standard conditions) band-gap gives diamond a very low background current when used in devices such as radiation detectors and electrochemical sensors. Applicability to the latter is also enhanced by the broad potential window under which diamond does not decompose solvents, as well as its resistance to chemical corrosion [24].

1.3.1   Boron doped diamond

The normally insulating diamond lattice can be made impure (or doped) with foreign elements such as boron, which sits to the left of carbon on the periodic table. Boron is an electron acceptor dopant, either introducing holes into the valence band or constituting its own impurity band just above the valence band maximum (VBM) dependent on its concentration. This p-type boron doping induces vastly increased conductivity, facilitating many of the promising electronic applications, not just in electrochemistry [25], but also as part of devices such as nuclear batteries [26].

Boron is well characterised as a dopant able to replace carbon during diamond growth, both by HPHT [27] and CVD [28], and post-growth by ion-implantation [29]. Many researchers have found, from performing temperature-dependent resistivity measurements, that the boron acceptor level lies 0.37 eV above the diamond VBM. Whilst this level is relatively deep compared with many semiconductor acceptor states (c.f. Si acceptor level of B is 0.08 eV above VBM [30]), it is shallow enough to induce semiconducting, metallic and even superconducting properties [31] as B concentration increases and its mid-gap acceptor level broadens.

1.3.2 Nitrogen and other donor dopants

Unlike boron, nitrogen (sitting to the right of carbon) is not a particularly useful electrical impurity. A deep electron donor level, 1.7 eV below the conduction band minimum (CBM) [32], makes the n-type characteristics of nitrogen essentially useless for any diamond device operating close to room temperature. This does not stop it from playing a role in the electrical characteristics of diamond, with N impurities able to compensate[iii] intrinsic acceptors and reduce the conductivity of otherwise undoped material [33]. Nitrogen is incorporable during both HPHT and CVD diamond growth [34, 35], but at present the resulting n-type material has few clear advantages for room-temperature electronics. The nearest neighbour nitrogen-vacancy (NV) centre has found use in various applications owing to its optical and spin properties [36], but has no better semiconductor properties than substitutional N.

Hydrogen-terminated diamond has a negative electron affinity (NEA) [37], meaning its bulk CBM lies above the energy level of a resting electron in vacuum. When doped with a donor element there will be an abundance of conduction band electrons with little to no energetic barrier to emission into vacuum. Collection of these thermionic emission electrons could form the basis of a heat-to-electrical energy converter capable of using renewable or waste heat to produce power [38]. Diamond is a suitable material for this type of device owing to its large band-gap, but requires (amongst other things) an n-type donor capable of introducing sufficient electrons to the conduction band for the device to operate at high currents [39, 40].

Thermionic emission is just one potential application of n-type diamond that requires a donor with an electrical level closer to the CBM. Others include the aforementioned radiation detectors and batteries (which would be made more simply), vacuum-UV emitting diodes, high-speed transistors and power devices.

Phosphorus sits below nitrogen on the periodic table and consequently has a lower electronegativitiy, making it the next obvious candidate for a shallow donor. Unfortunately, its donor level is only 0.6 eV below the CBM [41], making it less than perfect for room temperature electronics. The high temperature thermionic emission properties of phosphorus doped diamond (PDD) are potentially advantageous [40] compared to those of NDD, but no comparative study has been made. Other candidate substitutional donors include As [42], O [43, 44] and S [45], none of which have proven suitable for n-type doping. In an interstitial position, Li has been predicted to be a shallow donor

---

[iii]Compensation happens when electrons from donor levels in the band-gap drop to a lower acceptor level, thereby eliminating the potential of either to accommodate charge from their nearby bulk band.

[46], but attempts to dope diamond in this way have been unable to avoid either lithium aggregation or lithium substituting for carbon, where it introduces a compensating acceptor level [47, 48].

1.3.3 Co-doping

With no promising individual candidate n-type dopants, various researchers have predicted or attempted to use combinations of elements in an effort to make donor characteristics.

Theoretically, the clusters BN_2 [49], AlN_2 [50], HN_2 [51], Si_4N [52], LiN_4 [53] and MgN_3 [54] all provide donor levels shallower than that of nitrogen and some even shallower than phosphorus. Despite this, with the exception of the latter, the aforementioned studies made no attempt to produce the co-doped material. Moreover, clusters that are considered donors can in fact be less energetically favourable than other stoichiometrically equal clusters with a different atomic arrangement [55]. Considering this fact, when predicting co-dopant properties theoretically, it is imperative to consider the potential range of structures that two dopants can make.

On the experimental front, various attempts have been made to introduce two dopants either during or after CVD. Doping with lithium whilst growing diamond is possible [56] and some effort has been made to co-dope it with other elements like boron [57, 58], but with nitrogen Li has only been introduced post-growth by diffusion [59]. A boron-sulphur combination has been attempted [60, 61] based on the hypothesis that boron may increase the incorporation efficiency[iv] of sulphur during CVD, but although n-type characteristics were shown, seemingly favourable results were likely due to lattice defects (not sulphur) and could not be produced consistently. Co-implantation of boron and phosphorus produced apparently n-type behaviour in some material [62] but the results were similarly irreproducible. Phosphorus has also been combined with nitrogen [63, 64], but doing so produced no measured n-type conduction despite good incorporation of phosphorus. Diffusion of deuterium into grown boron-doped single crystals produced n-type material [65], but without further success after the initial experiments.

There is a large gap between the wealth of predicted donor complexes and studies showing successful production of the same defects. Even complexes with large binding energies may never form, due at least in part to an inability to diffuse even light elements through the tightly packed diamond lattice at non-graphitising temperatures [66].

[iv]Defined as the ratio between atomic concentration in the feed gas and atomic concentration in the material, usually expressed as a percentage

In order to overcome this problem, either growth or treatment by HPHT is possible since at such high temperatures dopants can be mobile and the sp^3 phase is stabilised. Nitrogen aggregation (for example) is possible [19], even for samples grown by CVD and subsequently treated by HPHT [35], facilitating control of both dopant concentrations and their ability to form multi-atom complexes within the material. This requires controllable doping during CVD with multiple elements from the gas phase.

Since co-doping has seen such limited success experimentally, little research has focused on examining the effect of combinations of elemental additions to CVD feed gases. The most common elements added (often within some compound) to carbon-hydrogen gas mixtures are argon, boron and nitrogen, with the former not considered a dopant *per se*. Oxygen can also be added, either in the form of O_2 [67] or CO_2 [68], but is thought not to incorporate readily. Oxygen also interacts strongly with boron-containing precursors [69], forming boron oxides and making it unfeasible to introduce both O and B during CVD. While some of the co-doping studies discussed above do use two dopant-containing precursor gases for diamond growth, the characterisation of the gas phase composition is limited. Simple measurements of dopant-related emissions by optical emission spectroscopy (OES) could provide insight into how multiple dopants might interact in the plasma prior to incorporation.

1.4 Combined boron and nitrogen

As the two most commonly used elements for doping diamond, boron and nitrogen make a perfect starting point for studies of co-doping. Not only this, but many diamond growers will experience the potentially unintentional co-introduction of B and N during diamond growth: some level of nitrogen is almost unavoidable in both HPHT and CVD synthesis even when boron doping; and in many reactors boron contamination is near permanent, ensuring any introduction of nitrogen will be accompanied by at least residual boron.

Beyond their unwanted co-introduction, various previous studies examine the combination of boron and nitrogen in diamond. Understandably, compensation of acceptors by nitrogen has been well studied, both those of intrinsic [33] and boron-related [70–72] defects. Luminescence experiments can detect transitions between donors and acceptors in boron doped and boron-nitrogen co-doped material [73, 74], confirming that direct electronic interaction between the two is possible.

A defect containing both boron and nitrogen was identified in electron irradiated boron-doped diamond as a [BN]$^+$ defect, positioned with the B-N bond on a lattice site

[75]. This so called split (100) interstitial appears to be energetically favoured over other less crowded interstitial positions. Defects such as this can be further examined by electronic structure theory calculations such as those using density functional theory (DFT) [76], much like those of the BN_2 donor calculations mentioned previously [49]. Hu et al. [77] have performed calculations on clusters of boron and nitrogen atoms, but the work has limitations that will be discussed further in chapter 3.

Boron and nitrogen have been shown to dope diamond both during HPHT [78] and CVD [79–81] synthesis, with the latter method causing favourable characteristics such as a widened working potential window for electrochemical electrodes [79, 80] and increased strength after high temperature annealing [81] compared to material not doped with both elements.

Nitrogen- and boron-containing gases, introduced to growing diamond during HF-CVD, can counteract the other in some of their detrimental morphological effects [82]. For example nitrogen additions were found by Hartmann et al. [82] to stabilise diamond growth where otherwise high levels of boron-containing gas caused sp^2 carbon formation. Unfortunately the co-introduction of B and N reduced deposition rates. This effect was confirmed by Sartori et al. [83, 84], who found that introduction of ~ 1 gas-phase B atom per 1000 N atoms suppresses the well-known nitrogen-related growth rate enhancement of MP-CVD diamond [85]. This idea is explored further in chapters 4 and 5.

1.5 Outline of the thesis

Despite numerous studies in the past, there are still unanswered questions regarding boron and nitrogen in diamond.

Theoretical (DFT) studies often examine only one defect, ignoring the potential plethora of structures two dopants might form within the material. This idea has been somewhat explored before, showing that the more energetically favourable of two stoichiometrically equal clusters of boron and nitrogen would compensate the other, more attractive (donor) one [55]. Nevertheless, work like this has been limited firstly to small clusters (≤ 3 atoms) and secondly to those potentially forming donors. To build upon this work, a theoretical study of boron-nitrogen clusters would expand the number of atoms and also examine boron-rich clusters - those likely to produce acceptor characteristics.

Boron and nitrogen doping of diamond during CVD might cause changes in growth and/or material properties based on either their interaction in the gas phase, in the growing surface (by some mechanism like the sub-surface N-induced hydrogen destabilisation

proposed by Yiming et al. [86]) or within the bulk material. OES can provide insight into the gas phase chemistry, showing relative emissions of plasma species in MP-CVD reactors. Detection of radicals containing boron and nitrogen might show whether the two elements undergo chemistry prior to their incorporation into the material, or if any interaction must be purely material related.

As discussed in section 1.4, there are various material properties affected by dopants, from mechanical properties to luminescence spectral features. In this thesis boron and nitrogen are introduced during CVD of diamond films. Various techniques can be used to characterise diamond, with the main focus here on film growth and electronic characteristics.

Thus this thesis presents a three-pronged approach to boron and nitrogen co-doping. An introduction to the theoretical and experimental concepts follows this chapter. The results then begin with a theoretical investigation of boron-nitrogen substitutional clusters in diamond, with up to 5 atoms per cluster. This is followed by an OES study of MP-CVD plasmas containing both boron and nitrogen, monitoring the emissions of boron and nitrogen containing species as a function of diborane, nitrogen and methane concentration in the process gas. Finally, a study of growth and analysis of diamond material grown with additions of diborane and nitrogen to the CVD gas mixture. This chapter presents growth rates, morphology, dopant incorporation and electrical properties such as resistivity, charge carrier excitation energy and thermionic emission.

Some of the presented results are preliminary, requiring further study to confirm, and some are conclusive. Nevertheless, as a whole this thesis aims to present an investigation, as comprehensive as possible, into co-doping with the hope that not only the boron-nitrogen combination might be better understood, but further combinations might similarly be understood in the future.

2

THEORETICAL AND EXPERIMENTAL CONCEPTS

2.1 First principles modelling

This section outlines why it is necessary to go beyond the simple Schrödinger equation for quantum mechanical calculations of materials, briefly introduces theories that tackle the problem of many electron systems and explains the approach of the *ab initio* codes used in this thesis.

2.1.1 Energy of a many-body system

The energy E of a simple quantum system can be expressed in terms of a wavefunction Ψ, as was derived by Schrödinger in the 1920s:

$$(2.1) \qquad \hat{H}\Psi = E\Psi$$

where $\hat{H}$ is the Hamiltonian operator. Being an operator, when $\hat{H}$ is enacted on the wavefunction it returns a value; in this case the energy of the system. For a general system of electrons and nuclei $\hat{H}$ can be expanded in its four terms:

$$(2.2) \qquad \hat{H} = \hat{T} + \hat{V}_{ee} + \hat{V}_{en} + \hat{V}_{nn}$$

where $\hat{T}$, $\hat{V}_{ee}$, $\hat{V}_{en}$ and $\hat{V}_{nn}$ return the kinetic, electron-electron potential, electron-nuclear potential and nuclear-nuclear potential energies respectively. Each can be written in full

[87]:

(2.3)
$$\hat{T} = \sum_i \frac{-\hbar^2}{2m} \nabla_i^2 \quad \hat{V}_{ee} = \frac{e^2}{8\pi\epsilon_0} \sum_{i \neq j} \frac{1}{|r_i - r_j|} \quad \hat{V}_{en} = \frac{-e^2}{4\pi\epsilon_0} \sum_{i,I} \frac{Z_I}{|r_i - R_I|} \quad \hat{V}_{nn} = \frac{e^2}{8\pi\epsilon_0} \sum_{I \neq J} \frac{Z_I Z_J}{|R_I - R_J|}$$

where there are N electrons denoted i (or j), $\hbar$ is the reduced Planck constant, m is the electronic mass, ∇ denotes a partial derivative with respect to each of the three spatial coordinates, e is the electronic charge, ϵ_0 is the vacuum permittivity, r is the position of the ith electron, Z is the nuclear atomic number of the Ith nucleus and R_I is the set of nuclear positions.

Since each term in equation 2.3 (apart from V_{nn}) contains a sum over all electrons or pairs in the system, the number of parameters required to solve them is equal to the number of parameters used to describe each electron multiplied by N. In the case of momenta and positions this is 3 since each electron exists in 3-dimensional space (this excludes spin, a fourth parameter). Given most systems of interest contain more than a few electrons, it is thus impossible to solve Schrödinger's equation for any system that might be of practical use.

Solutions to this problem were developed to attempt to get around this many-body problem, two of the most widely adopted incarnations being Hartree-Fock (HF) theory and density functional theory (DFT).

2.1.2 Hartree-Fock theory

Instead of considering every electron wavefunction together, Hartree-Fock theory approximates the wavefunction as a Slater determinant, which is a product set of orbital wavefunctions that is antisymmetrised such that it satisfies the Pauli principle:

(2.4)
$$\Psi = A.\det\{\psi_1(1), \psi_2(2)...\psi_N(N)\}$$

where only the diagonal element of the determinant product is shown, A is a normalisation constant and the orbitals are denoted ψ_i. Each element is acted upon by a new *Fock operator* defined as

(2.5)
$$\hat{F} = \hat{T} + \hat{V}_{ne} + \hat{V}_{nn} + \hat{V}_{Coulomb} + \hat{V}_{exchange}$$

where the first three terms are much like they were in $\hat{H}$ previously, but the $\hat{V}_{ee}$ term from equation 2.2 is split into terms $\hat{V}_{Coulomb}$ and $\hat{V}_{exchange}$. Primarily these potentials contain so called $\hat{J}$ and $\hat{K}$ operators respectively, which, importantly, are single electron

operators [88]. This means that to calculate the electron-electron part of the energy, HF considers each orbital ψ_i to individually experience a *mean field* of all the other electrons [89]. This charge density used by HF theory is variational, and the density (defined as $\sum_j |\psi_j|^2$) is unknown until each of the orbitals are known. Hence iterative calculations lead to a self-consistent field (SCF) where the energy is minimised [90].

The Slater determinant orbitals are an approximation made by HF theory, but the equations arising from them can be solved exactly, which is why HF methods are often referred to as *exact exchange* methods. Nowhere in the theory do correlation effects get explicitly treated however, so the energies from pure HF are often inaccurate [91].

2.1.3 Density functional theory

Hohenburg and Kohn showed in 1964 [92] that the ground-state energy E_0 of a system could be determined by a unique electron density solution ρ and also that it is variational. In theory any property dependent on the ground-state of a system could be derived from the density. In order to realise this density however, Kohn and Sham showed [93] that the electron-electron terms in the Hamiltonian must be split into two parts (similar to HF, but in a different way). These two parts are a classical potential deriving from an identical non-interacting density of electrons $V_{ee,ni}$ and an interacting exchange-correlation (xc) potential V_{xc}, which is combined with a part of the kinetic energy T_{xc} to make an overall xc energy E_{xc} [94]. Thus the two key equations of DFT:

$$(2.6) \qquad\qquad E_0 = E\left[\rho_0\right] = \hat{H}\left[\rho_0\right]$$

$$(2.7) \qquad\qquad \hat{H} = \hat{T}_{ni} + \hat{V}_{ee,ni} + \hat{V}_{ne} + \hat{V}_{nn} + \hat{E}_{xc}$$

where T_{ni} is the kinetic energy of the non-interacting electron density and the other terms are as defined above.

Each operator acts on the density function ρ, making them functionals, and only E_{xc} is not an exact equivalence to Schrödinger's equation. In this way, DFT is exact in its theoretical framework, but with approximations to the form of the electron interactions; contrasting with HF theory which makes its approximation during its theoretical formulation. E_{xc} is not a known functional, which means it has had many approximations since the first derivation over 50 years ago [93].

2.1.4 Exchange-correlation functionals

The form of E_{xc} is defined by an approximation which incorporates some level of detail of the surrounding electron density in any given position. The first example of this is the local (spin) density approximation (LDA, or LSDA), which was used by Kohn and Sham in their first implementation of DFT [93]. In essence the LDA considers the density surrounding any given position, ρ_Y, as equal to that of the given position, ρ_x, in its calculation of E_{xc}. Clearly in a real system this is never a good approximation, however for some systems, such as those with large atoms and therefore slowly spatially varying electron densities, the LDA does provide reasonable results.

Considering smaller atoms or for more detailed calculations, the gradient of ρ_x can be incorporated into the functional [95]. A generalised gradient approximation (GGA) often gives results closer to those of experiment [96] whilst taking a moderate amount of time and resources to compute. During the 1990s and 2000s various functional forms of the GGA were devised which are still being used by many researchers interested in pure DFT calculations, including PW91 [97], PBE [98] and WC [99].

For the purposes of this thesis the major drawback of GGAs is an underestimation of the band-gap [100]. This in some cases causes experimentally non-metallic systems to become metallic and hinders interpretation of dopant-related calculation results.

In order to correct E_{xc} for various molecular and periodic systems, *hybrid* functionals were developed to incorporate some amount of the exact exchange energy from HF theory [101]. This works to expand the energy range and, amongst other things, increase the size of the band-gap in solids [102]. There are various formulations including the chemically popular B3LYP [101] and the simpler HSE-06 [103, 104] and PBE0 [105]. Since these functionals require a calculation of the HF type in which each orbital is considered independently interacting with the density, as opposed to purely using functionals of the density, they are highly expensive to compute. This is especially the case for basis sets that require many functions.

2.1.5 Basis sets

In practical DFT and HF theory the electron orbitals or density must be constructed out of some set of functions, otherwise known as a basis set. There is no perfect way to do this, as no type of function is without its disadvantages in some respect. This thesis is concerned with periodic systems, and as alluded to it is also concerned with band-gaps; these two things will frame this basis set discussion.

The obvious choice for a periodic system is a function that has the same periodicity. In a periodic system the theoretical states are Bloch states:

$$\psi_i(\mathbf{r}) = e^{i\mathbf{k}.\mathbf{r}}u(\mathbf{r}) \tag{2.8}$$

where $e^{i\mathbf{k}.\mathbf{r}}$ is a phase factor and $u(\mathbf{r})$ is some real ($\mathbf{r}$) space function that is periodic over a length $\mathbf{L}$. If we move by $\mathbf{L}$ then:

$$\psi_i(\mathbf{r}+\mathbf{L}) = e^{i\mathbf{k}.(\mathbf{r}+\mathbf{L})}u(\mathbf{r}+\mathbf{L}) = e^{i\mathbf{k}.\mathbf{L}}\psi_i(\mathbf{r}) \tag{2.9}$$

so a movement by $\mathbf{L}$ causes a phase change dependent on the reciprocal space position $\mathbf{k}$.

One function that can be made periodic in $\mathbf{L}$ is plane-waves. If we define $u(\mathbf{r})$ as a Fourier series:

$$u(\mathbf{r}) = \sum_G c_G e^{i\mathbf{G}.\mathbf{r}} \tag{2.10}$$

where c_G are the Fourier coefficients and $\mathbf{G} = 2\pi/\mathbf{L}$, a reciprocal lattice vector. $e^{i\mathbf{G}.\mathbf{r}}$ is a plane-wave that travels perpendicularly to the $\mathbf{G}$ vector.

In order to perfectly model any system a Fourier series would have to be infinite, but in practice it can sufficiently describe the electron density by using a limited set. As $\mathbf{G}$ becomes larger, the plane-wave energy becomes larger and the wave-length λ becomes smaller:

$$E = \frac{\hbar^2|\mathbf{G}|^2}{2m} \qquad E = \frac{hc}{\lambda} \tag{2.11}$$

where m is the effective mass and c is the speed of light. As λ gets smaller the plane-waves can describe more detailed electron densities, so a cut-off energy E_{cut} may be used to limit the number of required basis functions. This is typically a few hundred eV.

Plane-waves have one large disadvantage for the type of calculations required in this thesis. In order to attain a reasonable band-gap and therefore impurity properties, hybrid functionals are required, which means performing calculations on every basis function. Plane-wave basis sets require many basis functions to properly describe the electron density, so hybrid functional calculations are extremely computationally expensive.

The above problem is not shared by Gaussian orbital basis sets. A linear combination of atom-centred orbitals (LCAO) basis set using Gaussians provides a small set that can describe the electron density sufficiently; an approach well-used in chemistry. The wavefunction can be defined as

$$\psi_i(\mathbf{r}) = \sum_{\alpha}^{N_{\text{bf}}} c_{\alpha} U_{\alpha}(\mathbf{r}) \tag{2.12}$$

where a ($1 \leq \alpha \leq N_{\mathrm{bf}}$) set of basis functions, U_α, each have coefficients c_α. The Gaussian functions take the form of

$$(2.13) \qquad\qquad\qquad U_\alpha(\mathbf{r}) = a_\nu e^{-b_\alpha \mathbf{r}^2}$$

where a_ν and b_α are coefficients to be optimised for a system. The a_ν coefficient incorporates the symmetry of a system, and is proportional to $\mathbf{r}^l$ where l is the angular momentum quantum number. Thus for example the d-orbital has an $\mathbf{r}^2$ term in the Gaussian function, providing the 2-fold d-symmetry.

2.1.6 CRYSTAL and CASTEP codes

The calculations performed for this thesis make use of CRYSTAL14, an all-electron Gaussian orbital basis set code, and CASTEP, a plane-wave pseudopotential code.

Pseudopotentials are functions that eliminate core electrons from a calculation, in some cases vastly reducing the number of electrons required to construct the electron density [106]. Moreover, they account for the part of the electron density that is most quickly varying in space, and thus reduce the required maximum energy of plane-waves in CASTEP.

Even with the use of efficiency enhancing pseudopotentials, CASTEP still suffers from the requirement of a large basis set to model the Kohn-Sham electron density. The resulting cost to calculate the SCF using a hybrid functional is orders of magnitude higher than for a GGA. For this reason the Gaussian orbital basis sets of CRYSTAL14 are better suited to hybrid functional calculations. The CRYSTAL14 program uses a limited number (≈ 15) of orbital functions to describe the density. Hybrid calculations are therefore not overly expensive, and in some cases are only around double or triple as costly as GGAs.

2.1.7 Convergence

Convergence in DFT is the state in which both the SCF is variationally minimised and the approximations made by the calculations have a minimal effect on the resulting energy and properties. Two fully converged calculations making use of the same xc functional, but with entirely different basis sets, will give exactly the same results in every case. The limitation of basis sets is that they are rarely fully converged: Gaussian basis sets are element dependent and can be inaccurate for certain chemical systems,

and pseudopotentials are never completely accurate. However, good agreement can be made if detailed basis sets and high plane-wave cut-off energies are used.

In practice, convergence in CRYSTAL14 and CASTEP often involves setting calculations parameters such that when the iterative processes - e.g. SCF minimisation or geometry optimisation - cause changes in energy less than a threshold value, the calculation is deemed to be converged, at least with respect to that parameter.

In theory, a periodic calculation must integrate over all reciprocal space ($\mathbf{k}$) in order to find the density. One approximation that is commonplace is using a grid of k points [107] fine enough that the Brillouin zone is sampled sufficiently:

$$(2.14) \qquad \rho(\mathbf{r}) = \int |\psi_k(\mathbf{r})|^2 d^3\mathbf{k} \approx \sum_k |\psi_k(\mathbf{r})|^2$$

which means a set of symmetric k-points can be converged in order to sufficiently represent the Brillouin zone.

2.2 Microwave plasma-activated chemical vapour deposition of diamond

This section introduces concepts relevant to both growth of diamond films and optical emission spectroscopic (OES) studies of the plasma itself. The two experiments make use of the same microwave-plasma activated chemical vapour deposition (MP-CVD) equipment and study the results of addition of boron and nitrogen to a hydrocarbon CVD plasma.

2.2.1 CH$_4$/H$_2$ plasma chemistry and the CVD mechanism

In a hydrogen containing microwave plasma high gas temperatures and energetic electron impacts cause H$_2$ to be excited, dissociating some fraction of the gas to form atomic hydrogen, the driving species for diamond growth [108]. The H atom carries out hydrogen abstraction: the removal of a hydrogen atom from another species to combine into H$_2$. This can happen to any H it makes contact with, be it bonded to another H, a C atom in methane, or a C atom on the diamond surface. These abstractions are essential to diamond growth, initiating the steps required for addition of carbon to the growing surface. In the gas phase the abstraction of H from (e.g.) CH$_4$ produces CH$_3$ radicals, the main precursor to epitaxial growth [109, 110]. In the plasma, CH$_x$ and C$_2$H$_x$ species inter-convert, frequently through reactions involving hydrogen, C$_2$H$_2$ being the most

prominent product. On the growing surface H abstraction provides the necessary unsaturated (or "dangling") bonds that facilitate chemisorption of gas phase CH_x radicals - see the mechanism below. H atoms are so uniquely important to the diamond growth process that hydrogen constitutes roughly 94 - 99 % of the process gas mixture in MP-CVD reactors.

As the main growth species, the CH_3 radical is responsible for addition of carbon to the diamond surface via the H-abstracted dangling bonds [111]. On, for example, a (100)-2x1 surface the reaction proceeds through a mechanism such as that depicted in figure 2.1; a gas phase H atom reacts with a surface terminating H atom, forming H_2 and leaving an unsaturated carbon atom on the diamond surface (abstraction); this facilitates the attachment of a CH_3 radical to the unsaturated carbon (addition); a second H atom reacts with a hydrogen from the newly attached carbon which it leaves unsaturated (abstraction); the new, unsaturated carbon finds a lower energy position above the centre of the dimer, breaking the bond between the two carbon atoms beneath (bridging); this leaves an unsaturated carbon on the original surface that can facilitate further chemisorption. This mechanism illustrates the importance of atomic hydrogen to the growth process, and suggests that CH_3 and (to some extent) CH_2 will dominate the productive chemisorption reactions that lead to growth. Further mechanisms, such as those that consider more than one CH_x addition [112] and those on other surfaces, have been explored but aren't outlined here.
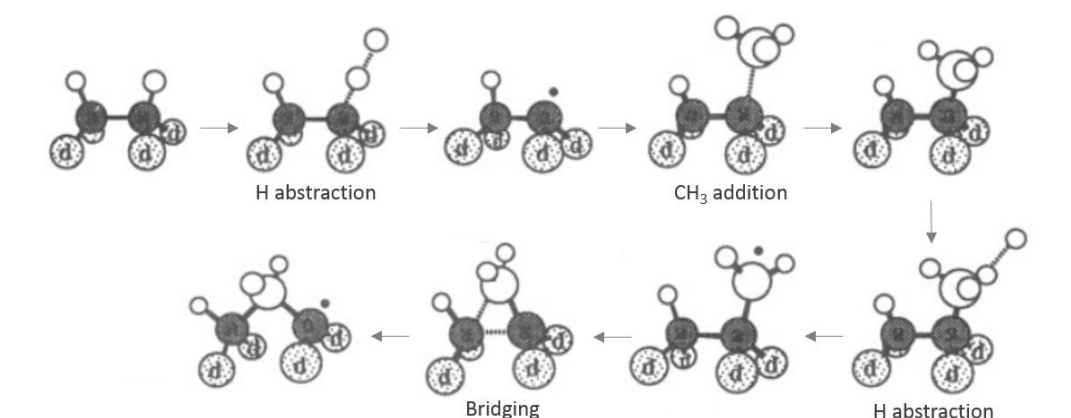
Figure 2.1: An example growth mechanism involving CH_3 addition to the reconstructed (100) surface of diamond. Spotted and dark circles are diamond carbon atoms under (d) and on (a) the surface respectively, small white circles are H atoms and large white circles are adsorbing C atoms. Small dark spots denote unsaturated bonding on a carbon atom. Adapted from [3].

Microscopically, crystals predominantly grow by step progression. Addition to the lower side causes expansion of the step in the higher-to-lower side direction, enlarging the higher atomic layer. New steps must be nucleated either at existing defects on a plane or simply by addition to the middle of a plane.

2.2.2 Effect of dopants on diamond growth

Non-hydrocarbon species have long been known to affect the synthesis of diamond, both in terms of growth rates and in crystal morphology. Parts per million levels of nitrogen in the process gas mixture cause a striking enhancement of the deposition rate, with increases of up to 10 times when using 200 ppm nitrogen compared to nitrogen-free conditions[113].

The exact mechanism for this increased rate in unknown, but explanations have been put forward based on both experiment and theory [85, 86]. Yiming et al. predict that substitutional N in the sub-surface of diamond reduces the hydrogen-carbon bond energy nearby, destabilising the hydrogen termination, causing faster generation of unsaturated carbon surface sites and accelerating the addition of further carbon to the surface [86]. Dunst et al. provide a model for a catalytic effect, where a hypothetical carbon-nitrogen containing species is adsorbed and enhances carbon adsorption before desorbing back into the gas phase [85]. The authors assume CN is the primary species involved in this catalytic process, which, since the enhancement is increased at high plasma power density [113], is consistent with more recent kinetic models that show CN density is greater at high pressure [114]. A key finding is that nitrogen appears to increase the likelihood of (100) facet formation [115], which Yiming et al. claim is a result of higher growth rate on the (100) surface caused by the presence of nitrogen [86].

Boron is known to incorporate readily into the (111) plane of CVD diamond [116] and can also change the texture and orientation of synthetic films. There is disagreement in the literature regarding the effect of boron on growth rate of diamond, with its addition commonly seen to reduce rates [117], but with no well-known mechanism. On the other hand, work done by Achard et al. show an increased growth rate in MP-CVD with boron present [118]. Sartori et al. [83] have shown that the growth rate enhancement of nitrogen can be suppressed by ppm levels of boron in the plasma, providing an explanation for the perceived growth rate decrease experienced by many users of boron in the past (their reactors likely contained some level of nitrogen impurities). A similar suppression could occur for morphological changes attributed to nitrogen, but this is not explored in the literature. The work of Sartori et al. disagrees with that of Dunst et

al. [85] since the authors find no quenching of the CN optical emission intensity upon introduction of boron-containing gases [83].

These selected examples show that there are various open questions regarding the incorporation and rate effects of nitrogen and boron dopants in diamond growth. This thesis attempts to add to this discussion.

2.2.3 Experimental apparatus

The MP-CVD reactor, used for experimentation on this project and for the OES part of this thesis, is shown schematically in figure 2.2. Using this apparatus it has been possible to introduce both boron and nitrogen to the growth plasma, and to consequently dope both species into the bulk material. Great care was taken when refurbishing and constructing the apparatus, since boron introduction is an irreversible process, a contamination issue known as the "memory effect" whereby boron oxide is deposited throughout the reactor to then be re-introduced gradually to the gas phase. High vacuum components were employed, along with a new welded gas manifold, whilst various other parts were repaired or replaced. This ensured minimal air-leak contamination, which, when combined with high purity gases installed specifically for this purpose, meant the lowest possible interaction of boron species with those causing contamination or lower B concentration.

As shown in figure 2.2, the substrate rests on a metallic disk (Mo or W), which rests on a thin circular wire (Mo or W), which in-turn rests on a water-cooled base-plate (Al). By altering the combination of these components (disks and wire thicknesses), the thermal coupling between substrate and base-plate changes and the substrate surface temperature can be altered, a change that is reproducible provided each thermal contact is consistent. This is a superior method of altering substrate temperature than (e.g.) changing plasma power, since it does not also change other process parameters such as plasma power density.

2.2.4 Parameter space and substrates

As a project that has a focus on dopants, the gas-phase concentration of these dopants is the primary parameter considered when comparing two samples. However, there are other considerations as well. The substrate temperature is known to change the incorporation efficiency of dopants during growth of CVD diamond [119]. For this reason the wire thicknesses were changed during part of the project, delivering a growth
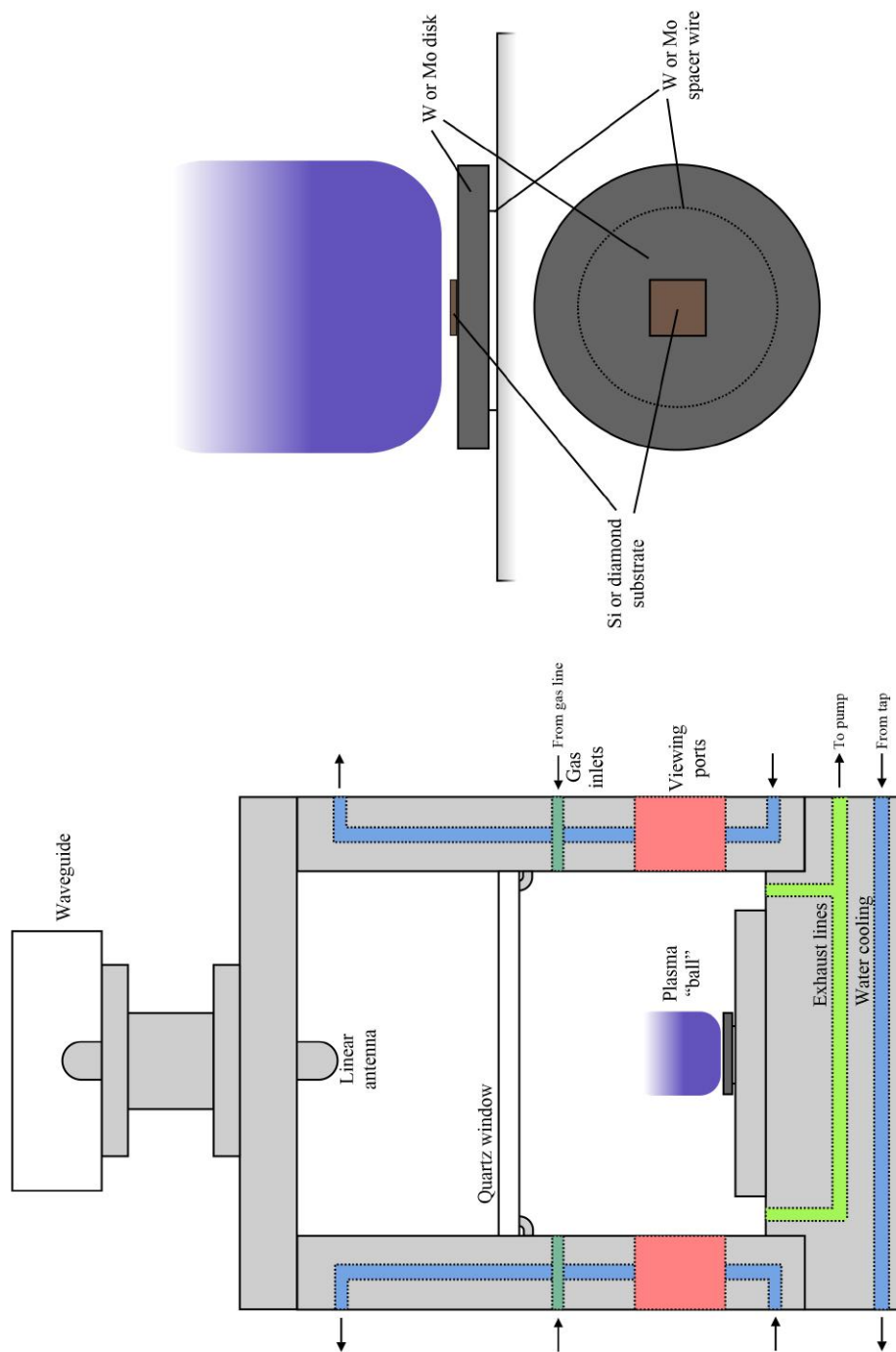
Figure 2.2: Schematic diagram of the reactor chamber (left) and enlarged schematic of the wire-disk-substrate construction (right). 2.45 GHz Magnetron-generated microwaves enter via the waveguide, are transmitted by the antenna, and resonate inside the chamber. The plasma "ball" is centred on an anti-node of the standing wave. The substrate is heated by the plasma and cooled through the baseplate, with the wire (of variable thickness) between disk and baseplate dictating temperature for given conditions. Water is flowed through the chamber walls, baseplate, and a heat-sink to prevent reflected power damaging the magnetron. Gas enters the chamber through two diametrically opposing inlets and leaves through holes in the baseplate towards the pump; pressure is measured and controlled in the exhaust line. Glass or (for OES) boro-silicate viewing ports allow visual examination and data collection.

temperature difference on the order of 200 K. The other major consideration is substrate requirements for the various materials experiments. Silicon is a cheap, easily processed and (in general) semi-conductive material that makes a good substrate owing to its carbide formation and relatively similar thermal expansion coefficient compared to diamond ($2.6\,\mathrm{MK}^{-1}$ to $1.0\,\mathrm{MK}^{-1}$; cf. $4.8\,\mathrm{MK}^{-1}$ for Mo). Delamination occurs upon post-growth cooling when thermal expansion coefficients are too mismatched. Silicon is used for many experiments with CVD diamond, including those presented here on growth rates, morphology, and dopant concentration. Unfortunately, due to its relatively low resistivity, Si is unsuitable for electrical measurements.

Diamond substrates provide a combination of perfect thermal expansion coefficient match, extremely high resistivity and, if a single crystal is used, the opportunity to grow single crystal material. The former of these advantages means bulk, microcrystalline material may be used for experiments such as thermionic emission (section 2.4.4) instead of thin layers of nanocrystalline diamond on (e.g.) molybdenum, whose expansion coefficient is such that diamond readily delaminates after it is grown thick enough. High resistivity of the substrate means Van der Pauw resistivity measurements (section 2.4.3) are feasible, since current is carried through the grown material. And finally, single crystalline material allows deconvolution of bulk material properties from those of the inherent grain-boundaries within polycrystalline material. This may provide insight into whether dopants incorporate more readily at grain boundaries or bulk, or at different growth facets.

2.3 Optical emission spectroscopy

With concepts from section 2.2 of continuing relevance, this section concerns the measurement of optical emissions from the growth plasma. The understanding of this data requires knowledge of what causes the emission intensities measured, the apparatus itself, and finally the software used to analyse it.

2.3.1 Atomic and molecular emissions

Quantum mechanics dictates that energy levels in atoms are discrete, meaning the absorption and emission of energy is quantised. The specific energy gaps between the electronically excited (and ground-) states of an atom are characteristic of that atom, and can be used to identify their presence. The peaks or *lines* in the atomic optical emission

spectrum are isolated and often strong, since with only electronic levels there are few decay routes possible.

The same isolation is not true of molecules, which also have vibrational and rotational energy levels. Figure 2.3 shows an energy (or Jablonski) diagram of molecular excitation and emission. Like atoms, molecules have characteristic emissions, but with more complex emission profiles. The excitation, through various mechanisms such as collisions with hot plasma species and energetic electrons, results in electronically excited states that can decay either by further collision or by light emission.
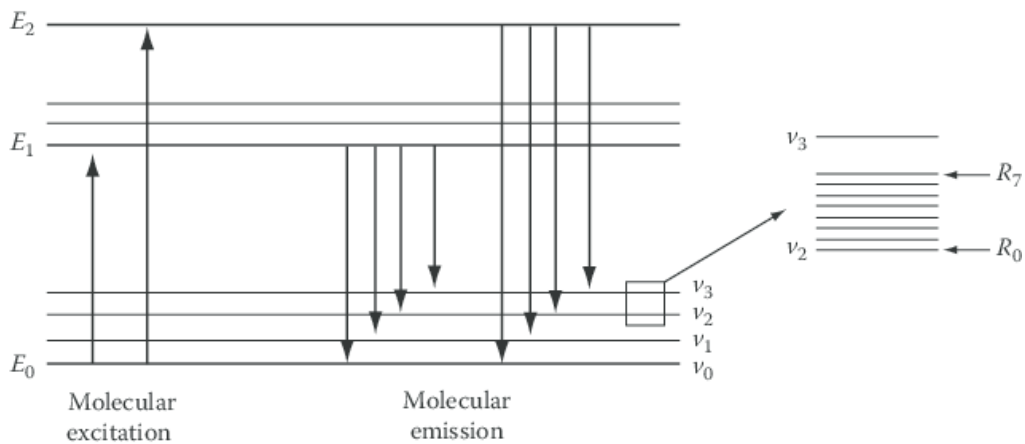
Figure 2.3: A Jablonski diagram showing molecular electronic excitation and emission to a range of vibrational states. The inset shows the rotational levels within. From reference [4].

The emission energy is dependent on the initial and final state separation, and each can be in a range of vibrational or rotational levels. Often, emissions examined in experiments will be of a specific vibronic (vibrational-electronic) transition; e.g. the vibrational ground-state of the first electronically excited state (A) to the first vibrationally excited state of the electronic ground-state (X). Each vibronic transition has a spectrum of emission lines spaced roughly equally energetically distant from each other, a distance equalling the gap between rotational levels. This is the form taken by the transitions of the diatomic species studied by OES in this thesis.

Along with an atomic emission, namely of the boron atom, the molecular emissions are shown in table 2.1, and allow detection of both boron and nitrogen containing species.

Emission intensity from the gas phase species in the plasma is a probe of excited states and therefore is a function of multiple variables: (1) the species number density in the studied plasma region n_X, (2) the number density of electrons present in the plasma n_e, (3) the electron energy distribution (EED) and (4) non-radiative decay by collisions,

Table 2.1: Details of the optical emissions studied in this work. Term symbols have the general form of {Electronic state}$^{\{total\ spin\}}${Orbital angular momentum}$^{\{reflection\ symmetry\}}_{\{inversion\ symmetry\}}$. A full explanation of term symbols is unnecessary here.

Species	Initial-Final State	Centre Wavelength / nm	Spectroscopic Constants Ref
N_2	$C^3\Pi_u - B^3\Pi_g$	337	[120]
NH	$A^3\Pi - X^3\Sigma^-$	336	[121]
BH	$A^1\Pi - X^1\Sigma^+$	433	[122]
B	$3^2S - 2^2P$	250	—
CH	$A^2\Delta - X^2\Pi$	431	[123]
CN	$B^2\Sigma^+ - X^2\Sigma^+$	388	[124]

affected by (e.g.) pressure. This list makes the common assumption that electron impact excitation (EIE) is the primary excitation mechanism in this system [125]. For small additions of some gases such as diborane and nitrogen, which may be assumed not to alter the electronic characteristics and size of the plasma, this means that optical emission intensity can be considered a relative indicator of concentration. Care must be taken in this interpretation however, because n_e and the EED may in fact be affected by gas composition in some cases; for example by a change in the average ionisation energy of the gas.

The gas temperature T_{gas} will have an effect on the shapes of many emissions, since for example higher temperatures increase population of higher rotational states. The ratio between emission intensity from different rotational levels, as well as other temperature induced effects like broadening, can be used as a probe of the excited state rotational temperature T^*_{Rot}, and the assumption that $T^*_{Rot} \approx T_{Rot} \approx T_{gas}$ provides a proxy for estimating T_{gas} through OES [69]. The temperatures of different gases in the plasma are thought to be similar owing to the high collision rate at the pressures suitable for MP-CVD. For this reason, the most reliable gas temperature data available during an OES experiment will likely be from the emission of one reliable diatomic species.

2.3.2 Experimental apparatus

Optical emission spectroscopic measurements were carried out using the same reactor setup as described in section 2.2.3. Within the reactor, the only difference being that no substrate was included, in accord with previous OES work in the group.
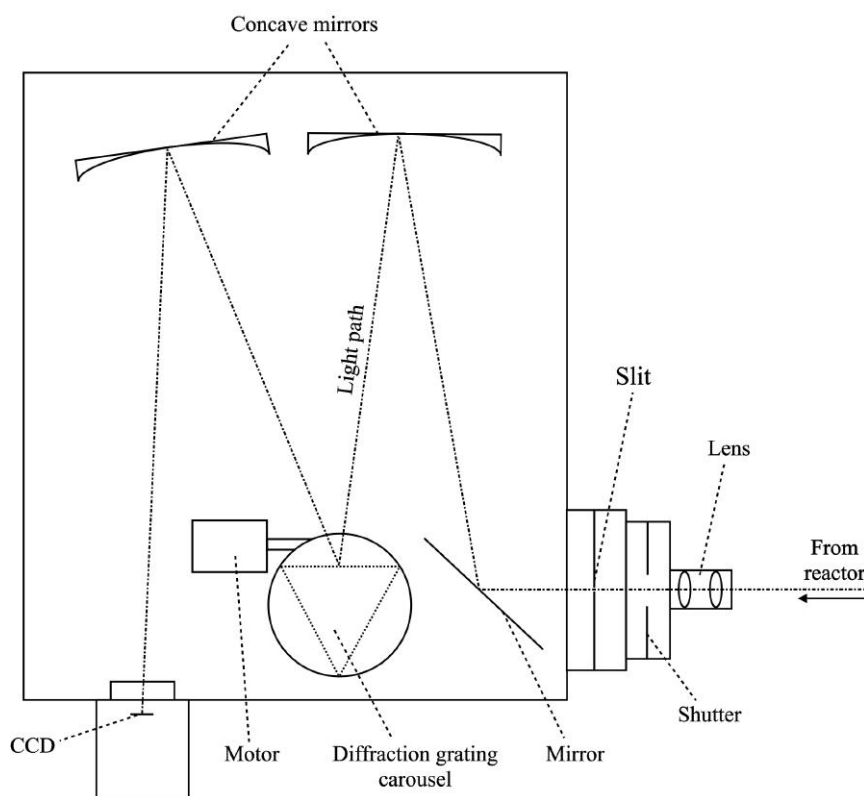
Figure 2.4: A schematic diagram of the optical emission spectrometer.

The measurements were taken with a Shamrock spectrometer (SR-303i-A, Andor, UK) on a Newton^{EM} CCD (DU970P-BV, Andor, UK) equipped with a 500 mm focal length, f/5.6 objective lens. A schematic of the measurement apparatus is shown in figure 2.4. Briefly, light enters through a lens focused on the centre of the plasma, before passing through a narrow vertical slit, reflecting off a flat mirror and a concave mirror followed by a diffraction grating. Upon reflection from the grating it is split into its spectral constitution, then reflected by a second concave mirror towards the CCD. Vertical spatial resolution is maintained whilst the horizontal axis becomes a wavelength range dependent on the line spacing of the diffraction grating. In this way, 2-dimensional intensity-wavelength spectra can be acquired for a range of heights above the disk.

2.3.3 Pgopher software

PGOPHER is a software package developed by Dr Colin Western at the University of Bristol [126]. The program is able to fit the theoretically produced spectra of simple molecules to experimental data [127]. In order to do this, many properties of the system are calculated, which means these properties can be collected as outputs from the analysis process. Various input parameters are required by the model spectra (many are from
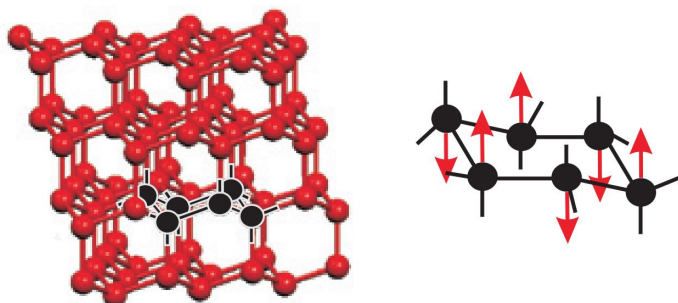
Figure 2.5: A schematic diagram showing the Raman-active vibrational mode in diamond. The 6-membered ring within the lattice (left) is flattened as alternating carbon atoms move up and down (right). Adapted from [5].

the references given in table 2.1), and the outputs from the fitting are, in this work, *abundances* (intensity) and *rotational temperatures*.

PGOPHER provides a more systematic and detailed way to analyse data than simple peak integration, since, provided data is high enough quality, it can subtract polynomial baselines as well as fit multiple molecule spectra to the same data. This means deconvolution and simultaneous analysis of overlapping spectra is possible.

2.4 Material characterisation

2.4.1 Raman spectroscopy

Raman spectroscopy is a simple, non-invasive tool for characterisation of a CVD diamond film, requiring (or in fact benefiting from) no sample processing prior to analysis. Characteristic signatures for sp^3 and sp^2 carbon allotropes are clear in Raman spectra, so at least qualitative interpretation of data is trivial.

Raman spectroscopy is known as an infra-red spectroscopic technique, since its spectral data lie in the IR region. A perfect diamond crystal is inactive in traditional IR spectroscopy due to its lack of (changeable) dipole moment. However, Raman scattering takes place accompanied by a *polarisability* shift, so no dipole is required. In the diamond Raman process, an incoming photon of relatively high energy interacts with a phonon mode of the crystal. This mode, as shown in figure 2.5, can be visualised as a flattening of a 6-membered ring, or as a compression within and stretch between (111) planes. Consequently the polarisability changes, so an excitation to a virtual state is possible. The final state after decay can be one of higher vibrational energy than the initial state, with the relative energy denoted the Raman shift. For sp^3 carbon this energy is equivalent to 1332.6 cm^{-1}.

The primary beam consists of a focused laser with a wavelength in the ultra-violet

to infra-red region of the electromagnetic spectrum. Different excitation wavelengths promote different Raman modes, favouring sp^3 carbon over sp^2 at shorter wavelengths.

2.4.2 Scanning electron microscopy

Scanning (or secondary) electron microscopy (SEM) is the most powerful and ubiquitous technique in the field of surface morphological analysis. Images of high (nm) resolution can be acquired in a matter of seconds at any given magnification up to > 50k times. Samples must be somewhat conductive to avoid charging effects, which can alter images in real time and therefore hamper collection of useful data. However, coating with a conductive film such as gold or silver, thin enough so as to not change the microscopic surface structure, can solve charging problems.

The technique works by directing a focused high energy (tens of keV) beam of primary electrons at the sample surface via a series of electron optics. These incident electrons cause secondary electron production within the material via inelastic collisions. Some non-zero proportion of the generated secondaries will vacate the material, and an electron detector can count them. The intensity of secondary electrons detected will translate into a brightness datum for the given position on the sample. Because the beam is directed precisely at one position at a time, a raster process can build up a picture of the surface by constructing a brightness map from the secondary electron intensity at each point.

2.4.3 Van der Pauw measurements

Semiconductors are characterised by their low and alterable carrier density and their low and (positively) temperature dependent conductivity. The Van der Pauw (VDP) technique offers an effective probe of the latter characteristic. Unlike a "normal" electrical measurement in which voltage is applied and current measured, VDP works by applying a set current and measuring voltage.

In the VDP configuration (figure 2.6), a current is driven between two adjacent corners of the square, and a voltage is measured between the other two. The experiment may be thought of as a square grid of N arbitrarily small square resistors, both in series and in parallel. Resistance is proportional to N in series, and inversely proportional to N in parallel. As long as the sample remains a square, the number of in-series resistors equals the number in parallel. It follows that the size of the sample makes no difference to the sheet resistance, provided the assumption of point-like contacts holds.
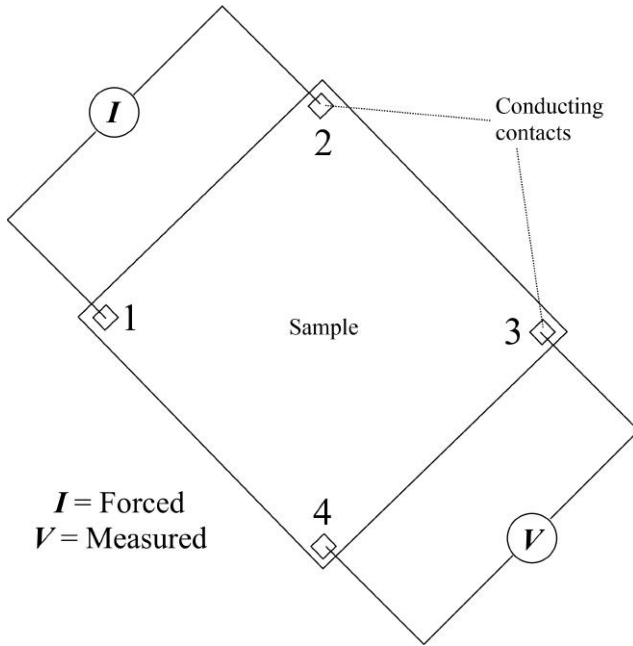
Figure 2.6: A schematic of the Van der Pauw technique. Current is driven between two adjacent contacts (e.g. 1 and 2) and the consequent voltage between the remaining contacts (e.g. 3 and 4) is measured. Configurations A and B are equivalent measurements using different combinations of adjacent contacts, for example if A is the example given, then B drives current between 2 and 3, and measures voltage between 4 and 1. Positives and negatives of each combine to make 8 measurements data set.

The resulting data acquired are resistance values, which provides the sheet resistance (R_S) when combined via

$$(2.15) \qquad \exp(-\pi R_A/R_S) + \exp(-\pi R_B/R_S) = 1$$

where R_A and R_B are the resistance values acquired in configurations A and B respectively. This equation must be solved iteratively, which is possible by scripting in MATLAB.

The resistivity may be acquired from the sheet resistance via $\rho = R_S d$, where d is the film thickness.

VDP measurements are made possible by an in-house built apparatus, for which Dr James Smith is gratefully acknowledged. However, this equipment is limited to conventional room temperature measurements. In semiconductors, the finite activation energy of charge carriers from dopants means conductivity (σ) is strongly dependent on temperature [128]:

$$(2.16) \qquad \sigma = \mu N \exp\left(\frac{-E_A}{k_B T}\right) = \frac{1}{\rho}$$

where μ is the mobility, N is a factor incorporating the number of donors and acceptors present in the sample as well as the valence band density of states, E_A is the impurity activation energy, k_B is Boltzmann's constant and T is the sample temperature. μ and N have a temperature dependence of order $-A$ and $\frac{3}{2}$ respectively, where A is a constant

that can be assumed close enough to $\frac{3}{2}$ that equation 2.16 simply has an exponential T dependence [129].

To achieve precise control of a broad range of sample temperatures, the in-house built apparatus commonly used for thermionic emission experiments (see section 2.4.4) was re-purposed with the 4 point probe equipment attached. The experimental apparatus is shown in figure 2.7.
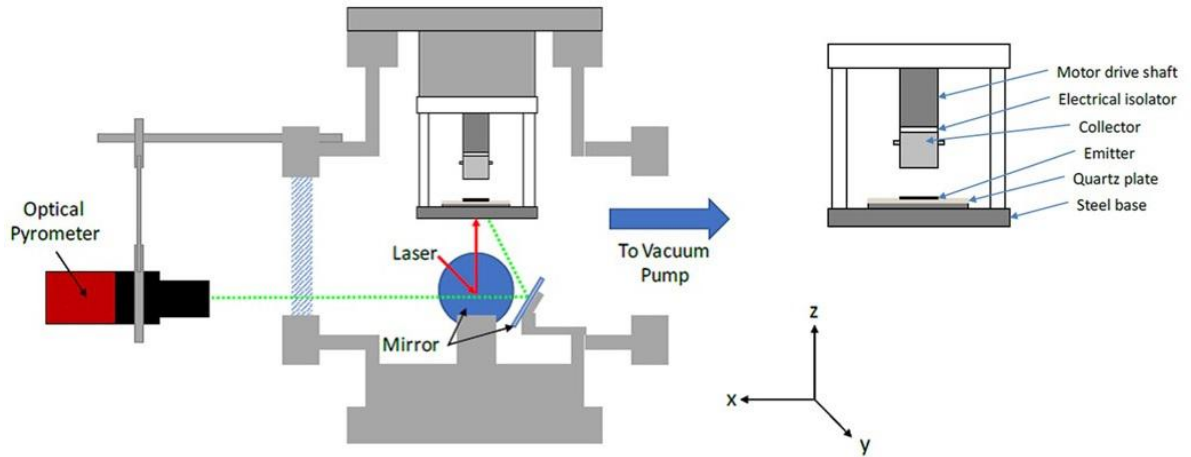
Figure 2.7: A schematic diagram of the high temperature electrical apparatus used for both temperature-dependent Van der Pauw measurements and thermionic emission measurements. Adapted from [6]. The same sample mounting was used for both experiments, but with clamps appropriate to each and the collector not used for VDP.

2.4.4   Thermionic emission

When a sample is heated to some material-dependent high temperature, it is possible for electrons to escape it into a surrounding vacuum. The work function, W, of a material dictates the energy cost to each electron to leave the surface, so it follows that a low work function will cause a high rate of thermionic emission. The well known equation of Richardson and Dushman relates the thermionic current density, J, to temperature, T, for metal surfaces [130]:

$$(2.17) \qquad J = A_{\mathrm{R}} T^2 \mathrm{e}^{-\frac{W}{k_{\mathrm{B}} T}}$$

where A_R is a material specific parameter that incorporates various physical properties and constants and k_{B} is Boltzmann's constant. Two problems arise when applying this equation to diamond: firstly, the derivation of A_{R} assumes a continuous $E^{1/2}$ dependence

of the density of states (DOS) on energy [131], but diamond has a discontinuous DOS near the Fermi level. Secondly, the surface is assumed to be perfect and unchanging. We know from both thermionic and photoemission experiments that the hydrogen termination required for a NEA is desorbed at high temperature [132], which renders the surface irreversibly (for the duration of the experiment) altered.

Due to the shortcomings of the Richardson equation, the group has taken two approaches: (1) to simply analyse the thermionic emission threshold temperature and maximal current density, and (2) to add a hydrogen desorption component to the Richardson-Dushman model. As this thesis is concerned primarily with materials analysis, option one is appropriate to sufficiently describe the thermionic properties of the sample set. Option (2) is presented in an in-preparation publication, and is not discussed further here.

A similar experimental apparatus was used to examine TE as with the T dependent VDP measurements, but instead of isothermal control the laser heats samples as rapidly as is reproducible in order to acquire emission current data before hydrogen desorbs significantly.

A limitation to the technique is space-charge, where electron density in the vacuum gap causes a further potential barrier for electrons to overcome if they are to escape the emitter completely. To mitigate this, a voltage is commonly applied to the collector, nullifying the power producing potential of thermionic emission, but allowing data collection for material comparison.

2.4.5   Secondary ion mass spectrometry

In order to ascertain the success of a doping experiment, the incorporation efficiency must be acquired from a concentration measurement. Few techniques can reliably measure the concentration of dopants in diamond due to the variability of defect structures and the consequent plethora of spectral signatures. Moreover, incorporation of both boron and nitrogen, two dopants which could become bound together within the material, may interfere with spectral characterisation. This leaves secondary ion mass spectrometry (SIMS) as the method of choice. It being a destructive technique, samples must have all other experiments carried out upon them before SIMS analysis.

In SIMS the primary beam is a heavy ion beam, in this case gallium, and the secondary output is a huge array of electrons, radicals and ions unique to the sample being analysed. Figure 2.8 shows a schematic of the technique, in which electric and

magnetic sectors (MS) perform spectroscopic analysis on the secondary ions. The MS-SIMS kit in the IAC is an in-house built apparatus.
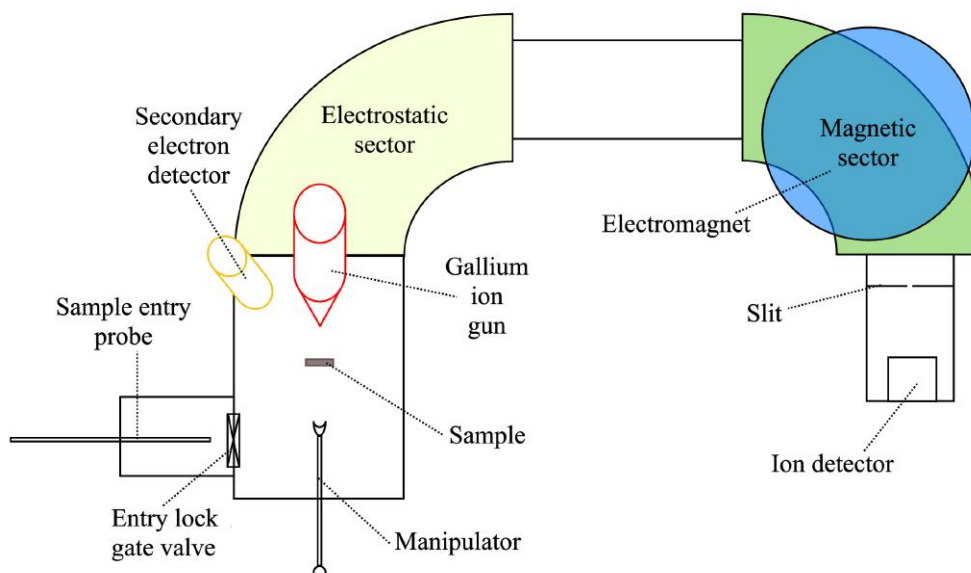
Figure 2.8: A schematic diagram of the high vacuum magnetic sector secondary ion mass spectrometry (MS-SIMS) equipment, recreated from reference [7].

Vapourised gallium ions are accelerated by a high voltage to bombard the sample surface, delivering large amounts of energy to and progressively etching the surface atoms. The resulting debris travels isotropically away from the sample. Of the charged ions in this debris, those which enter the electric sector are energy-selected and of the selected energy, those of a specific mass-to-charge ratio (often shortened to mass) are selected in the magnetic sector.

A mass spectrum can be acquired showing the range of ions detected, giving well-resolved peaks at integer masses. The carbon peak at mass-12 is the mark against which dopant containing ions are compared in this work. The longest-lived most stable ions are those examined, which for boron and nitrogen are B^+ and CN^- respectively. Positive and negative ions must be detected separately, so an individual experiment is required for each.

After the (mass-to-charge ratio) position is found from a mass spectrum, a depth profile can show the number of counts of B^+ and C^+, or CN^- and C^-, the ratio of which is multiplied by a calibration factor to find the concentration. This factor was acquired by analysing a sample in which a known concentration of dopants had been implanted, an experiment carried out by Dr Peter Heard for which he is gratefully acknowledged.

Generally assumed to be constant for diamond materials, the etch rate can be determined by combining cross-section measurements from the SEM with multiple conclusive depth profiles.

First principles modelling of boron-nitrogen substitutional clusters in diamond

The majority of this chapter is to be submitted for publication (currently in preparation). I gratefully acknowledge the following co-authors; M. Zamir Othman, Sergio Conejeros, Neil A. Fox and Neil L. Allan. I performed all calculations, analysed the data and wrote the draft of this work.

3.1 Introduction

Lacking a suitable single n-type dopant for diamond, the attention of many theorists has turned toward combinations of small atoms arranged in clusters as a means of producing a shallow donor [44, 50, 133].

Theoretical work has provided insight into various combinations of elements, highlighting clusters that add one electron to the diamond lattice such as BN_2 [49], Si_4N [52] and LiN_4 [53]. It is clear from intensive research that care must be taken when studying these clusters, both theoretically - e.g. when choosing the supercell size [134] - and from an experimental point of view - e.g. the ease of cluster fabrication [135]. The predicted stability, or binding energy, of these clusters is often high since, thanks to electronegativity and size effects, co-dopants couple strongly [55].

Much of diamond synthesis results in dispersed dopants, however the high temperatures involved in HPHT growth and annealing facilitate dopant migration, with

annealing studies showing creation of large binding energy cluster defects such as A- and B-centres [136]. Since this process allows formation of complex nitrogen-vacancy clusters, it may be the most promising route to formation of clusters more useful for n-type diamond material.

If produced by HPHT, some of the electronically promising clusters predicted to date will be outnumbered by others of higher stability. An example of this is the N-B-N (or BN$_2$) cluster since density functional theory (DFT) calculations predict that a B-N-N cluster (comprising a central N coordinated to one N and one B) is more stable by 0.5 eV [137]. In fact, there could be a range of defects with varied stability and properties that combine two elements, but many of the studies performed to date focus their attention on a limited set of the most promising clusters.

Hu et al. [77] studied various clusters of boron and nitrogen in diamond by classical molecular dynamics simulations with Tersoff potentials, but the study failed to reproduce the experimental symmetry of the substitutional nitrogen (C-) centre, predicting it to be tetrahedral with 4 elongated bonds compared to those of pure diamond. Experimentally the nitrogen centre is known to have C_{3v} symmetry with one elongated and three shortened bonds [138]. With a prototypical defect such as this [139] incorrectly modelled, to date there has been no satisfactory computational survey of the possible boron-nitrogen substitional defects that could be present in HPHT diamond. Furthermore, the electronic behaviour of predicted clusters is as yet unexplored.

To begin to understand co-doping as a method of altering the properties of diamond, an extensive survey of the possible combinations of dopants is required. This chapter presents an *ab intio* study of boron-nitrogen clusters in diamond, with both nitrogen-rich and boron-rich complexes considered. Both the energetics and electronic properties of these systems are evaluated and discussed in terms of their probable existence in HPHT material.

3.2   Computational methods

Spin polarised all-electron electronic structure calculations were performed using the CRYSTAL14 program [140] on 512-atom diamond supercells using periodic boundary conditions. Exchange and correlation were treated by the revised hybrid DFT Hartree-Fock functional of Heyd, Scuseria and Ernzerhof (HSE-06) [141]. For carbon, a 6-21G* basis set [142] of 10 Gaussian functions of s, sp and d symmetry described the electron orbitals. For boron and nitrogen impurities a detailed polarisation quality pob-TZVP

basis set [143] was employed, each with 17 Gaussian functions of s, p and d symmetry. For the 512-atom supercell, a converged Monkhurst-Pack [107] grid of $2 \times 2 \times 2$ special k-points sampled the Brillouin zone. During geometry optimisation (via the Broyden‚ÄìFletcher‚ÄìGoldfarb‚ÄìShanno, or BFGS, scheme [144]) the lattice parameter was fixed at that of the pure diamond supercell and the atoms allowed to relax with substitutional dopants in place of carbon atoms until the system energy changed by less than 10^{-7} Hartree per step. The Coulomb and exchange series overlap integral thresholds were set to 10^{-7} and 10^{-14}. Calculations of this type on pure diamond yielded bond lengths of 1.55 Å and a band-gap of 5.2 eV.

For this project, ground-spin state structural analysis took the form of symmetry, bond lengths and binding energies, alongside the energy of formation as defined by:

$$(3.1) \qquad E_{\mathrm{Fm}} = E_{\mathrm{defect}} + nE_{\mathrm{C}} - \left(E_{\mathrm{p}} + \sum_n \mu_i \right)$$

where E_{defect} is the energy of a supercell containing a geometry-optimised neutral defect or cluster; nE_{C} is the energy of n carbon atoms removed by substitution of n foreign atoms into the diamond lattice; E_{p} is the energy of the perfect (undefective) diamond supercell; μ_i is the energy of each of the n impurity atoms, calculated from standard states.

The binding energy, E_{b} indicates the interaction of two or more dopants within the lattice and is defined as:

$$(3.2) \qquad E_{\mathrm{b}} = E_{\mathrm{Fm,defect}} - \sum_n E_{\mathrm{Fm,iso}}$$

where $E_{\mathrm{Fm,defect}}$ is the formation energy of the defect cluster and $E_{\mathrm{Fm,iso}}$ is the formation energy of each isolated constituent impurity. E_{b} is negative for bound systems.

Facile calculations of the excitation energy μ_{e} of electron donor and acceptor impurities are hampered by a combination of limited supercell sizes causing effective dopant concentrations in the region of thousands of parts per million; and the inherent limitation of exchange functionals in DFT causing underestimation of the band-gap [145]. The use, in this work, of large supercells and hybrid functionals that incorporate part of the Fock exchange energy mitigates this issue somewhat. This allows many systems to be adequately analysed from their density of states (DOS) spectra. Nevertheless, the problem remains for defects with small μ_e; for this reason here the DOS results from CRYSTAL14 are compared with results of the *empirical marker method* (EMM), which has been successfully used to compare activation energies of diamond dopants, dopant pairs and multi-dopant clusters [55, 146].
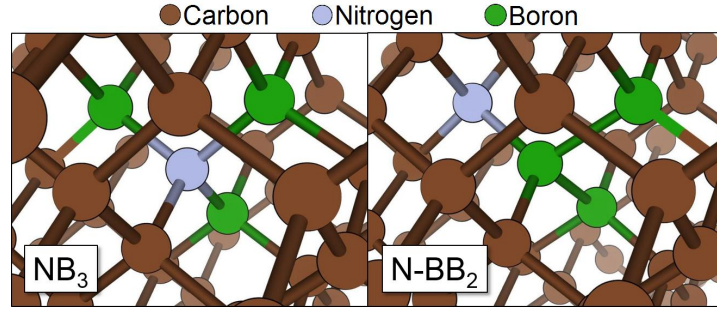
Figure 3.1: Two stoichiometrically identical but structurally distinct clusters, NB_3 and N-BB_2. The former is an example of a 'symmetric' boron-rich cluster in which the minority foreign (N) atom is in a central position, and the latter an example 'asymmetric' cluster in which the minority foreign atom is in a peripheral position.

To carry out the EMM, the CASTEP code [147] used the generalised gradient approximation (GGA) of Perdew, Burke and Ernzerhof [98]. The calculation parameters were, where possible, the same as those of the HSE-06 calculations as outlined above, but with a plane-wave valence basis set of energy up to 800 eV and ultra-soft core electron pseudopotentials [106].

Due to its large basis set, CASTEP is unable to undertake hybrid functional calculations for these systems, but it does provide a good confirmation of the structural results and a means to compare neutral charge states with positive or negative charge states of a supercell. Using charge calculations, the EMM provides a simple and effective indicator of the acceptor or donor (d) level by comparison to a reference (r) state:

$$(3.3) \qquad \mu_{e,d} = \mu_{e,r} - \left[(E_d^0 - E_d^+) - (E_r^0 - E_r^+) \right]$$

where $\mu_{e,d}$ and $\mu_{e,r}$ refer to the excitation energy of the dopant and reference respectively, and E^0 and E^+ to the energy of the neutral and charged state respectively. Here the example is of a donor, giving positively charged states, but the method is equivalent for acceptors in negatively charged states. The 'markers' used here for acceptors and donors are boron and nitrogen respectively, owing to their similar values of μ_e to many of the examined clusters.

3.3 Results and discussion

The notation used here for identifying a cluster is similar to that used in the literature [55]. For example the A-centre, or nitrogen substitutional pair, is denoted N_2. Additionally,

to distinguish between clusters of equal stoichiometry but distinct atomic arrangement, some clusters are denoted in a form similar to that for B-N-N, avoiding confusion with BN_2, which is itself labelled N-B-N. Clusters of equal stoichiometry but differing atomic arrangement are distinguishable by the terms 'symmetric' and 'asymmetric'. A further stoichiometric pair is presented figure 3.1.

3.3.1 Defect structures

Figure 3.2 shows the HSE-06 boron-nitrogen cluster structures, with a summary of the data shown in table 3.1. Before geometry relaxation, slightly off-setting the atomic position from the undefective lattice position avoids dopants relaxing into geometric local energy minima. For the isolated nitrogen defect this procedure yields the well-known C_{3v} symmetric state in which one N-C bond is elongated relative to the perfect diamond bond length (C-C_p = 1.55 Å) to 2.04 Å and the other three shorten to 1.47 Å, reflecting the 'lone pair' of electrons on sp^3 hybridised N.

A similar C_{3v} relaxation occurs for single substitutional boron, but with a slight elongation compared to C-C_p even in the shorter three bonds due to the large covalent radius of boron. That said, all changes in bond lengths for the boron dopant are minor.

The same reduction in symmetry does not occur for homonuclear pairs of boron or nitrogen, both of which retain D_{3d} symmetry. The N-C bonds in N_2 are further contracted compared to those of N at 1.45 Å, reflecting a strong repulsion of the two nitrogen atoms, 2.21 Å apart. Again, a similar situation occurs in B_2, with a B-B bond length of 2.03 Å.

While the homonuclear pairs repel, the heteronuclear pair BN, which is isoelectronic with CC, barely causes a bond length change, with the B-N bond only longer than C-C_p by 3 %. The satisfaction of valencies in the BN pair also causes the bonds from B and N to the surrounding carbon atoms to be far closer in length to C-C_p.

Unlike some previous authors [49, 51] the present hybrid calculations find the symmetry of N-B-N to be C_s rather than C_{2v}, as in the unrelaxed case. This symmetry lowering is due to an elongation of a carbon-nitrogen bond on one nitrogen atom, causing a surrounding distortion much like that for N. The N-B-N centre may be considered as a 'separate' N adjacent to a valence-satisfied BN. Similarly, in the B-N-N centre the outer nitrogen atom behaves much like a single N, with its three carbon bonds shorter than C-C_p by 4 % and the remaining bond (to nitrogen) longer by 30 %, 2.01 Å.

Unlike the nitrogen-rich 3-atom clusters, B-N-B and B-B-N are vastly less structurally different from intrinsic diamond itself with a maximum X-C bond length change of 3 % relative to C-C_p and the inter-boron bond in B-B-N (1.76 Å) being less than half as
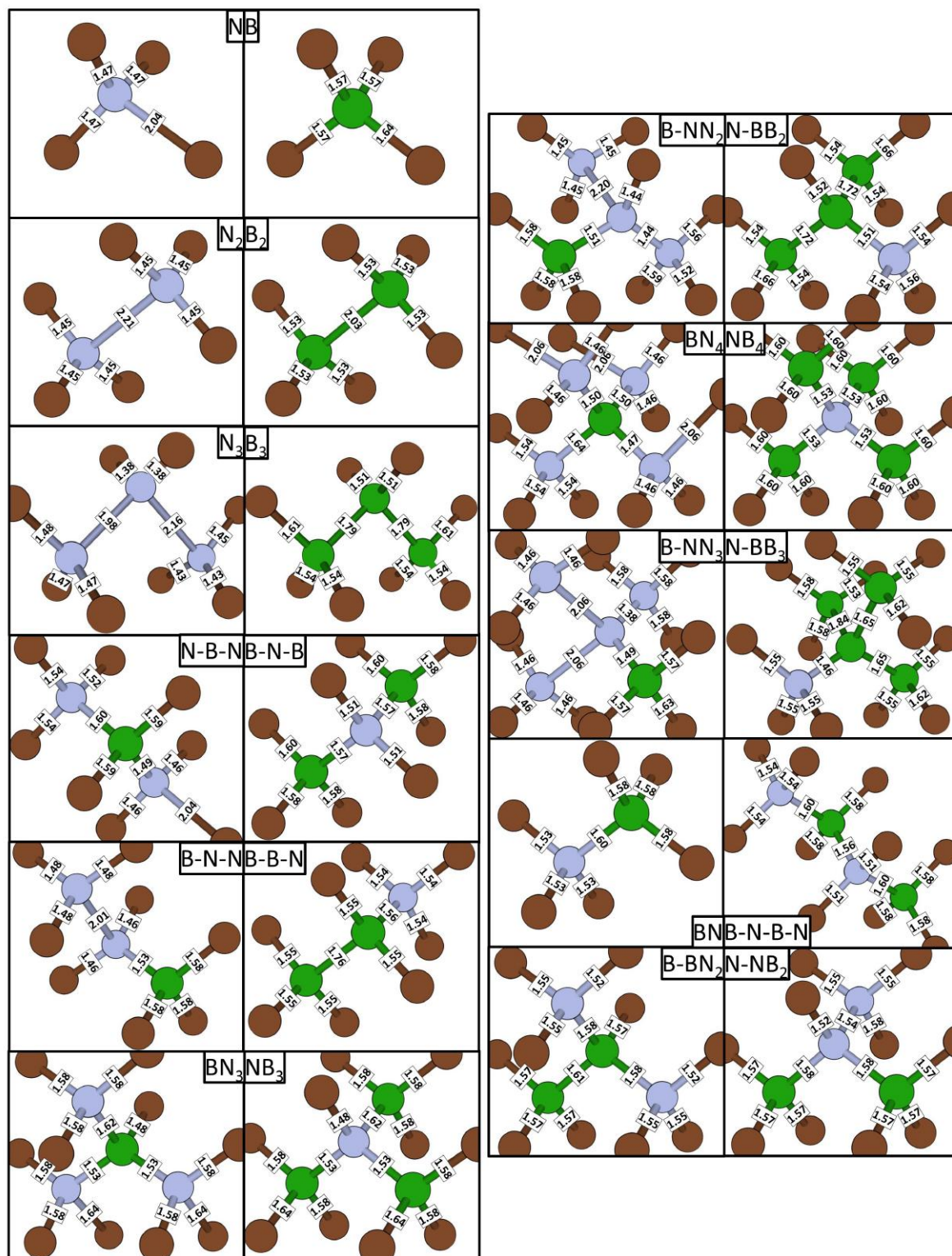
Figure 3.2: Bond lengths (Å) of B- and N-rich clusters with $n \leq 3$. All separations involving dopant atoms (i.e. all but C-C) are shown.

Table 3.1: Lowest energy spin-state symmetry and structural results for the clusters examined by HSE-06 calculations. Symmetries before and after the geometries are optimised from perfect lattice positions to their ground states are denoted Unopt and Opt respectively. Bond lengths are given in units of the calculated perfect diamond carbon-carbon bond length $C\text{-}C_p$, 1.55 Å, followed by a bracket containing the number of bonds of the given length stemming from each central atom: for example "1.02 (3,1)" under the C-B heading refers to four bonds 2 % longer than those of perfect diamond, three originating at one boron atom and one at another, each to a carbon atom. †C-B bond lengths differ by less than 1 %, making the symmetry almost C_{2v}

n	Cluster	Spin	Symmetry Unopt	Symmetry Opt	Bond length / $C\text{-}C_p$ C-N	C-B	B-N	N-N	B-B
1	N	1/2	T_d	C_{3v}	0.95 (3) 1.32 (1)	—	—	—	—
	B	1/2	T_d	C_{3v}	—	1.02 (3) 1.06 (1)	—	—	—
2	N_2	0	D_{3d}	D_{3d}	0.94 (3,3)	—	—	1.43 (1)	—
	B_2	0	D_{3d}	D_{3d}	—	0.99 (3,3)	—	—	1.31 (1)
	BN	0	C_{3v}	C_{3v}	0.99 (3)	1.02 (3)	1.03 (1)	—	—
3	N-B-N	1/2	C_{2v}	C_s	0.94 (2) 1.32 (1) 1.00 (2) 0.98 (1)	1.03 (2)	1.03 (1) 0.96 (1)	—	—
	B-N-N	1/2	C_s	C_s	0.96 (3) 0.94 (2)	1.02 (3)	0.99 (1)	1.30 (1)	—
	B-N-B	1/2	C_{2v}	$C_s^†$	0.98 (2)	1.02 (2,2) 1.03 (1,1)	1.02 (2)	—	—
	B-B-N	1/2	C_s	C_s	1.00 (3)	1.00 (3,2)	1.01 (1)	—	1.14 (1)
	N_3	1/2	C_{2v}	C_s	0.95 (2) 0.96 (1) 0.92 (2) 0.94 (1) 0.89 (2)	—	—	1.40 (1) 1.28 (1)	—
	B_3	1/2	C_{2v}	C_{2v}	—	1.00 (2,2) 1.04 (1,1) 0.98 (2)	—	—	—
4	$B\text{-}BN_2$	0	C_s	C_s	1.00 (2,2) 0.98 (1,1)	1.02 (3,1)	1.02 (2)	—	1.04 (1)
	$N\text{-}NB_2$	0	C_s	C_s	1.00 (2) 1.02 (1) 0.98 (1)	1.02 (3,3)	1.02 (2)	1.00 (1)	—
	B-N-B-N	0	C_s	C_s	1.00 (3) 0.98 (2)	1.02 (3,2)	1.03 (2) 1.01 (1)	—	—
	BN_3	1	C_{3v}	C_1	1.02 (3,2,2) 1.06 (1,1)	0.96 (1)	0.99 (2) 1.05 (1)	—	—
	$B\text{-}NN_2$	0	C_s	C_1	0.93 (3,1) 1.03 (1) 1.01 (1) 0.98 (1)	1.02 (3)	0.98 (1)	1.42 (1) 0.93 (1)	—
	NB_3	0	C_{3v}	C_s	0.96 (1)	1.02 (3,2,2) 1.06 (1,1)	0.99 (2) 1.05 (1)	—	1.11 (2)
	$N\text{-}BB_2$	0	C_s	C_s	1.00 (2) 1.01 (1)	1.00 (2,2) 1.07 (1,1) 0.98 (1)	0.97 (1)	—	—
5	BN_4	3/2	T_d	C_1	0.94 (2,2,2) 1.33 (1,1,1) 1.00 (3)	—	0.97 (2) 1.06 (1) 0.95 (1)	—	—
	$B\text{-}NN_3$	1/2	C_{3v}	C_s	0.94 (3,3) 1.02 (3)	1.02 (2) 1.05 (1)	0.96 (1)	1.33 (2) 0.89 (1)	—
	NB_4	3/2	T_d	T_d	—	1.03 (3,3,3,3)	0.99 (4)	—	1.07 (2)
	$N\text{-}BB_3$	1/2	C_{3v}	C_s	1.00 (3)	1.00 (2,2) 1.05 (1,1) 1.02 (2) 0.99 (1)	0.94 (1)	—	1.19 (1)

extended as that in B_2 (2.03 Å). Relative to C-C_p the boron-carbon bonds in B-N-B are extended by only around 1 %, resulting in a relaxed geometry with C_{2v} symmetry.

Of the clusters containing two nitrogen atoms and two boron atoms, B-BN_2, N-NB_2 and B-N-B-N, little structural change from perfect lattice positions is apparent. All have low symmetry, C_s, simply due to their atomic arrangement. Addition of a compensating atom to the three-atom clusters clearly reduces the resulting structural changes considerably.

The most stable spin state of BN_3 is 1 due to the two extra electrons added by nitrogen atoms not directly bonded to one another. This results in C_s symmetry with one nitrogen having all three of its C-N bonds extended by 2 % relative to C-C_p and the other two N atoms with one C-N bond longer still, at 6 %. Unlike BN_3, asymmetric B-NN_2 has a low spin ground state and its symmetry is just C_1. The two distances between the central and outer nitrogen atoms differ hugely: 1.44 and 2.20 Å.

By contrast the boron-rich four atom clusters deviate from high symmetry only slightly. A small shift, mainly in the positions of two B atoms in NB_3, causes a reduction of symmetry from C_{3v} to C_s, retaining one mirror plane. The three boron atoms in N-BB_2 perform a scissor motion during relaxation, maintaining a mirror plane while increasing the inter-boron distance and reducing the boron-nitrogen bond length.

In its lowest energy state of spin $\frac{3}{2}$, the BN_4 cluster has three nitrogen atoms with one C-N bond far longer than the other two whilst the fourth N remains close to its lattice position. The movement of the three N atoms is accompanied by a shift of the central boron from its 3-fold symmetric position. This results in a complete loss of symmetry during relaxation. B-NN_3 is spin $\frac{1}{2}$, also with a symmetry of C_s. Two peripheral nitrogen atoms in B-NN_3 move away from the central N during relaxation, causing mirror symmetric elongations of the two N-N distances and leaving the central nitrogen coordinated to the neighbouring boron and one remaining nitrogen.

Despite sharing the same spin as its nitrogen-rich counterpart, the NB_4 ground-state, unlike BN_4, maintains tetrahedral symmetry with minor strain in all bonds compared to the perfect lattice. The ground state of N-BB_3, on the other hand, is spin $\frac{1}{2}$ and the B-B bond lengths are much the same as in the smaller N-BB_2 cluster, the additional boron atom sitting on the mirror plane in a peripheral position.

3.3.2 Energetics

Figures 3.3 and 3.4 show the HSE-06 structural energetic data for the range of nitrogen-rich and boron-rich defects, respectively, with both the formation energy (E_{Fm}) and
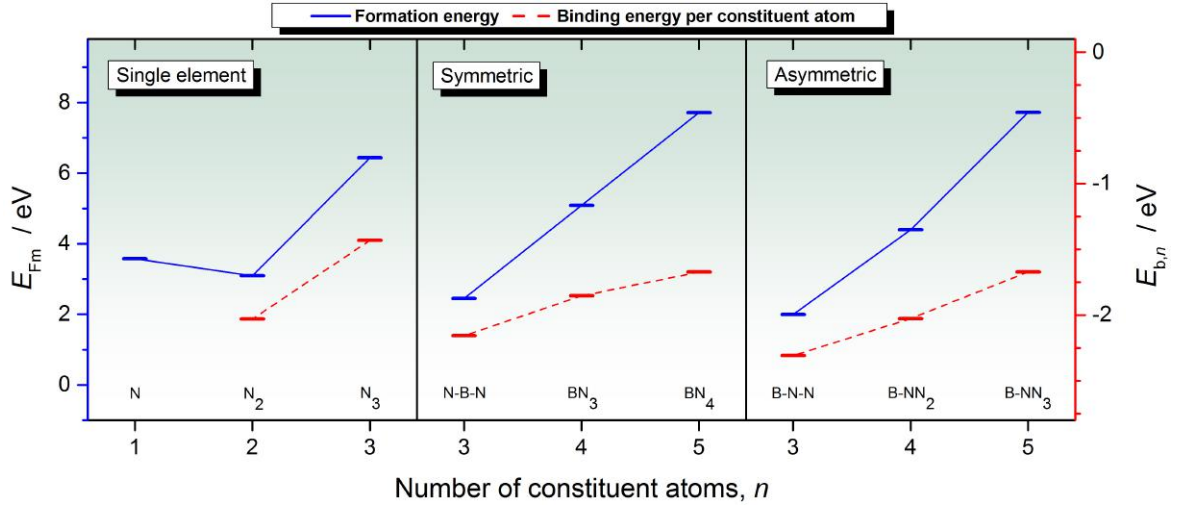
Figure 3.3: Plots of formation energy E_{Fm} and binding energy per constituent atom $E_{\mathrm{b},n}$ against n for the nitrogen-rich single element, symmetric and asymmetric clusters. Note that the $E_{\mathrm{b},n}$ axis (right) is set to the same range as figure 3.4, but the E_{Fm} axis (left) is scaled to best represent the E_{Fm} range. Present as guides to the eye, the solid blue and dashed red lines connect E_{Fm} and $E_{\mathrm{b},n}$ values respectively.

binding energy per constituent atom ($E_{\mathrm{b},n}$). For single N and B dopants only E_{Fm} applies, and the values of 3.58 and 1.77 eV respectively agree well with those published previously [148]. When considering the energetics of N or B atom loss from dopant clusters, the scope here is limited to single atom losses since dopants are considered unlikely to migrate in cluster form.

The binding energies of the single-element pairs, N_2 and B_2, are -4.06 and -1.29 eV respectively, also in excellent agreement with the results of previous researchers [146]. The binding energy of N_2 reflects the tendency of type I diamond to accommodate A-centres.

When n increases in single-element clusters from 2 to 3, we find an increase in formation energy and less well-bound clusters. For nitrogen, this is in part due to the formally unsatisfied valencies causing an energetically expensive symmetric distortion of both N-N bonds; in N_2 the inter-nitrogen distance may be large, but the valencies are satisfied.

Figure 3.5 shows the structural energetic data for clusters containing equal numbers of boron and nitrogen atoms. A simple defect with a large binding energy of -5.52 eV and even a negative formation energy of -0.17 eV, the BN defect is a potentially present cluster in multiple types of diamond.
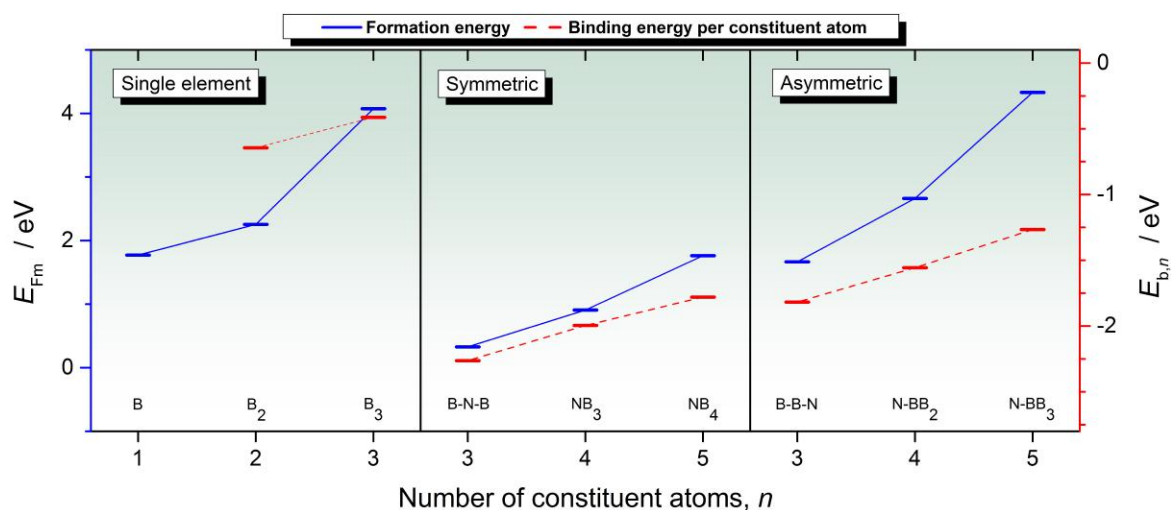
Figure 3.4: Formation energy E_{Fm} and binding energy per constituent atom $E_{\mathrm{b},n}$ against n for the boron-rich single element, symmetric and asymmetric clusters. Notes on scale and lines are the same as in figure 3.3.
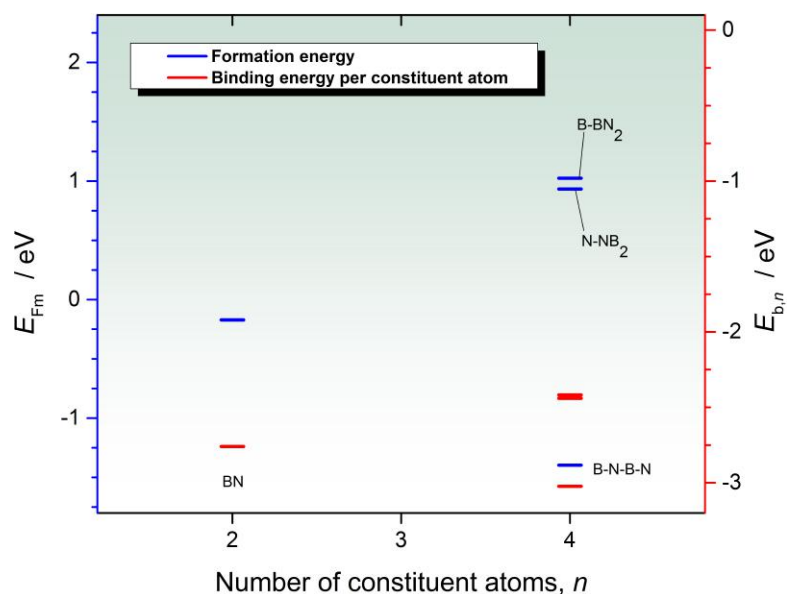
Figure 3.5: Formation energy E_{Fm} and binding energy per constituent atom $E_{\mathrm{b},n}$ against n for the four equal boron-nitrogen clusters. Notes on colours are the same as in figure 3.3, but the $E_{\mathrm{b},n}$ scale is different.

The binding energies of N-B-N and B-N-N differ by 0.46 eV, in agreement with previous work [55]. Addition of further nitrogen atoms to these clusters renders them less stable, with the asymmetric case being more stable than the symmetric for $n = 4$. By contrast for $n = 5$ the symmetric spin $\frac{3}{2}$ cluster, BN_4, is almost energetically equal to its asymmetric, spin $\frac{1}{2}$, counterpart. Relaxation of three N atoms in BN_4 results in shorter and stronger bonds with both the central boron and two of their three nearest-neighbour carbons. The asymmetric cluster $B-NN_3$ does not similarly relax: the central N atom shares no bonds with C atoms so cannot make the single C-N bond elongation made by N atoms in many clusters.

The boron-rich clusters lack the lone pair electron density present in their nitrogen-rich analogues. Positioning a nitrogen atom at the centre of a cluster causes stabilisation with respect to both B_{n-1} plus isolated nitrogen and to clusters with peripheral N atoms for all values of n. Interestingly, the formation energies of the asymmetric clusters for $n = 3$ to 5 are comparable to those of the $n = 1$ to 3 single element boron clusters. Once formed however, these clusters are more tightly bound than B_x because of the high energy associated with forming a single N centre. The largest difference in formation energy between two boron-rich clusters that differ in content by one boron atom is 1.82 eV between B_3 and B_2, so that the dissociation of B_3 to form B_2 and B is exothermic by 0.1 eV. All other boron-rich clusters are stable with respect to loss of boron [149].

In general the boron-rich clusters are less distorted than the nitrogen-rich clusters, resulting in lower formation energies, but have similar binding energies due to the accommodation of single nitrogen defects being very endothermic. For both boron- and nitrogen-rich clusters the number of constituent atoms with largest $E_{b,n}$ is three, provided they have an accompanying atom of the other element. Comparing $B-BN_2$ and $N-NB_2$ with BN, and N_2 with BN_3 and $B-NN_2$, it appears that the addition of a BN unit usually causes only small changes in $E_{b,n}$ when nitrogen is present in the cluster. B-N-B-N is likely to outnumber its more compact counterparts with the same stoichiometry as its binding energy significantly outweighs theirs; it having the most negative binding energy of any cluster examined here.

The asymmetric N-rich clusters are more stable than the corresponding symmetric clusters for $n = 3$ and 4, and BN_4 and $B-NN_3$ are almost energetically equal. This may result in a greater concentration of BN_4 than its smaller counterparts since, for example, an isomeric rearrangement of BN_3 favourably results in $B-NN_2$ formation. Given this, there may not be a clear route to BN_4 formation via addition of N atoms to smaller clusters, despite its stability.

Under thermodynamic control and for given appropriate dopant concentrations the clusters with the most negative binding energy will prevail. Considering the tendency of nitrogen to cluster, a co-doped N-rich sample might contain some combination of (for example) N-N-B, B-NN$_2$, BN$_4$ and some purely N containing clusters, depending on the ratio of nitrogen to boron.

For boron-rich clusters the structures involve atomic separations and geometries more similar to those in the perfect diamond lattice. This gives both low formation energies and high stabilities of clusters with multiple boron atoms. The low energy required to produce a single boron defect results in the instability of the B$_3$ complex with respect to loss of B, but all other examined boron-rich clusters lack an exothermic destruction pathway [149]. The symmetric boron-rich clusters are all more stable than the asymmetric clusters. Additionally, unlike their N-rich counterparts the NB$_x$ defects have large E_b values relative to the single element defects.

Thermodynamic control may cause relaxation into global energy minima, but another factor in the free energy of a system is entropy. Entropy is not considered in the current energetic speculations and may play a role during HPHT treatment, possibly causing smaller clusters and even single substitutional dopants as temperatures are increased. For example, the B$_2$ cluster is theoretically bound only up to 750 K [150], largely due to the effect of entropy being more prominent at high temperature. That said, all defects incorporating nitrogen studied here are predicted to have much larger E_b values than that of B$_2$. It is therefore likely that boron-rich co-doped diamond might produce some of the symmetric NB$_x$ clusters with $x = 1$ to 4 during HPHT preparation, with entropy possibly favouring lower x values over larger clusters.

This work considers entirely neutral species when calculating binding energies. This may not be applicable to a material containing both nitrogen and boron since, when they coexist, it is energetically favourable for a single nitrogen centre to donate an electron to a single boron centre. In this case each calculation of binding energy would involve the energy of a positive nitrogen centre, N$^+$, and a negative boron centre, B$^-$, each replacing one of their neutral counterparts (or two in those with 2 of each element). The energy differences between neutral and charged N and B are known, 1.70 and 0.37 eV respectively. Subtracting these from the band-gap of diamond gives 3.40 eV, an amount by which each co-dopant cluster binding energy would be raised (made less negative). None of the studied clusters become unbound by this change, but it may mean some are less favourable in an experimental system than is apparent from considering purely neutral species.

One further consideration for HPHT preparation of these clusters is non-ground-state spin. At the high temperature used, kT will lie in the approximate range $0.15 - 0.2$ eV. NB_3 has spin states (0 and 1) that differ by 0.2 eV, the upper end of this scale. The BN_3 and NB_4 ground-states, spin 1 and $\frac{3}{2}$ respectively, lie below their higher energy spin states by around 2 to 3 times kT. Each of the other clusters have far larger energy gaps between their spin states, making them unlikely to occupy the higher energy state upon preparation by HPHT.

3.3.3   Excitation energies

CRYSTAL HSE-06 DOS spectra show the difference between the mid-gap levels and the relevant band: the conduction band minimum (CBM) for donors and the valence band maximum (VBM) for acceptors. From these levels the excitation energy of a defect μ_e can be obtained. Advantages of this method include that it relies on no empirical input, so is a truly *ab initio* technique, and that it only provides levels within the band-gap, unequivocally providing results on defects of interest. Disadvantages include the *slightly* narrow diamond band-gap obtained by calculations using HSE-06, here 5.2 eV (compared to 5.5 eV experimentally), increasing the likelihood of metallic DOS spectra. Additionally, unrealistically high impurity concentrations cause degenerate doping; diamond supercells examined with 1 defect in 512 atoms have concentrations as high as 3.5 $\times 10^{20}$ cm^{-3}.

The EMM results complement the HSE-06 data, and have the advantage that even shallow excitation energies can be obtained. Its comparative nature means calculations on high concentrations can give reasonable results provided the supercell is large enough that charged states do not result in unphysical geometries. Using an experimental marker, it is of course not a truly *ab initio* method.

With their respective advantages and disadvantages, neither of the two methods would be appropriate to consider the large range of defects in this work comprehensively. Whilst the levels obtained from the two methods are rarely identical, they are sufficiently similar that comparison provides justifiable insight. Table 3.2 shows the HSE-06 and EMM results for a range of well studied diamond dopants. The combination of both methods is invaluable when considering shallow-level defects, as exemplified by B and P, where the DOS method is unreliable in quantifying the excitation energy.

An example (N_2) density of states spectrum is shown in figure 3.6. Examination of the band-gap region allows quantification of the electrical levels owed to dopant clusters. Specifically for N_2, the donor level is calculated from the difference between the average

Table 3.2: Excitation energy μ_e for various substitutional acceptors (A) and donors (D) in diamond, calculated by both the HSE-06 DOS method and the EMM. "M" refers to a level producing a metallic DOS from which the value cannot be derived.

Dopant	Type	HSE-06 μ_e / eV	EMM μ_e / eV	Literature μ_e / eV
B	A	M	$0.37^\dagger$	0.37, [151]
Al	A	0.94	0.82	1.0, [148]
Li	A	1.48	1.62	1.4, [152]
N	D	1.65	$1.70^\dagger$	1.70, [139]
P	D	M	0.74	0.60, [41]
S	D	1.57	1.38	1.2, [153, 154]
O	D	2.18	2.63	2.5-2.7, [154]

†Levels used in the EMM as empirical markers
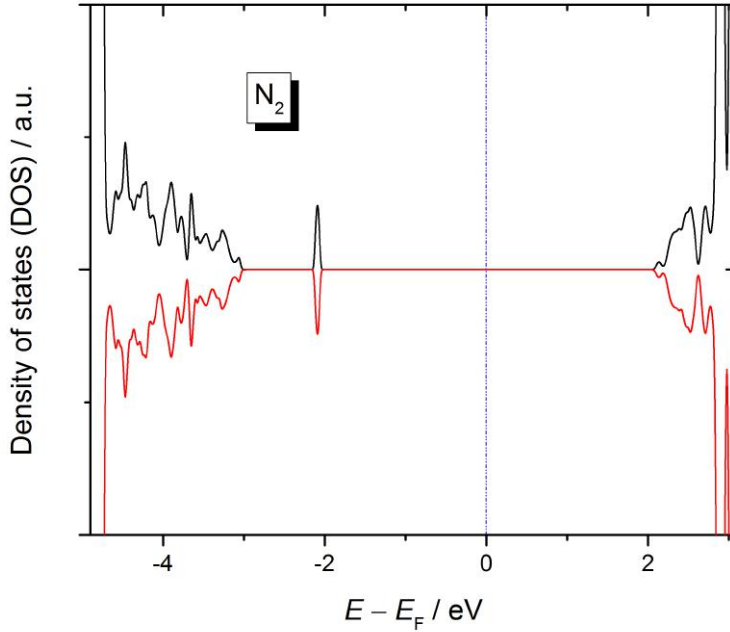
Figure 3.6: Density of states spectrum of the N_2 defect in the vicinity of the diamond band-gap, showing both up (black) and down (red) spin density, which are equal in this overall spin-0 system. The vertical blue line indicates the Fermi-level (E_F).

energy of the mid-gap state and the CBM. The other nitrogen-rich defect μ_e values are similarly calculated from the CBM, while the boron-rich cluster μ_e values are derived from their proximity to the VBM.

μ_e of the N-rich donor clusters and B-rich acceptor clusters are shown in figures 3.7 and 3.8, where the values are given with respect to the CBM and VBM for donors and acceptors respectively. Excluding those acceptor levels too shallow to determine by the DOS method, the two methods tend to agree well. Values for previously studied examples
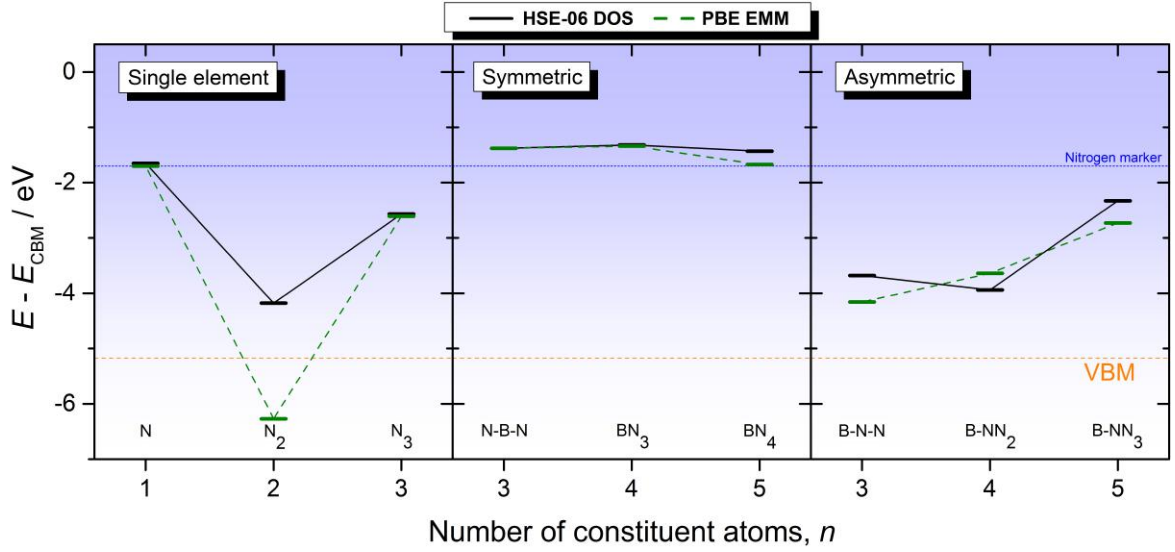
Figure 3.7: Nitrogen-rich cluster donor levels against n for both the HSE-06 density of states method (black solid lines) and the PBE empirical marker method (green dashed lines). The nitrogen EMM marker and the VBM are given for reference.

such as N_2, B_2, N-B-N, and B-N-N are in good agreement with the literature [55, 146].

The trends apparent in the N-rich and B-rich plots somewhat mirror each other, as is expected from sets of clusters that differ fundamentally from each other only in their higher or lower electronic and nuclear charges. For example, the *pure* elemental defects with $n = 1$ to 3 show a shallow-deep-medium pattern in both boron and nitrogen. When $n = 2$ two half-spin defects combine to make a zero total spin ground-state, stabilising the associated negative or positive charge and its band-gap state and thereby requiring more energy to remove the electron or hole from the respective nitrogen or boron defect. The $n = 2$ level is thus deeper than $n = 1$. The $n = 3$ cluster may be considered a spin 'mixture' of $n = 1$ and 2. This spin dictated progression is also apparent in the boron-rich $n = 3$ to 5 clusters.

One striking difference between nitrogen-rich and boron-rich clusters is the asymmetric $n = 3$ and 4 clusters. While B-N-N and B-NN$_2$ have similar μ_e, B-B-N has a shallower level than N-BB$_2$. The former is likely to be associated with the smaller structural distortion in B-N-N relative to B-NN$_2$ and its effect on the nitrogen electron density. There is no analogous effect in the boron-rich clusters.

For symmetric nitrogen-rich clusters with $n = 3$ to 5, addition of N atoms does not significantly reduce μ_e as might be expected. The same is not true of the asymmetric versions, where each nitrogen addition reduces the donor excitation energy. This difference
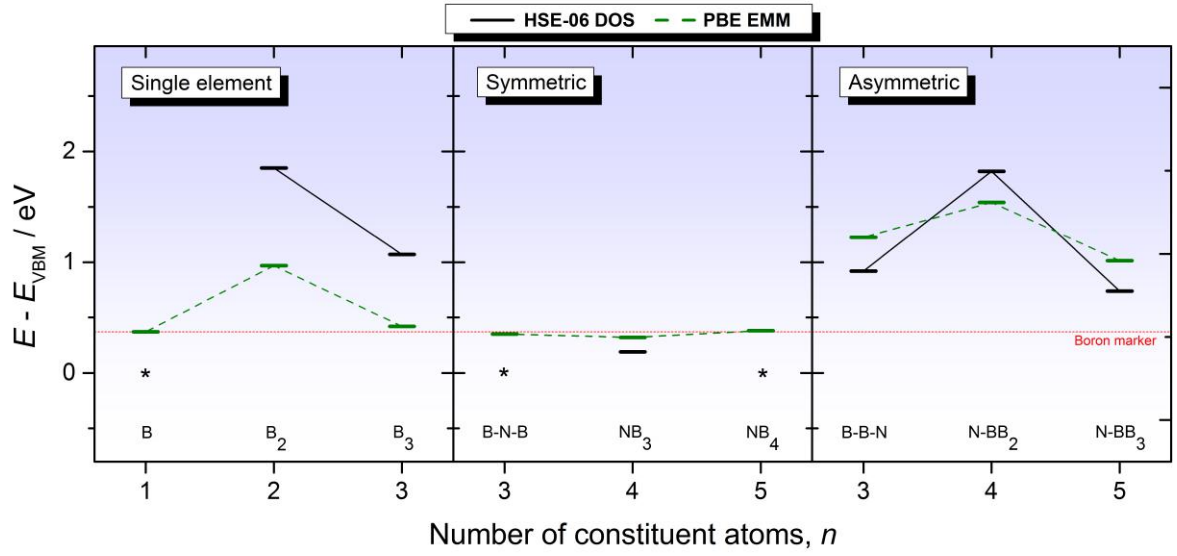
Figure 3.8: Boron-rich cluster acceptor levels against n for both the HSE-06 density of states method (black solid lines) and the PBE empirical marker method (green dashed lines). The boron EMM marker is given for reference. A star denotes a metallic DOS spectrum from which the level cannot be ascertained.

can be understood by considering N-B-N as $(NB)^0$-N^0 and B-N-N as B^--N_2^+ [55]. Addition of N atoms to the former simply causes further N^0 centres in (very) close proximity to an existing deep donor defect. On the other hand, addition of N atoms to the asymmetric cluster causes further concentration of electron density in the already negative region of the donor cluster. This stacking of negative charge pushes the associated level to higher energies and makes donation of an electron more favourable.

As donors, the symmetric N-rich clusters have similar μ_e values to the single nitrogen centre and the asymmetric N-rich clusters have deep levels. With the range of defects that could be present, a HPHT prepared material would maintain a range of levels within the band-gap, which if detectable may be difficult to interpret.

μ_e for the boron-rich clusters are all lower than the equivalent nitrogen-rich defects. The band-gap levels of the stable symmetric clusters would even be similar to that of the single boron impurity, so might be indistinguishable by some experimental techniques. These defects could already exist in some natural or HPHT type II-b diamond.

3.4 Conclusion

3.4.1 Summary

In an effort to understand how two co-dopants might behave in diamond, this chapter
presents an analysis of a broad range of substitutional boron-nitrogen clusters using
hybrid DFT calculations. Ground-state geometries and both structural and electronic
energies are discussed in detail. A comparison of the CRYSTAL14 HSE-06 electronic
energy levels with those determined by the EMM using CASTEP shows good agreement.

Electron density in the nitrogen-rich clusters leads to large local geometric distor-
tions, low symmetries, high formation energies and deep band-gap states. Nevertheless,
nitrogen-rich clusters are strongly bound and are stable with respect to loss of nitrogen.
Depending on preparation conditions, the asymmetric N-rich clusters will play a part in
nitrogen-rich co-doped material.

In contrast, the boron-rich clusters lead to smaller bond length changes compared to
pure diamond, are all (apart from B_3) stable with respect to loss of boron atoms [149]
and to formation of pure boron clusters. Those of highest stability, NB_x, have electronic
energy levels comparable to that of B.

Comparison of clusters containing both boron and nitrogen to those containing
only one element shows, in almost every case, that the two co-dopants cause mutually
enhanced stability. This has implications for HPHT grown material, since the likelihood
of boron and nitrogen co-existing within it is high. Detection of some clusters, such as
the symmetric NB_x and BN_x groups, might prove difficult since the charge excitation
energies are similar to those of the well known single elemental dopants.

3.4.2 Future work

Progress in computational projects will be enhanced by future computational power
increases. Larger supercomputing clusters will allow supercells of ever greater numbers
of atoms to be modelled. This will allow relatively near-future work on this type of project
to study systems containing 1 defect in 1000 atoms ($6 \times 6 \times 6$ conventional unit cells).
Eventually, the concentration of defects in the largest supercells will be realistic, allowing
simulation of semiconducting material. From DOS calculations on these sized cells the
excitation energies of even shallow donor and acceptor levels might be accessible.

With the exception of B-N-B-N the clusters studied here have contained atoms no
further from each other than two bonds. If this rule was relaxed there might be further

structures worth considering. Additionally, structures involving H atoms, interstitials and/or vacancies are important considerations for predictions of realistic materials since each can alter the properties of an associated defect.

If experimental efforts in production of clusters make progress, then computational modelling might offer some help in analysis of some detection techniques. Both CASTEP and CRYSTAL have functionality allowing the user to generate various spectra that would be produced by the examined material, for example for infra-red, nuclear magnetic resonance and electron energy loss spectroscopies.

SPECTROSCOPIC INVESTIGATION OF B/N/H/C MICROWAVE ACTIVATED CVD PLASMAS

4.1 Introduction

A convenient property of diamond CVD plasmas, that they emit light, has been used in their characterisation for many years. Optical emission studies range from simple monitoring of a spectral peak to confirm the presence of a species of interest [155] to extensive spectroscopy combined with kinetic models [69, 156], aiming to dissect the chemistry of the plasma.

Other techniques used to characterise CVD systems have included resonance-enhanced multi-photon ionisation (REMPI) studies of hot-filament assisted CVD reactors [157] and cavity ring-down [absorption] spectroscopy (CRDS) of microwave-plasma enhanced CVD reactors [158], both techniques that quantify the concentration of gaseous species in the chamber.

Many OES studies on nitrogen containing plasmas have correlated CN emission with some characteristic of grown material [159–162], but since, unlike REMPI and CDRS, OES is strictly a non-quantitative method, without either a complementary quantitative technique or a comprehensive model of chemical processes few conclusions can be drawn about the chemical role of nitrogen-containing species.

Other researchers have introduced both N- and B-containing gases to the plasma input gas. Notably, experimental work by Sartori et al. [83, 84] has shown that trace

levels of boron containing gas in the process mixture suppresses the growth-rate increase commonly experienced by growers using ppm levels of nitrogen. This work, however, finds no influence of N_2 or B_2H_6 on their counterpart's studied optical emission species, BH or CN respectively, at the explored concentrations. Additionally, modelling has been carried out by Liang et al. [163] that incorporates both N and B species, but finds little interdependence between them. Both of these studies are discussed further later in this chapter.

Individually, boron and nitrogen have seen extensive research in MP-CVD plasma diagnostics. With a view to comprehensively understand the role of dopants in microwave reactors, the groups of Prof. Mike Ashfold in Bristol and Dr. Alix Gicquel in Paris have performed extensive studies on MP-CVD reactors using combined OES, absorption spectroscopy (either CRDS or a similar 'tunable diode laser absorption spectroscopy', TDLAS) and kinetic reaction modelling on boron [164–167] and nitrogen [114, 168] containing plasmas. The influence of boron and nitrogen additions on the process conditions are well characterised by their three-technique method, allowing an understanding of the data in this chapter by reference to the previous work.

The lack of interaction of boron- and nitrogen-containing species found by previous optical studies can be attributed to either narrow parameter space or experimental inaccuracies, since diborane and nitrogen are known to interact in boron nitride producing plasma deposition systems [169]. In this chapter, a larger parameter space is combined with detection of numerous plasma species to further explore the boron-nitrogen interaction in CVD plasmas. The effects of co-introduction of diborane and nitrogen gases are rationalisable by hypothesis of the interactions of known reactive N and B containing species and by analogy to hydrocarbon chemistry.

4.2   Experimental methods

In the work carried out for this chapter the reactor (as shown in figure 2.2) contained a 1.25 " tungsten disk on top of a 0.009 " wire, with no additional substrate on top. The chamber was cleaned prior to beginning the project and good sealing was checked to ensure minimal air contamination. The reactor remained closed until the data collection was complete.

During the experiment, hydrogen (N7; generated by electrolysing (Milli-Q purified) water in a Noblegen H_2 generator; MicroPROGEL, UK) is introduced at a flow of 300 sccm. When required, up to 12.5 sccm (4 %) CH_4 (N5.5; Air-Liquide, UK) is introduced. Ni-

Table 4.1: Details of spectroscopic data acquisition for each region of interest in the emission spectrum.

Region	Grating / lines mm^{-1}	Centre Wavelength / nm	Acquisition time / min
N$_2$ and NH	1200	335	25
BH and CH	1200	435	10
B	1200	250	8
CN	1200	385	5
Wide	300	500	3

trogen (N5.5; Air-Liquide, UK) and diborane (100 ppm in H$_2$; N6; Air-Liquide, UK) are introduced when appropriate, up to a concentration in the total gas composition of 3.2 % and 15 ppm respectively whilst the total hydrogen flow is kept constant. Flow rates are controlled by a range of mass flow controllers (MFCs; Tylan, UK or MKS, UK) which are in-turn set by a MFC controller (MKS, UK) in the rack. Pressure, set to 150 torr at normal operating conditions, is maintained by a butterfly valve (MKS, UK) and exhaust valve controller (MKS, UK) through a P-I-D feedback loop. A magnetron provides 2.45 GHz microwave radiation powered by a 1.5 kW supply (ASTeX, US), and is set to 1.5 kW at normal operating conditions. The aluminium chamber is cooled by mains water flow, monitored by flow-meters (Kobold, UK), and the quartz window by continuous air flow.

Experimental process parameters include B$_2$H$_6$, N$_2$ and CH$_4$ concentrations, from 0 to 15 ppm, 3.2 % and 4 % respectively. Each change in gas flow was followed by 10 minutes of non-acquisition time, to allow the reactor to reach a steady state, apart from for changes in B$_2$H$_6$ flow when, due to an increased time taken to reach a steady state [69], a 30 minute period was used.

Height resolved spectroscopic data was collected by the Shamrock Andor spectrometer described in section 2.3.2 and shown in figure 2.4. Two-dimensional spectral images were acquired by the CCD, cooled to - 50 ^{o}C, and visualised on a PC with the Andor Solis software package, an example of which is shown in figure 4.1A. This example is for the 435 nm centred BH region, which also contains CH emission.

The 6 species emissions detailed in table 2.1 were monitored by positioning the diffraction grating such that the CCD recorded spectra centred at five different positions, for times appropriate to gather data with sufficient signal-noise ratio. These parameters are defined in table 4.1. The 1200 lines mm^{-1} grating combined with the spectrometer and lens as described provided data with a spectral resolution of ~ 0.2 nm.
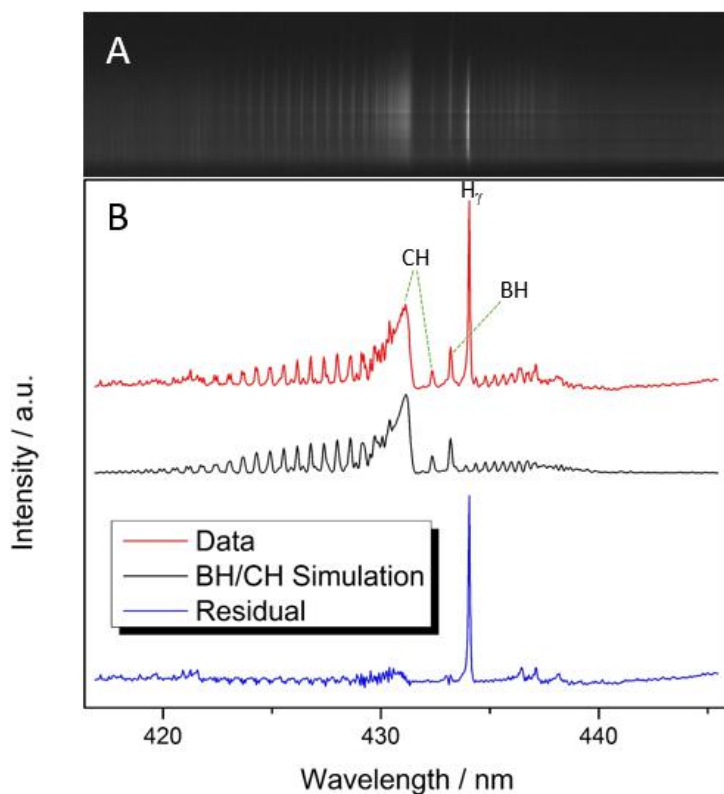
Figure 4.1: An example of BH/CH emission data in (A) its raw, height against wavelength, form where brightness shows intensity and in (B) its PGOPHER-processed form, showing the experimental data (red), the calculated spectrum (black) and the difference between the two (blue). The scale is the same for each trace. In this way the intensity of both species can be extracted from the data and interference from other emissions (e.g. H_γ) can be recognised.

4.2.1 Analysis

Molecular emission spectra were first processed by a MATLAB code to ensure spatial calibration to a reference image, previously acquired using an object of known dimensions in place of the plasma. The code also separated the data by height into 16 bins, each representing a range in the plasma of 1.5 mm (as shown in figure 4.2), introducing a ± 0.75 mm range error to each height result quoted in this chapter. The bin size distance was also confirmed by the spatial calibration images. 16 bins provides a satisfactory balance between signal-noise ratio and spatial resolution.

The molecular emissions were then analysed by the PGOPHER software package. The spectra of N_2/NH and BH/CH were analysed simultaneously to give intensities for both species. The example shown in figure 4.1 also contains the atomic hydrogen Balmer-γ emission line, which, as shown by the residual (data minus simulation) spectrum, is not accounted for in the analysis.

Trends in intensity over the process parameter space were analysed for the maximal intensity bin out of the possible 16 vertically stacked bins. This means the following data for nitrogen species are acquired at a height centred at 6.75 mm above the substrate, and that for BH, CH and CN are acquired centred at 8.25 mm above the substrate. There are
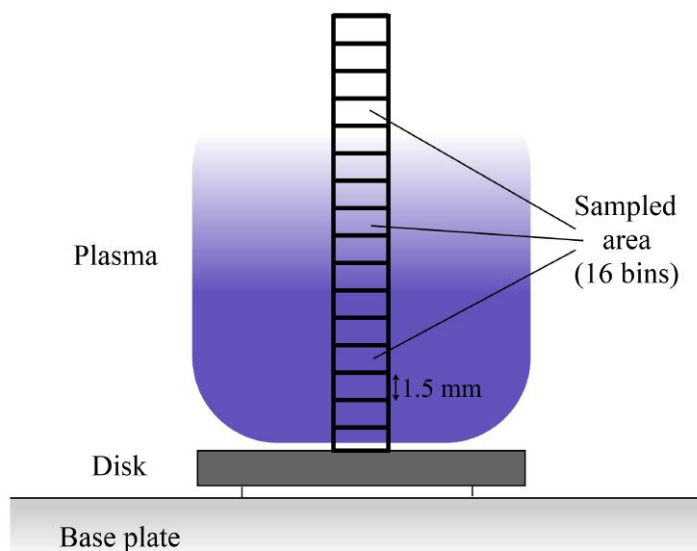
Figure 4.2: Schematic of the plasma overlaid with boxes representing the 16 1.5 mm bins into which data is split after collection.

two artefacts that exist on all raw data, which can be seen in figure 4.1A as horizontal lines across the CCD image. This is likely due to one of the internal components in the spectrometer - such as the slit - and is considered inconsequential for the subsequent analysis. Height resolved data, however, requires consideration of this issue.

The emission of atomic boron was analysed by a MATLAB code that simply integrates the area under the spectral peak minus a linear baseline. This method allows continuous, not binned, height resolved data to be acquired.

4.3 Results and discussion

Due to the complexity of this 4-gas system, the results for plasmas containing two gases are interpreted with reference to previous literature, before examination of the results of the three and four gas mixtures.

4.3.1 N/H and B/H plasmas

Nitrogen and boron have individually been added to hydrogen microwave plasmas and their emissions characterised before [114, 164–168, 170]. The data presented here therefore acts as a consistency check, with the plots shown in (at least qualitative) agreement with previous work.
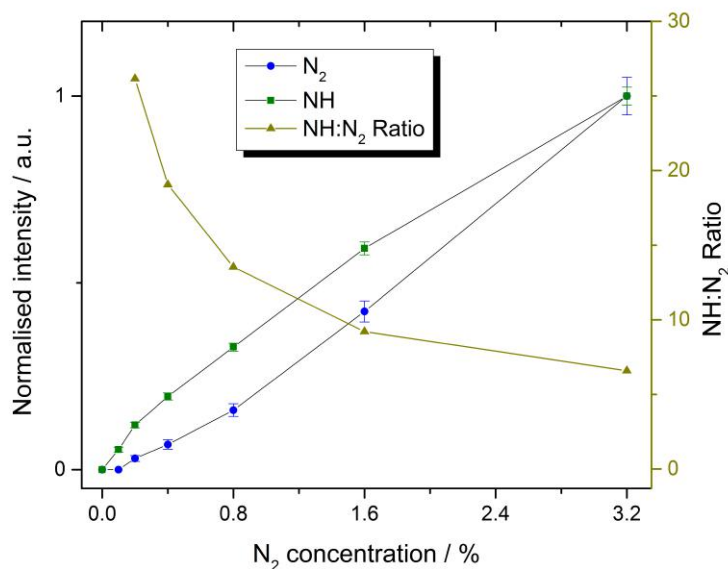
Figure 4.3: Normalised intensity of N_2 and NH emissions as a function of nitrogen concentration in a N/H plasma. The ratio between the two emissions is also shown.

The first experiments on N/H plasmas were carried out in the reactor before diborane gas had been introduced. This ensured the very minimum of contaminating species could interact with reactive NH_x radicals. Figure 4.3 shows the increase of N_2 and NH emissions upon increasing nitrogen concentration in the feed gas from 0 to 3.2 %. Both species have roughly linear trends, but NH intensity is dominant at low [N_2], a trend which is also apparent in their emission intensity ratio. This is in agreement with previous results from the same reactor [168] and could be due to the initial [N_2]/[H] fraction being small. Reactions producing NH, for example $N_2^{(*)}$ + H$\longrightarrow$NH + N (where $N_2^{(*)}$ is an excited nitrogen molecule), will proceed more rapidly at low N_2 content since there is an abundance of H atoms in the hot plasma region.

The intensity as a function of height above the substrate, or spatial profile, for NH and N_2 emissions at 3.2 % N_2 input is shown in figure 4.4. The previously mentioned artefacts in the raw data are also apparent in the analysed data shown here, manifesting mainly in a slight local intensity minimum around a height of 9-11 mm. The heights at which N_2 and NH emissions peak, 3 mm and 6-7.5 mm respectively, are slightly below those found in previous results using the same reactor [168], 6 mm and 9 mm. The difference in peak heights is the same here and, with the influence of the artefacts, this result is considered consistent with the earlier work. If one took the entire shape of the emission of NH and N_2 in figure 4.4, their central positions would agree fairly well with the previous report. Moreover, previously a 30 mm disk was used where here the
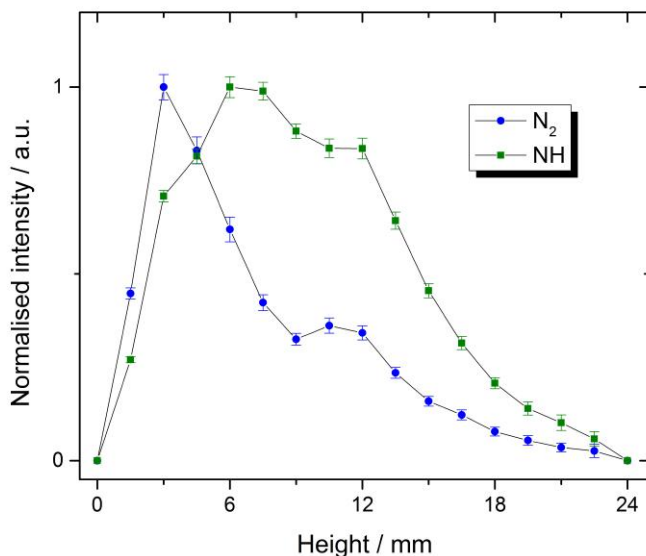
Figure 4.4: Normalised intensity of N_2 and NH emissions as a function of height above the substrate in a N/H plasma with 3.2 % N_2 present.

diameter is 1.25 ". This wider disk tends to expand the plasma in the radial direction and if power density changes are minimised by contracting the plasma vertically, then the disk may account for some of this discrepancy.

In previous work, the spatial profile of NH was compared against CRDS absolute column density values and shown to correlate strongly [168]. This means that in this case, emission intensity changes are primarily the result of proportionate changes in the number density of each species.

For N_2, the low peak height is the result of gas density, where (considering the ideal gas law, $PV = nRT$) the density is highest in the cooler (nearer to the substrate heat sink) region than in the middle of the plasma [69, 171]. The electron number density must still be high enough to cause substantial excitation, however, so N_2 emission drops off at large heights where the plasma ceases to produce sufficient electrons.

NH on the other hand is less abundant in the cooler regions. This is due to the necessary H-shifting processes that form NH_x species from nitrogen being less frequent as H atoms are mostly thermally produced in the hot plasma region.

The result of increasing diborane concentration in a previously hydrogen containing plasma is shown in figure 4.5, with BH and B atom emission intensities detected. Unfortunately no data were gathered for concentrations of (e.g.) 7.5 ppm where the emission of both species is likely to be low but measurable, however like previous work [165] (where BH was detected) the intensity is found to be proportional to diborane
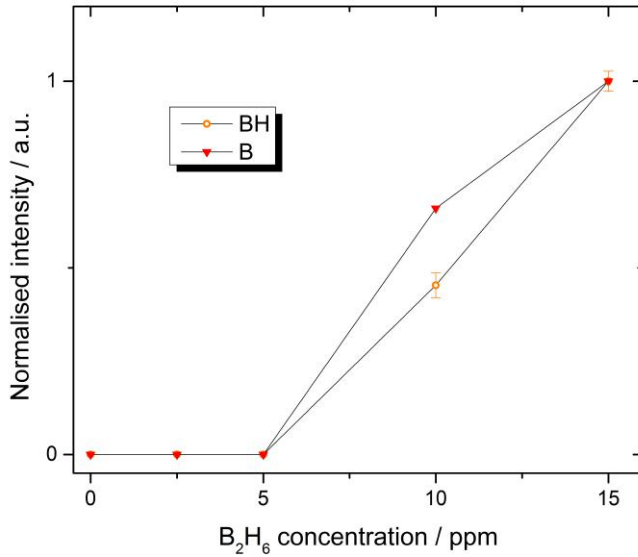
Figure 4.5: Normalised intensity of BH and B emissions as a function of B_2H_6 concentration in a B/H plasma.

increase after an offset due to contaminating oxygen. The O contamination arises due to a combination of vacuum vessel-adsorbed water, chamber leaks and gas impurities (which are minimised). The previous researchers attribute the loss of boron containing species to the production of BO_x solids.

B and BH are two of the abundant BH_x species predicted [165], so provide a good marker for the presence of boron in the plasma. Their concentration is dependent on gas temperature just as with NH. BH radicals are more prominent in the higher temperature part of the plasma, as is shown by previous calculated spatial distributions [165] and confirmed in the data shown in figure 4.6. [B] is predicted to peak at large height values, but as shown the emission peaks at low height. Total gas number density combined with gas temperature being lower, which favours B over BH in some conditions [166] close to the substrate, could account for this. Additionally, B emission hasn't been examined with this experimental apparatus before so there is no reason to cast doubt on the validity of the results.

4.3.2 B/N/H plasmas

Having confirmed that N/H and B/H plasmas act as expected under the conditions examined here, B/N/H gas mixtures are now explored. This constitutes the first data for which there is no direct literature comparison, however many of the trends are consistent with previous work.
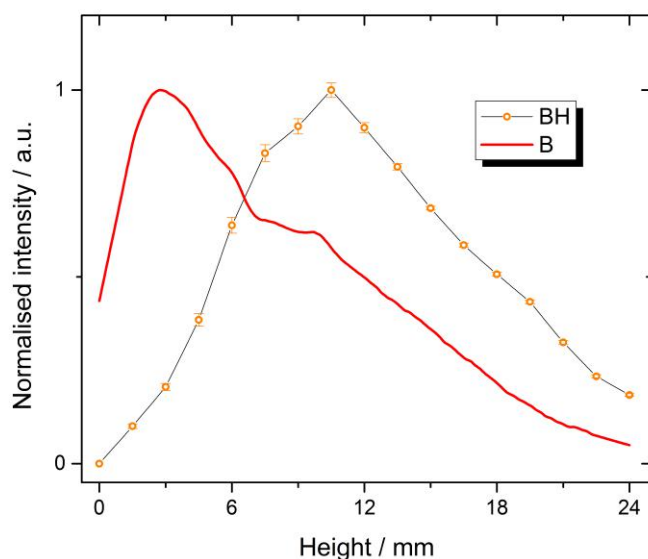
Figure 4.6: Normalised intensity of BH and B emissions as a function of height above the substrate in a B/H plasma with 15 ppm B_2H_6 present.

Figure 4.7 shows the effect of introducing N_2 gas to a preexisting B/H plasma. Firstly, it is clear that the presence of 15 ppm of diborane in the input gas makes no qualitative difference to the behaviour of N_2 and NH emissions. The introduction of such small quantities of B_2H_6 to a hydrogen plasma induces insignificant changes in the plasma characteristics [165] so changes in nitrogen species intensities are not expected, especially considering 3.2 % N_2 is equal to 32,000 ppm. Even considering the low dissociation fraction of N_2 [168], NH_x concentrations are predicted to be comparable to, but slightly exceed, those of BH_x [165] at these conditions.

The marked decrease in B and BH emissions upon nitrogen increase shown in figure 4.7 does suggest a strong role of nitrogen in the concentration of detectable boron species in the plasma. Since N_2 is so inert this likely arises due to reactions with NH_x species. Owing to the lack of change in NH behaviour with diborane present, this indicates that either a species with $x \neq 1$ is involved, or if NH is reacting with B and BH then its nitrogen reservoir, N_2, is vast enough that any reactions make little difference to its abundance, being replenished as quickly as it is depleted. B and BH have no such large reservoir when 15 ppm of diborane is used.

The B atom emission intensity at 0.4 % N_2 in figure 4.7 exceeds expectation, considering the rest of the trend. The reason for this is unknown, but is not a consequence of poor data analysis - that is the measured intensity at this set of conditions is in fact high. From the emissions of B and BH at $[N_2]$ = 0.1 and 0.2 %, it is clear that BH emission is
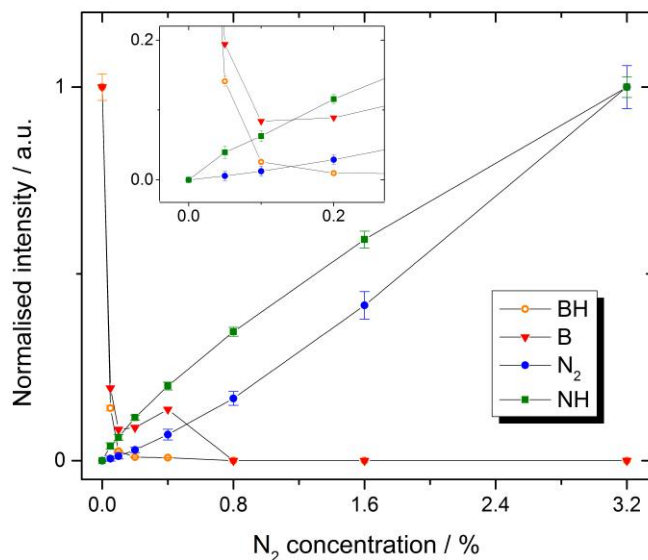
Figure 4.7: Normalised intensity of gaseous emissions as a function of nitrogen concentration in a B/N/H plasma with 15 ppm B_2H_6 present. The inset shows an expanded view of low intensity and N_2 concentration.

suppressed more readily than B emission, the reason for which is also unknown. Repeat measurements may highlight the cause of this unexpected result.

Spatial profiles of each species under changes in nitrogen flow were qualitatively consistent with those of figures 4.4 and 4.6, despite the large reduction in boron containing species intensity as shown in figure 4.7.

Due to this vast drop in B and BH emission in the presence of nitrogen, it was not possible to monitor the effect of diborane on N_2 and NH emissions whilst also detecting boron containing species in a B/N/H plasma. The results of increasing B_2H_6 concentration in a preexisting N/H plasma are shown in figure 4.8, with B and BH emissions detected. With the addition of more data points, the plot is similar to that of figure 4.5, where the intensities are essentially linear after an offset that is likely caused by contamination and in this case by the presence of nitrogen. At 0.1 % N_2, which is 1000 ppm, the NH_x concentrations in the plasma are likely to be comparable to those of BH_x [165, 168], but any linear offset caused is not discernible from the precision of the data shown here.

The spatial profiles of B and BH at 15 ppm diborane added and in the presence of 0.1 % N_2 were qualitatively consistent with those of figure 4.6.

In order to interpret the B/N/H plasma data, an analogy to hydrocarbon chemistry can be made. The dominant form of carbon found in the hot region of a C/H plasma is C_2H_2, with its number density up to two orders of magnitude higher than any other C_xH_y species [110]. The remaining carbon is predominantly made up of CH_4, CH_3 and
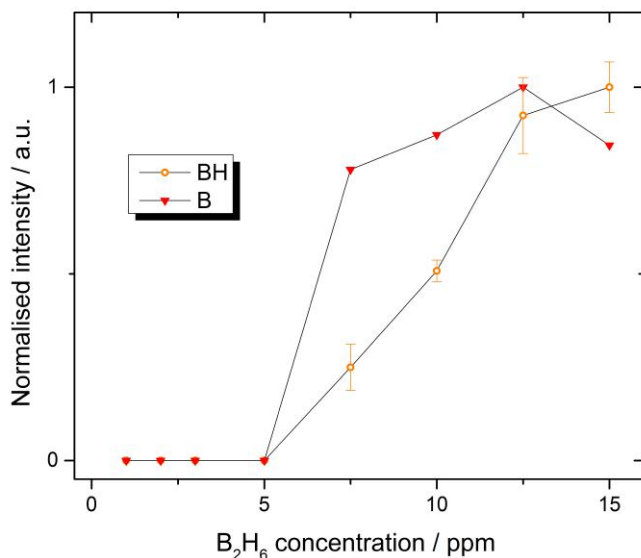
Figure 4.8: Normalised intensity of BH and B emissions as a function of B_2H_6 concentration in a B/N/H plasma with 0.1 % N_2 present.

Table 4.2: Enthalpies of formation of a range of gas phase species in the CVD plasma. X is either N, B, C, C_2 or BN. All but BN are from the NIST database, reference [1]. The data for BNH and BNH_2 are not available on NIST, so calculated values [2] are given for the BN series instead. ΔH_F for H is 218.00 kJ mol^{-1}

	ΔH_F for $X = ...$ / kJ mol^{-1}				
	N	B	C	C_2	BN (calculated)
X	472.68	560.00	716.67	837.74	610.864
XH	376.56	442.67	594.13	476.98	300.83 (BNH), 383.67 (HBN)
XH$_2$	190.37	200.83	386.39	226.73	48.95

C_2H, and this is the case regardless of the carbon containing precursor gas. A similar thing could well happen for boron-nitrogen chemistry and to illustrate this a range of enthalpies of formation, ΔH_F, for species of interest are presented in table 4.2.

The ΔH_F values on their own do little to help understand the interaction of boron and nitrogen, however their combination can justify qualitative predictions through comparison of reaction enthalpies to those of previously modelled reactions. Shown in table 4.3 are the reaction enthalpies, ΔH_R, for a range of reactions producing BNH_x species alongside the equivalent (isoelectronic) C_2H_x reactions. The reaction pathways that produce the abundance of C_2H_2 do in fact involve higher numbers of hydrogen atoms [172], but here $x \leq 2$ is sufficient for illustrative purposes.

Most of the ΔH_R values are more negative for the carbon containing species, implying that production of BNH_2 may not be as dominant in a B/N/H plasma as C_2H_2 production

Table 4.3: A number of illustrative reactions that form BNH_x species. For comparison, reactions forming C_2H_x. Only $x \leq 2$ is considered for simplicity despite the fact predominant C_2H_x chemistry occurs via $x > 2$. As it is more stable, ΔH_F for BNH is used rather than for HBN in reaction enthalpy calculations.

N^o	BNH_x Reaction	$\Delta H_{R,BNH_x}$ / kJ mol^{-1}	C_2H_x Reaction	$\Delta H_{R,C_2H_x}$ / kJ mol^{-1}
1	BH + N $\longrightarrow$ BN + H	-86.49	CH + C $\longrightarrow$ C$_2$ + H	-255.06
2	NH + B $\longrightarrow$ BN + H	-107.70	CH + C $\longrightarrow$ C$_2$ + H	-255.06
3	BN + H$_2$ $\longrightarrow$ BNH + H	-92.03	C$_2$ + H$_2$ $\longrightarrow$ C$_2$H + H	-142.76
4	B + NH $\longrightarrow$ BNH	-635.73	C + CH $\longrightarrow$ C$_2$H	-833.82
5	BH + NH $\longrightarrow$ HBNH	-770.28	2CH $\longrightarrow$ C$_2$H$_2$	-961.53
6	BNH + H$_2$ $\longrightarrow$ HBNH + H	-33.88	C$_2$H + H$_2$ $\longrightarrow$ C$_2$H$_2$ + H	-32.25

is in a C/H plasma. However, reaction 6 has a similar exothermicity for both carbon and boron-nitrogen chemistry. This suggests that the B-H and N-H bonds in HBNH are approximately as strong as the C-H bond is in C_2H_2, which in turn suggests that HBNH could be a prominent species in a B/N/H plasma. A full treatment using a kinetic model such as the Bristol-Moscow model would be needed to fully elucidate this.

4.3.3   B/N/C/H plasmas

Emission intensities during the gradual addition of methane to a preexisting B/N/H plasma, from 0 to 4 % CH$_4$, are shown in figure 4.9. The initial conditions are the same as those resulting in the 0.4 % N$_2$ points of figure 4.7, where some intensity can be detected for all studied emissions, resulting in large measurable changes in all examined species.

The detected carbon-containing species, CH, is known to increase with a square-root dependence on the methane concentration [158], a trend which is well reproduced here. The presence of 15 ppm B$_2$H$_6$ and 0.4 % N$_2$ does not appear to affect the plasma significantly enough to cause the CH emission to be qualitatively altered.

Nitrogen species emissions also have a similar appearance to that reported for this reactor chamber before [114], with the N$_2$ intensity rising slightly and the NH intensity dropping before converging on a low value. NH emission is lowered because of a large drop in the number density of NH and in fact NH$_x$ species as a whole. The reactive nitrogen containing radicals are overwhelmingly converted into HCN, which in previous calculations is shown to contain > 99 % of all non-N$_2$ nitrogen in the hot part of a N/C/H plasma. The rising N$_2$ emission could be the result of either slight increases in N$_2$ number density [114, 168] at these conditions; gas temperature, which increases

Figure 4.9: Normalised intensity of gaseous emissions as a function of methane concentration in a B/N/C/H plasma with 0.4 % N_2 and 15 ppm B_2H_6 present. For clarity the plot is split arbitrarily into two. The high N_2 emission errors are due to low signal:noise, but the data points do correspond to a measured trend in intensity.

upon introduction of methane (see figure 4.10 and associated discussion); or because of increased number of electrons owing to a change in the average ionisation energy of the plasma gas.

In figure 4.9, B and BH emissions increase and appear to level off above 2 % methane in the feed gas. This is in stark contrast to the work of Ma. et al [166], in which the BH emission (and B and BH column densities in CRDS) spikes at ~ 0.5 % CH_4 in hydrogen, before returning to a low value and gradually declining with further methane increases. On the other hand, Rond et al. [167], who performed similar experiments, report no such spike in BH emission or either B or BH densities, in fact presenting a decline in the B mole fraction with increasing methane.

To explain the results of B and BH, and those of Ma et al. and Rond et al., the effect of the main active impurities before and during methane introduction is considered. Here the majority non-hydrogen gas is nitrogen since, as mentioned, measures were taken to reduce both leak and gas impurities to below 1 ppm. As discussed in section

4.3.2, NH_x species will likely undergo reactions with BH_x species to form (e.g.) BNH_x. Upon methane introduction the conversion of NH_x radical population to HCN [114] will reduce the number densities of NH_x species and thus their interactions with BH_x species, increasing the BH_x population.

Ma et al. hypothesise that oxygen in the air leak, gas impurity and adsorbed water impurities interacts with boron species and its reduction results in the spike they find in boron population when CH_4 is added [166]. The reactions and new species are modelled and the trend is well reproduced by the calculations, confirming the culprit. They model species such as HBO and H_3COBH_2, as well as CO, which is the main product of reactions of oxygen containing species with CH_x. CO production results in reactive oxygen-containing species being less pervasive in the plasma and therefore possibly not interacting as strongly with BH_x. A small amount of added methane *getters* the oxygen, causing an increase in BH_x population. Once little oxygen remains at higher CH_4 content, species like $CH_xCH_yBH_2$ begin to form, again reducing $[BH_x]$ and thus lowering B and BH populations and their emissions.

The reduction in B atom density found by Rond et al. [167] could be a result of extremely low interaction of BH_x with impurities. If nitrogen and oxygen were present at below significant levels, then the predominant result of CH_4 additions would be the production of HCB-containing species such as CH_2CHBH_2 [166]. Without N or O, these hydrocarbon-borane species are the majority sink for boron in the hot plasma and with more CH_x and C_2H_x their production rate will be increased.

This set of three scenarios with distinct trends of boron species emission with increasing methane fraction and their interpretation with respect to impurities like N and O highlights the strong influence of gas composition on the population of BH_x.

The gas temperature as measured by BH emission is shown in figure 4.10, for a B/N/H plasma with and without methane addition. The data have larger errors at the peripheries of the plasma due mainly to signal:noise. It is possible that the limited wavelength range used to analyse the spectrum, combined with low intensities due to the presence of nitrogen, causes BH not to be a reliable thermometer for B/N/C/H plasmas. That said, the gas temperature increase on addition of CH_4 does qualitatively reproduce that of previous research [166], where a 300 K rise was measured from 0 to 5 % methane.

Figure 4.11 shows the trend of each species as N_2 is progressively introduced to the reactor. The nitrogen increase has little to no effect on CH emission (note CH is collected and analysed together with BH). This implies minimal effect on plasma characteristics such as number and effective temperature of electrons present. The qualitative behaviour
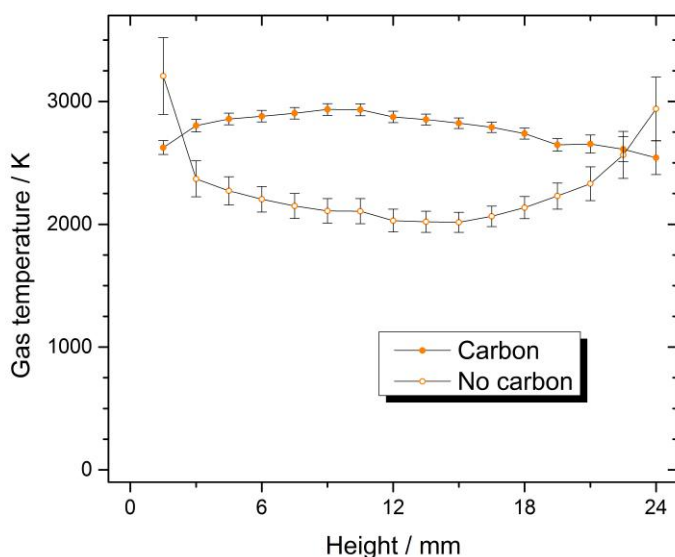
Figure 4.10: Gas temperature as estimated from BH (and CH) emission spectra from a B/N/H plasma and a B/N/C/H plasma with 2 % methane. Gas temperatures estimated from peripheral emissions are considered unreliable as errors are large.

of NH and N_2 emissions is much the same as without CH_4, whilst being undetectable at low nitrogen input concentrations. This reflects the decrease in NH_x concentration caused by HCN formation.

The BH_x emitters, on the other hand, behave differently to the no-carbon case. Whilst in figure 4.7 their emissions were quenched rapidly and completely by 0.4 - 0.8 % nitrogen added, here in figure 4.11 they remain emitting up to the maximal 3.2 % N_2. This is a confirmation of the previous claim that the presence of CH_4 causes the reactive nitrogen species in the plasma to react more prominently with carbon to form species like HCN than with BH_x to form BNH_x. The B and BH emission intensities do still reduce on increase of nitrogen flow, implying that despite the effect of carbon on nitrogen, some reactions such as those in table 4.3 may still occur.

The effect of increasing diborane concentration in the feed gas to a preexisting N/C/H plasma is shown in figure 4.12. The data agree well with that of Ma et al. [166], where BH emission was also linear when methane was present in the plasma. This is contrary to the situation without carbon found here and by Ma et al. [165], where impurities delay the onset of linear behaviour (figure 4.8), this time attributable to nitrogen instead of oxygen. Again, this is consistent with claims that carbon in the plasma causes impurities such as NH_x to be reduced. This is strong evidence that NH_x species interact with BH_x species in the hot plasma region, likely via some of the reactions shown in table 4.3 and more.
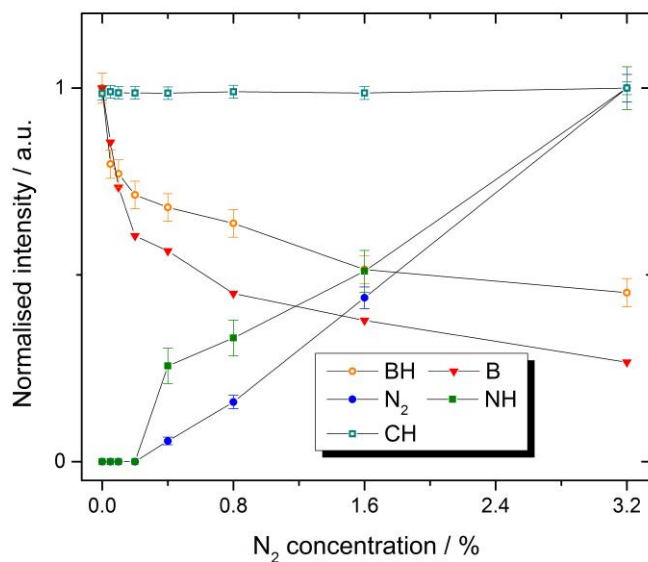
Figure 4.11: Normalised intensity of gaseous emissions as a function of nitrogen concentration in a B/N/C/H plasma with 15 ppm B_2H_6 and 2 % CH_4 present.
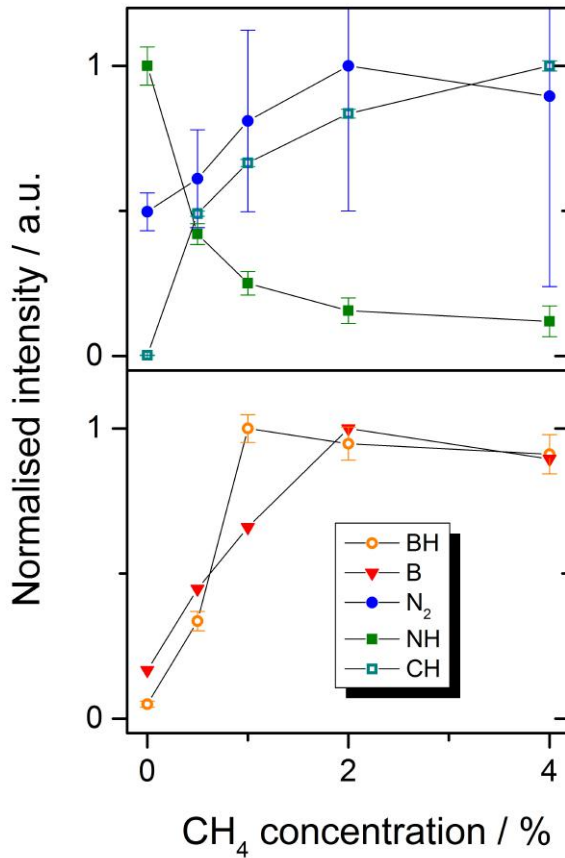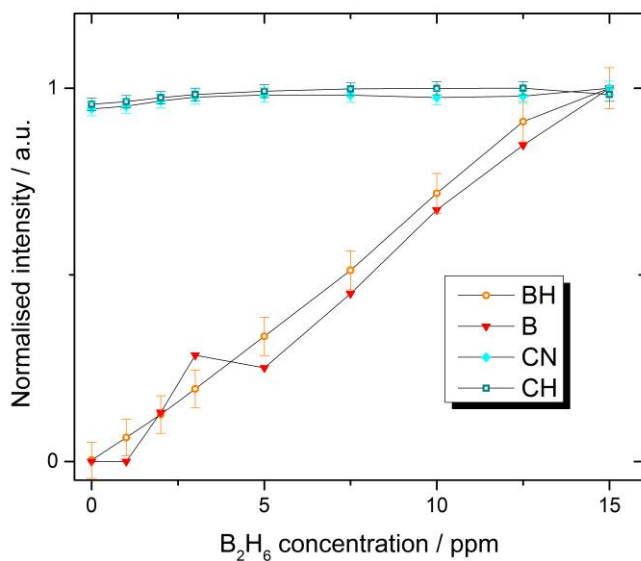

Figure 4.12: Normalised intensity of gaseous emissions as a function of B_2H_6 concentration in a B/N/C/H plasma with 0.4 % N_2 and 2 % CH_4 present. NH and N_2 emissions (not shown) were low and had large associated errors due to signal:noise.

The emission intensities of N_2 and NH were measured during the increase of diborane in the B/N/C/H plasma, however their values were small with large errors. No discernible changes occur over the 0 - 15 ppm parameter space measured here.

The work of Sartori et al. [83, 84] showed that BH_x and NH_X species must interact in some way, even in methane containing plasmas, since boron was able to mitigate the growth-rate enhancing effect of small nitrogen additions to the CVD plasma. However, their optical emission studies provided no evidence for that claim, suggesting to the authors that the boron-nitrogen interaction could be non-plasma-related (a diamond surface effect perhaps). The results presented here clearly show that BH_x and NH_x must interact in the plasma in some way, but the nature of their chemistry is unclear. That diborane addition doesn't significantly affect NH_x (or CN) emission intensity in the data shown here does not disprove this hypothesis. Again, the reservoir of nitrogen in N_2 might be responsible for this, the parameter space may merely be too narrow or possibly the species sensitive to changes in BH_x was not examined. One candidate is N atoms which are calculated to be the most abundant NH_x species close to the substrate in a N/C/H plasma [114]. N emits at $\sim$ 120 nm [173], so would require a well thought-out experiment. UV-transmissive components and possibly vacuum both in the reactor-spectrometer gap and in the spectrometer itself would allow detection of significant emission intensity.

CRDS experiments on absolute densities of NH_x species at the concentrations they are able to quench BH_x emissions would lead to a greater understanding of their interaction in a hot B/N/H plasma. In addition, any reduction in NH density caused by the presence of boron would similarly elucidate the chemical interactions. A similar argument can be made for B/N/C/H plasmas, where absolute density measurements would be key, but a combination of these with modelling results would be necessary to explain this complex 4-part system.

4.4   Conclusion

4.4.1   Summary

In summary, this chapter focuses on measurements of the optical emission intensities of gaseous species in B/N/H and B/N/C/H plasmas with respect to changes in the concentration of each non-H_2 process gas.

As processed by MATLAB codes and PGOPHER, the data show that many of the trends

are consistent with previous reports, beginning with N/H and B/H plasmas. Specifically, the emissions of NH, N_2, B and BH are all linear with the latter two first overcoming an impurity induced offset. By reference to the literature, these linear trends can be interpreted as signifying linear increases in the population of each species in the plasma.

The emissions of NH, N_2, B and BH in a B/N/H plasma showed similar behaviour as in N/H and B/H plasmas, apart from a strong interaction of nitrogen with BH_x causing a full quenching of their emissions at and above 0.8 % N_2. The reaction of NH_x with BH_x is hypothesised to result in BNH_x species via reactions analogous to those resulting in the dominant C_2H_2 molecule. The NH intensity is not diminished by B_2H_6 introduction, which is thought to be due to the large nitrogen reservoir in N_2 restoring the equilibrium NH_x concentration upon its reaction with boron containing species.

The addition of methane to the B/N/H plasma causes a number of emission intensities to change in similar ways to those reported previously. For example the emission of CH increases with a square-root dependence on the CH_4 concentration, N_2 increases slightly, and NH reduces due to HCN formation. Whereas B and BH follow trends dissimilar to the two previous reports of Ma et al. [166] and Rond et al. [167], which also dispute each other. These differences are interpreted in terms of nitrogen and oxygen species or lack thereof. Additions of N_2 to B/C/H plasmas and of B_2H_6 to N/C/H plasmas cause trends that confirm that (e.g.) HCN formation mitigates the interactions of nitrogen with boron species previously hypothesised to occur in B/N/H plasmas, but does not entirely stop them.

4.4.2 Future work

In order to progress this project, expansion of the parameter space to lower nitrogen concentrations (requiring mixed N_2 in hydrogen gas to be introduced to the reactor) would allow further analysis of BH_x quenching in B/N/H plasmas. Higher flow rates of B_2H_6 would similarly allow more detailed experiments in B/N/H plasmas; for example, is the key parameter the ratio [boron]:[nitrogen] in the feed gas or do their absolute values make a difference to their emission trends? Continuation of this experiment on the new spectroscopic apparatus in the Bristol diamond lab would aid in this effort, since the signal:noise ratio, spectral resolution and UV sensitivity are greatly enhanced with respect to those possible in this work. This may mean minute changes in (e.g.) NH emissions could be differentiated, and specifically the effect of diborane introduction on the NH emission in a N/H plasma could be analysed. Along with possible N atom detection, this could elucidate the cause of the growth rate annihilation caused by small

boron additions to the N/C/H plasmas of Sartori et al. [83, 84] and of those in chapter 5 of this thesis. A full understanding of the interactions of nitrogen and boron species in B/N/C/H plasmas requires both experimental effort and modelling in a manner similar to that carried out in the work of Ma et al. [165, 166] and Truscott et al. [114, 168].

GROWTH AND CHARACTERISATION OF B-N CO-DOPED DIAMOND FILMS

5.1 Introduction

Interpretation of the results of gas-based deposition may be complicated, since changes in process parameters may cause either: altered plasma chemistry, morphological changes in the material, or differing incorporation efficiency of dopants. These issues are particularly problematic for boron and nitrogen in diamond since not only do boron and nitrogen interact strongly in the gas phase (see chapter 4), but their combination may also produce stable compounds with similar characteristics to carbon materials, such as boron nitride [174].

Understanding gas phase chemistry does provide insight into the reasons for eventual material changes, but there are also various notable existing studies tackling some aspects of this complex problem. As discussed in chapter 4 the addition of boron to a nitrogen-containing growth plasma can entirely mitigate the N_2-induced rate enhancement [83, 84]. This effect has been observed not only in plasma-based deposition, but also when using hot filament (HF) activation [116]. Changes in morphology are reported and graphitic phases appear to coexist with the produced diamond material. With the large input dopant concentrations required in the microwave plasma (MP) growth of boron doped nanocrystalline diamond, changes in nitrogen flow during morphological optimisation can result in reduced estimates of dopant incorporation [163].

Some distinction can be made between the effects of plasma chemistry and incorporated dopant interactions by direct concentration measurement of incorporated impurities, for example by SIMS. Even HFCVD incorporation efficiency of boron can be greatly reduced by the presence of N_2, not usually considered a good nitrogen precursor in hot filament systems due to its strong triple bond [80]. The co-introduction of the two dopants does produce a promising widening of the window over which diamond electrochemical electrodes do not cause solvent reactions [79, 80], but advantages of the B-N combination are rare.

Most changes in the material electronic properties due to nitrogen introduction are a hindrance to applications, with nitrogen compensating boron acceptors [72] and even those present in intrinsic material [33]. For most growers, a reduction in their gas impurity levels could likely result in improved electrical characteristics of boron-doped diamond due to lack of nitrogen within the material [71]. Conductivity can be reduced in boron doped diamond by five times whilst increasing nitrogen in the gas phase from, for example, 0 to 500 ppm [70].

Many of the cited studies provide a strong argument for the disadvantages of small quantities of nitrogen when it comes to growing, doping or applicating boron-doped diamond. By contrast, here the relative input concentrations of boron and nitrogen are qualitatively reversed, studying the effect of large nitrogen additions and small quantities of boron in the growth plasma. A range of techniques are used to study different aspects of the material, broadly fitting into the categories of growth, incorporation and electrical characteristics.

Details of experimental procedures are given, before describing the set of samples required to explore each aspect of the analysis. Results are presented for each technique and discussed in the context of changes in dopants and the type of diamond: polycrystalline or single crystal material. Some material characteristics such as morphology and dopant concentrations have an influence on others such as electrical properties; the discussion attempts where possible to elucidate these trends.

5.2 Experimental methods

Sample preparation firstly consists of substrate seeding (for Si), followed by MP-CVD growth in the reactor described in section 2.2.3, before examination of the grown material using the various analysis techniques, largely in the order they're given in section 2.4.

5.2.1   Substrate seeding

Seeding was required on non-diamond substrates due to the large enhancement of growth rate provided by a homoepitaxial-like surface. The only such substrate used in this thesis was silicon, specifically p-type owing to its higher work function than its n-type counterpart. This high work function results in minimal electron-induced disruption of the growth plasma.

First, the $10 \times 10 \times 0.5$ mm (100) silicon wafers were cleaned in an ultrasonic cleaning bath while submerged in water (Milli-Q purified), ethanol, acetone and methanol (lab-grade), each for 5 minutes. After drying with a compressed air gun, they were placed in a solution of 25 % carboxyethyl silanetriol di-sodium salt in water (Fluorochem, UK) for at least 10 minutes. The silicon was then thoroughly rinsed in Milli-Q water and dried before being submerged in a nominally 18 nm particle size nanodiamond suspension (25 cts L^{-1}; Microdiamant AG, Switzerland) for 5 minutes. They were then dried again and stored for later use. The seeding layer showed no sign of deterioration over normal storage timescales.

5.2.2   Operation of the reactor

Silicon, polycrystalline diamond (0291, Element 6, UK) or single-crystal diamond (0040, Element 6, UK) substrates were placed in the reactor chamber, which was then closed and pumped to a base pressure of $\sim$ 20 mTorr.

During growth, the substrate was heated entirely by the plasma and the temperature was measured by a 1-colour optical pyrometer ($\lambda = 2.2$ μm; Raytech, UK) and displayed on a readout (Thermopoint 8000) in the rack, which was generally compared with a 2-colour pyrometer ($\lambda_1 = 700$ nm, $\lambda_2 = 1000$ nm; Landmark-X V1.14, Land, UK) in order to confirm the emissivity setting. The surface temperatures of the cold and hot silicon, polycrystalline diamond and single crystal diamond were 753 ± 19, 993 ± 15, 727 ± 3 and $978 \pm 9\,°$C respectively.

Each sample grown on a given substrate type was deposited for the same length of time, before the non-hydrogen gases were switched off. The plasma was extinguished only after sufficient time allowed diborane, nitrogen and methane in the process gas to be reduced to minimal levels.

5.2.3   Particulars of materials analysis techniques

Raman spectroscopy. In this work a 325 nm He-Cd UV laser (IK series, Kimmon Koha, Japan) gave Raman shifts detected by a Renishaw 2000 spectrometer (Renishaw, UK). Spectra were recorded for long enough to ensure good signal-to-noise ratio, dependent on the sample. Normalisation to the 1332 cm^{-1} diamond peak height meant differing absolute intensities did not hinder interpretation of the spectra.

Scanning electron microscopy. SEM images were taken by a field emission gun (FEG) SEM facility (Sigma, Zeiss, Germany). 1k, 5k and 15k times magnification images allowed comparison of the morphological changes over the parameter space for each substrate type. To avoid any charging effects the beam energy was optimised prior to taking images, however most samples were gold-coated prior to loading. A sputter coater (Scancoat six, Edwards, UK) deposited ~ 20 nm Au onto the samples, which fully eliminated charging effects.

Secondary ion mass spectrometry. Gallium ions were accelerated up to 25 keV and delivered to the sample at a current of 3 nA. The current was prone to drift, but for sensitive experiments, namely bore time measurements, it was kept within 1 % of this value. Negative mode SIMS was acquired at a 5k times magnification, and positive mode at 1k in order to maximise signal. This meant depth measurements were always performed in negative SIMS mode. Acquisition times differed dependent on the variability of the data, and number of acquisitions per sample also varied as such.

Van der Pauw (VDP). VDP measurements used a 4-way switching box to ensure each orientation of the sample was analysed. A DC/AC source (6221, Keithley, UK) drove the current and a nanovoltmeter (2182A, Keithley, UK) measured the voltage. Both the number of data points and the applied current were tailored to each sample to ensure the highest signal-to-noise ratio and smallest errors. Current ranges were commonly between 10^{-9} and 10^{-4} A and the number of data points was usually between 5 and 20, each taking ~ 0.5 s. For temperature dependent measurements (TVDP) beyond room temperature (RT) a 40 W CO_2 laser (Firestar V series, Synrad, UK) maintained a sample temperature within ± 1 K of the set-point over the range of 300 to 800 °C in steps of 100 °C, measured with a 2-colour optical pyrometer (Spotmeter R160, Land-Ametek, UK). RT measurements, assumed to be at 25 °C, were taken in the same apparatus.

Table 5.1: Nomenclature representing the 5 doping regimes of samples grown for this project. Each uses a given combination of dopants nitrogen and diborane with concentrations given with respect to methane. Examples of full sample notation are given in the main text.

Nitrogen	Boron		
	Zero	Low (10 ppm)	High (50 ppm)
Zero	—	10B	50B
24600 ppm	N	10B.N	50B.N

Thermionic emission. The equipment used for temperature dependent VDP is used again here. A steel collector anode is placed 200 μm from the sample using a motor actuator (Z825V, Thorlabs, Germany), positioned by moving the required distance away from the short position. A 25 V bias is applied to the anode by a DC power supply (HY3003D, Mastech, UK) to ensure that emitted electrons contribute towards the current, measured by a multimeter (2750, Keithley, UK). Molybdenum clamps hold the sample in position and complete the circuit. The sample is rapidly heated from 300 °C to 750 °C over a period of 18.33 seconds.

5.3   Sample set

With the aim of this study to examine the effects of boron and nitrogen on CVD diamond, a set of samples with varying quantities of dopants were produced. Included in this set are controls, with either nitrogen or boron added to the C/H based process gas mixture. Table 5.1 shows the combinations of dopants used, with either 0, 10 or 50 ppm (with respect to methane) diborane and 0 or 24600 ppm nitrogen. Nitrogen incorporates much less readily than boron into the diamond lattice for reasons that will be discussed later, hence its much higher concentration when used.

To study the effects of doping with the concentrations denoted in table 5.1 by a range of techniques, three different substrate types were used. Reasons for this are described in section 2.2.4 and the substrates are shown in table 5.2, along with the techniques they make possible for the samples grown on them.

Combining the doping and substrate nomenclature used in tables 5.1 and 5.2, provides a code used to identify each sample examined in this chapter. Additionally, cold and hot growths on silicon are denoted c-Si and h-Si respectively. This means the substrate

Table 5.2: Showing which sample sets, denoted by their substrates, are used for analysis by each technique. Si, Pc and SC stand for silicon, polycrystalline diamond and single crystal diamond respectively. Examples of full sample notation are given in the main text.

Analysis technique	Sample set substrate		
	Si	Pc	SC
SEM imaging	✓	✓	—
SEM cross-section	✓	—	—
Raman spectroscopy	✓	✓	✓
SIMS	✓	✓	✓
Van der Pauw	—	✓	✓
Thermionic emission	—	✓	—

followed by the doping defines samples individually, such as: "h-Si-10B" for a sample grown on hot silicon with 10 ppm diborane (with respect to methane) added during growth. Another example is "SC-50B.N", in which a single crystal diamond substrate was used and 50 ppm diborane and 24600 ppm nitrogen (wrt. CH_4) were added to the plasma. When it is clearly apparent what the substrate is, some plots and text will use only the doping to differentiate samples.

5.4 Results and discussion

The effects of doping and co-doping manifest in various changes in material and electrical properties, many of which appear to be interrelated. For example the growth rate can be affected by morphology, and electrical characteristics by sp^2 content. This complicates interpretation of the results somewhat. This section attempts to present data and discussion in a logical order, but when necessary to rationalise the findings, draws upon the analysis of multiple techniques.

5.4.1 Growth rate

For samples grown on silicon substrates the thickness was measured by scanning electron microscopy after snapping the substrate and film to expose a clean cross-section of the diamond. Results of these measurements are shown in figure 5.1.
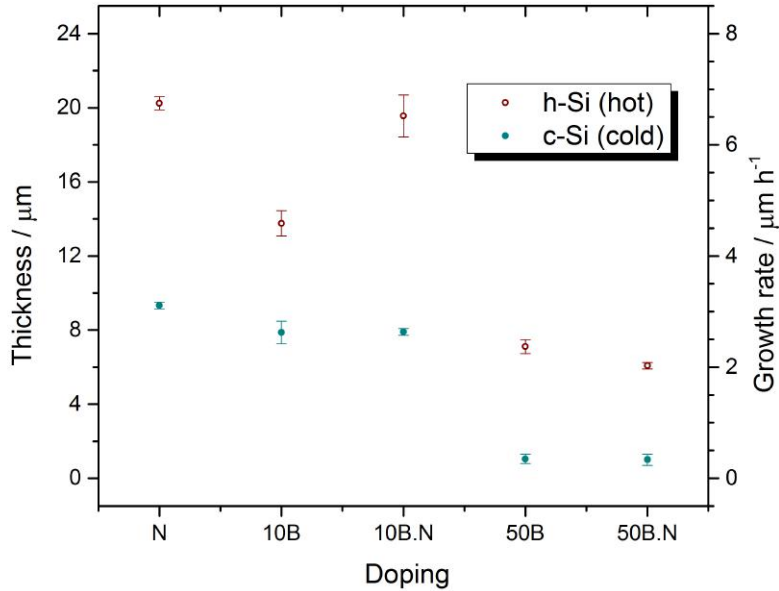
Figure 5.1: Thickness and growth rates (over 3 h) as measured by SEM cross-sections, for samples grown on both hot (h-) and cold (c-) silicon (Si).

Firstly, it is clear that a higher substrate temperature causes faster growth of diamond, a phenomenon known since some the early work on diamond CVD [175].

Boron in general slows the growth rate of the diamond samples shown here, with 50 ppm of diborane reducing the deposition rate of c-Si-50B.N by 89 % compared to c-Si-N. The addition of 10 ppm diborane in c-Si-10B.N, however, reduces the growth rate by only 15 %. This is in agreement with the work of Sartori et al. [83], who claim that the growth rate enhancing effect of 1000 nitrogen atoms in the gas mixture can be suppressed by the addition of 1 boron atom - c.f. 24600 ppm N_2 compared to either 10 ppm or 50 ppm B_2H_6 that, hypothetically, mitigate the effect of 10000 or 50000 ppm of N_2 respectively.

The effect of temperature appears to be most stark when a high concentration of boron suppresses the growth rate, with the growth rate of h-Si-50B 6.1 times higher than that of c-Si-50B. Compare this with h-Si-10B, which grew 1.75 times faster than c-Si-10B.

Unexpectedly, the samples c-Si-N and c-Si-10B have similar growth rates, implying there was either a high background nitrogen content in the MP-CVD reactor or some unknown growth-rate enhancing process occurred during growth of c-Si-10B. The former would be surprising since, as mentioned, the measured leak rate and nominal gas purity are such that less than 1 ppm of impurities can be present during growth. For the equivalent hot-growth samples this issue is less prominent and the data are explicable given the dopants added.
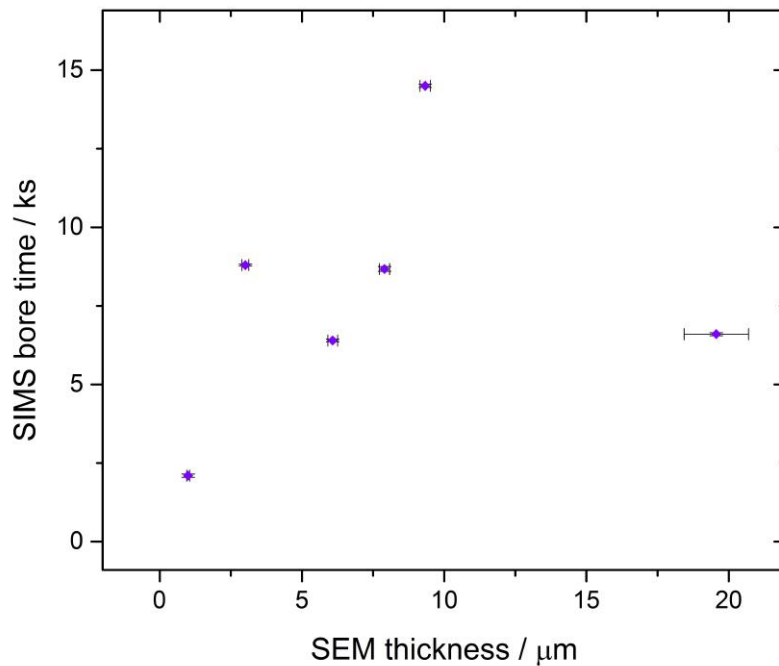
Figure 5.2: A comparison of the time taken to bore through a sample in the SIMS apparatus to the thickness of the sample as measured by SEM cross-section. All samples shown here were grown on silicon.

For samples grown on diamond it is not possible to snap the substrate to expose a cross-section of the grown film. Not only that, but even if it were possible it would be difficult to distinguish sample from substrate. For this reason, SIMS is used to bore through the sample into the substrate. A change in the measured nitrogen concentration is apparent upon reaching the substrate at a time denoted the 'bore time'. Averages of multiple bore times for a given sample often result in low standard errors.

Examples of bore times for a selection of samples of different measured cross-section thicknesses are shown in figure 5.2. Overall, the two thickness measurements correlate fairly weakly, with the thickest sample as measured by SEM being bored fairly quickly by SIMS. This sample does have a large variation in thickness, likely to be caused by a temperature gradient across the substrate during growth, so it is possible the position bored by SIMS was at a thinner-than-average location. Disregarding this outlying sample, the correlation becomes reasonable, confirming that at least a loose estimation of thickness using SIMS is justified.

The etch rate of polycrystalline and single crystal material cannot be assumed equal. Given the lower variation in morpoholog of SC samples, SIMS bore time may in fact be a more consistent measure of thickness on diamond substrates than on silicon. There is no thickness comparison though, so this is purely a speculation. Nevertheless, with the etch rate of single crystal diamond presumed to be a constant, as measured by Dr. Peter
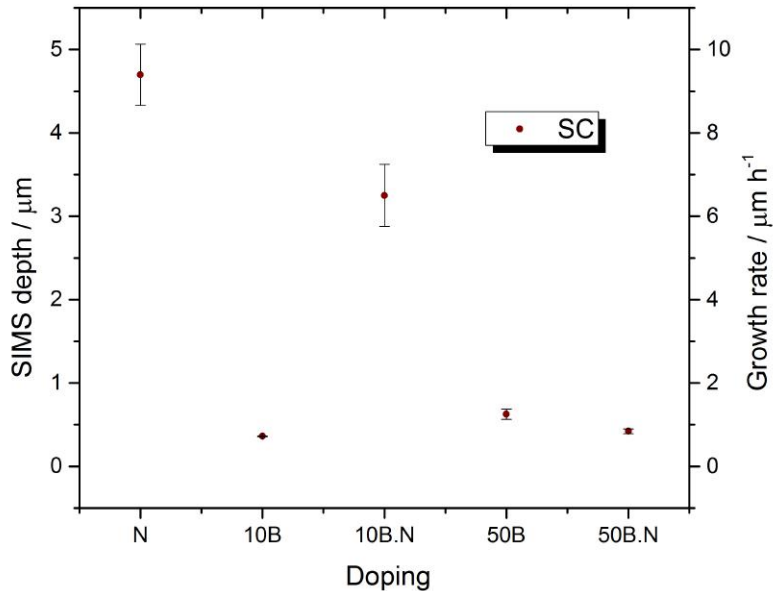
Figure 5.3: Thickness and growth rates (over 0.5 h) as measured by SIMS bore time for samples grown on single crystal (SC) diamond.

Heard (who is gratefully acknowledged), the depth can be estimated.

The SIMS depth for the SC sample set is shown in figure 5.3. The trends largely reproduce those found in the silicon substrate sample set (figure 5.1), with some subtle differences. The growth rates are in general higher, consistent with the lack of grain competition in single crystal growth making deposition more rapid.

It is clear that boron suppresses the growth rate significantly at a concentration of 50 ppm, and slightly at 10 ppm even with nitrogen present, which is similar to the effect in Si-based samples. By contrast, when N_2 is not added to SC growth, a small addition of 10 ppm diborane results in a deposition rate as low as with a large boron concentration. Reasons for this could be gas-phase impurity related if for some reason less nitrogen was present in SC-10B than in h-Si-10B (which had a similar growth temperature to SC). However, the leak rate was low, confirmed prior to every growth of diamond in this project. This suggests that when growing single crystal, compared to polycrystalline, a lower concentration of boron is required to suppress the rate enhancement of nitrogen. There is debate in the literature about the incorporation of dopants in grain boundaries, with nitrogen thought to preferentially insert more readily into grain boundaries than bulk in nanocrystalline diamond [176] and little evidence regarding whether boron does the same. Both dopants will incorporate into (111) growth facets roughly 10 times more efficiently than into (100) facets, with boron about 100 times more efficiently than nitrogen in either case [177, 178]. Given that the SC sample set is (100) orientated,

perhaps the incorporation of nitrogen on the growing surface is so low that boron is
better able to counteract its effect than it is in polycrystalline (Si based) samples where
a greater variation of morphological features is available.

5.4.2 Surface morphology

Alongside measurements of cross-sectional thickness, scanning electron microscopy can
provide comparitive characterisation of grain sizes and morphology, as well as further
information such as the occurrence of twinning.

In addition to changing growth rate, dopants are known to alter the morphology of
diamond films. A distinction can be made between *orientational* and *textural* morphology,
the former signifying which, if any, is the dominant crystallographic direction pointing
normal to the film surface and the latter providing information on which, if any, is the
prominent facet terminating the crystallites. After a long enough growth time the fastest
growing direction is thought to prevail and dominate the orientation of the film [179].
In undoped films this will commonly be the (110) direction, but this may be difficult to
ascertain since the texture of these films is almost always (100)- or (111)-dominated due
to the high (110) growth rate. Temperature is also a key factor in both orientation and
texture.

SEM images for the c-Si and h-Si sample sets are shown in figure 5.4. From previous
studies [115], nitrogen introduction is known to cause the (100) direction to dominate
the orientation as well as the texture. In the N-doped samples grown here though,
temperature appears to determine the efficacy of nitrogen in dictating orientational and
textural morphology as well as grain size. c-Si-N shows a predominantly (111) orientation
combined with a (111) texture whilst h-Si-N has (100) orientation and (111) texture,
implying that cooler growth mitigates the effect of nitrogen on the (100) orientation
enhancement. Even so, the fact that (100) facets are not prominent in c-Si-N implies
the (100) growth rate is faster than the other directions, so temperature affects the
orientation considerably but possibly has a lesser contribution to relative facet growth
rates.

The smallest grain size of the c-Si set are those grown in the presence of 50 ppm
diborane; both with similarly random facetting and orientation, but a slight increase
in grain size in the nitrogen-added case, c-Si-50B.N. With only 10 ppm of diborane the
films adhere to a more well-defined morphology, with c-Si-10B having a mixed (100) and
(110) orientated appearance and c-Si-10B.N growing with mainly (100) orientation. The
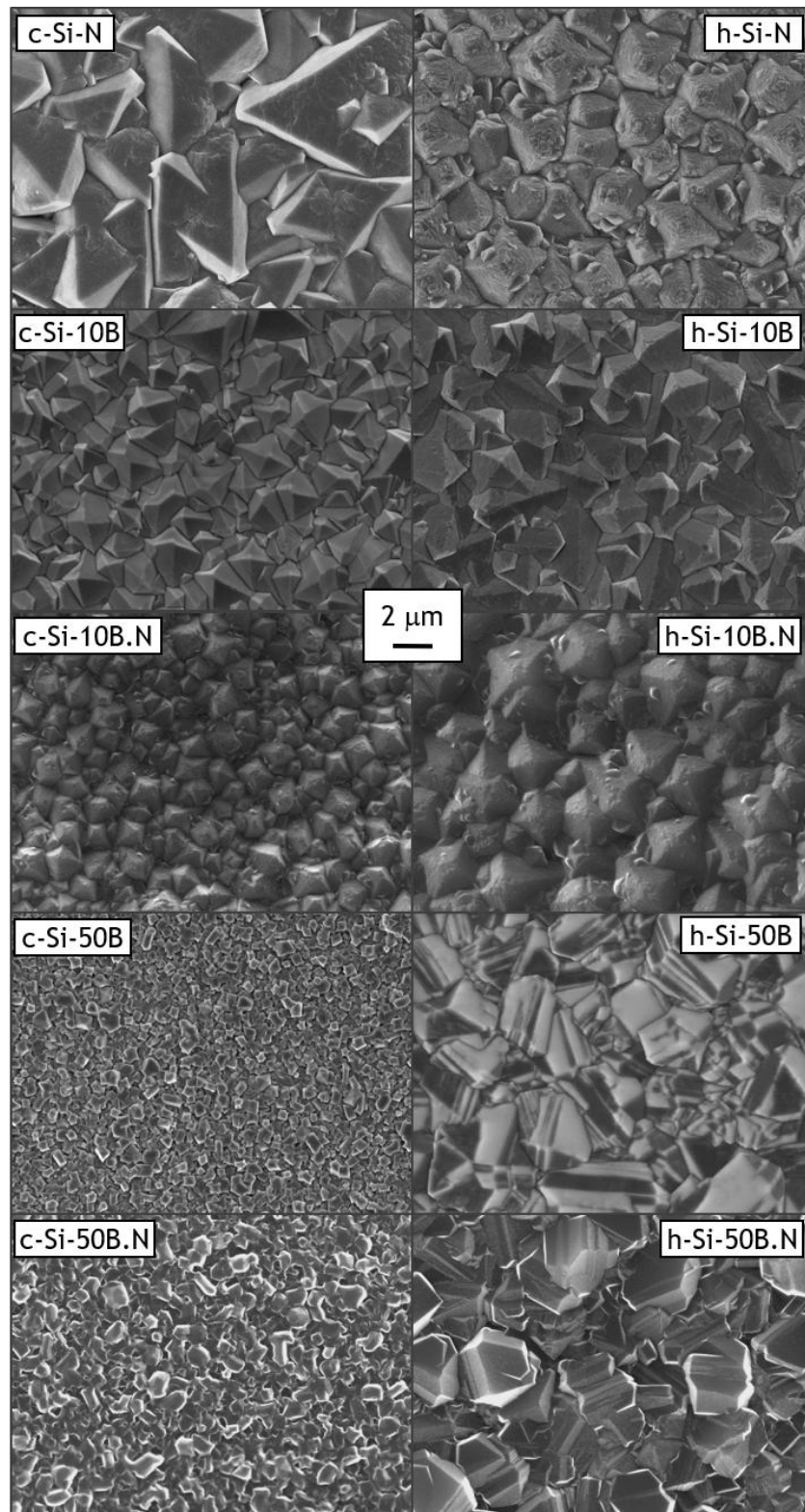
Figure 5.4: Scanning electron micrographs of samples grown on silicon (Si) substrates with a range of doping combinations. All share the same magnification.

addition of nitrogen here does not increase the grain size, but simply reduces the facet
definition.

Increased growth temperature in Si samples with 0 or 10 ppm diborane reduces facet
quality and, in those containing nitrogen, increases twinning. The opposite may be said
for the h-Si-50B and h-Si-50B.N films, having grain sizes much larger and well-facetted
than in their colder counterparts. This is a result of the large growth rate enhancement
of temperature (c.f. figure 5.1) producing larger grains for high [B]. The (admittedly
smaller) enhancement in growth rate in the 10B samples causes slight increases in grain
size whilst reducing facet quality, especially in h-Si-10B.N.

Since the Pc sample set was grown on the polished side of a polcrystalline diamond
substrate, the orientation and texture of the films don't follow the same selective process
that governs films grown on silicon. Figure 5.5 shows images of the Pc sample set
surfaces, with one example of 100 times magnification showing the variably orientated
domains as dictated by the underlying substrate. Morphological characteristics are thus
highly varied within individual samples, something that is true for each in the Pc set.
Since the films are in some sense epitaxial, the grain boundary density should be low
even if the growth surface normal does not coincide with a favourable lattice growth
direction.

5.4.3   Raman spectra

The polycrystalline diamond Raman spectrum contains signatures of the various poten-
tially present carbon allotropes: peaks at 1332 cm^{-1} (narrow) for sp^3 diamond; 1345
and 1550 cm^{-1} (wide) for sp^2 graphitic carbon; 1125 and 1450 cm^{-1} (wide) for polymeric
carbon, common in nano-diamond films [180, 181]. This work is primarily concerned
with the sp^3 diamond and sp^2 graphitic signals since grain sizes are in most cases too
large for polymeric carbon to be detectable. UV excitation causes a good separation of the
1332 cm^{-1} diamond peak and the broad 1550 cm^{-1} graphitic peak (longer wavelengths
can cause the latter to move to lower energies), also providing a strong and consistent
diamond peak across a broad morphology range [182]. Hence normalisation to the 1332
cm^{-1} peak allows comparison of samples based on the relative appearance of the two
graphitic signatures.

The Raman spectra of the c-Si sample set are shown in figure 5.6. Often samples of low
growth rate and small particle size will show high signals of sp^2 carbon due to their high
grain boundary density. Although characterised by its low growth rates in comparison to
other sets, the c-Si set does not fully adhere to this trend. Those without 50 ppm diborane
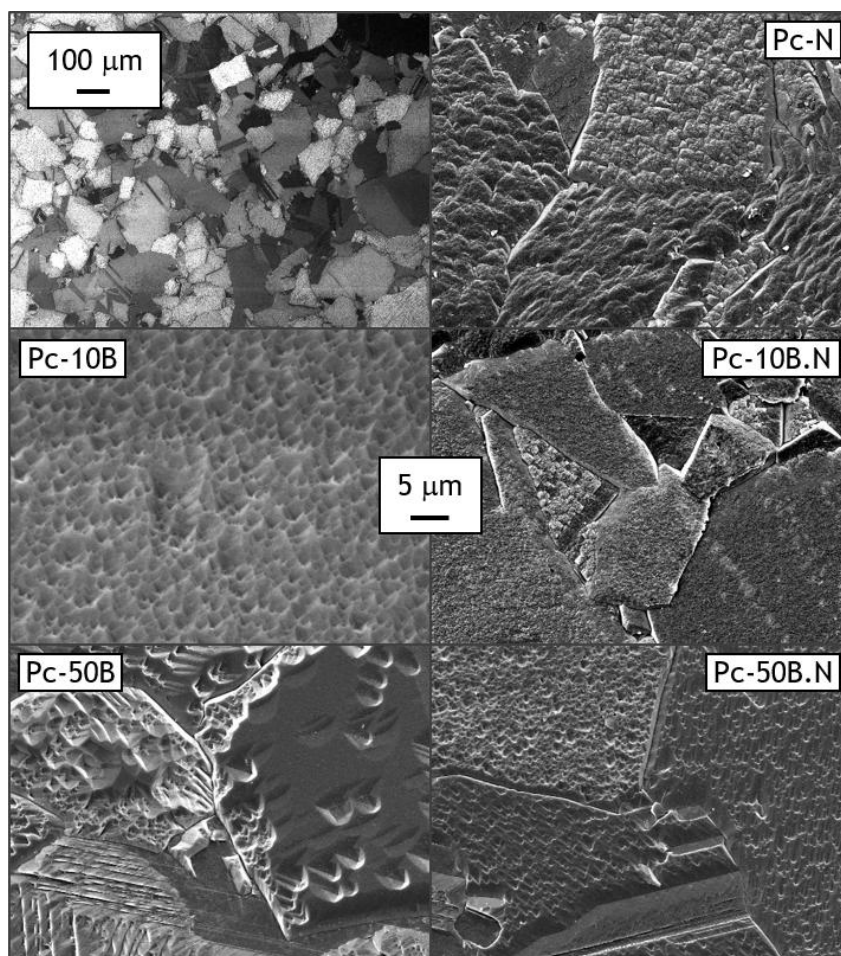
Figure 5.5: Scanning electron micrographs of samples grown on polycrystalline (Pc) diamond substrates. All but the top left (exemplary, low magnification) image share the same magnification.

added show considerable graphitic signatures centred around $1550 - 1600$ cm^{-1} and, as shown in section 5.4.2, are larger in grain size than those with a higher level of boron added. The boron-induced lowering of the so called graphite 'G' peak (at 1500 - 1600 cm^{-1}) is well known [183] and isn't thought to be due to a reduction in graphitic material [184]. Nevertheless, given the effect on growth rates by boron and nitrogen interaction found here and by others [83], a lack of activity of nitrogen-containing species could conceivably be altering the growing diamond surface.

The presence of nitrogen causes considerable facet roughening at 10 and 0 ppm diborane and sp^2 carbon could be present at microscopic surface defect sites. This is apparent, possibly more so, in figure 5.7 where samples grown on hot silicon in the presence of nitrogen (and 0 or 10 ppm diborane) have the highest sp^2 graphitic signatures.
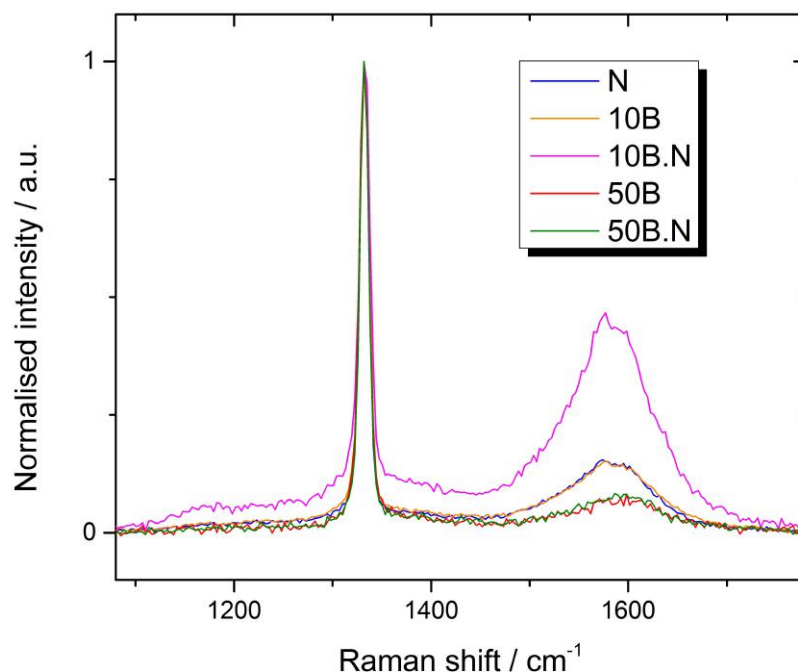
Figure 5.6: Raman spectra of the set of samples grown on cold silicon (c-Si) substrates. The intensities are normalised to the intensity of the ~ 1332 cm^{-1} diamond peak.

This is in agreement with the SEM images in figure 5.4 if the appearance of rough facets and twins are assumed a contributor to the G Raman peak.

Once again, with 50 ppm diborane the Raman spectra of h-Si samples shows minimal sp^2 signal, potentially owed jointly to the large, well defined grains, to the incorporation of boron into the lattice suppressing the sp^2 signature and possibly to lower nitrogen activity caused by interaction with boron.

When compared to c-Si, the effect of larger grain size is apparent in the whole h-Si set apart from h-Si-N. All but the nitrogen-only sample have larger grains and therefore less inherent sp^2 graphitic content, manifesting in lower intensity around $1550 - 1600$ cm^{-1}.

When grown on polycrystalline diamond substrates, films have Raman spectra as shown in figure 5.8. The 1332 cm^{-1} diamond peak is visibly narrower than those of figures 5.6 and 5.7 and even those with the highest G peaks, Pc-N and Pc-10B.N, are of lower sp^2 signal than their silicon substrate counterparts. Once again, the boron in the 50B.N case may be counteracting the presence of nitrogen that causes a small but significant graphitic peak around 1500 cm^{-1} in the N and 10B.N samples.

As may be expected the SC sample set shows no significant peaks apart from the 1332 cm^{-1} diamond peak, shown in figure 5.9. Assuming these spectra result from the grown film and not the substrate beneath, this is a useful confirmation that the single crystal substrate samples are in fact epitaxial films with at least a near-continuous
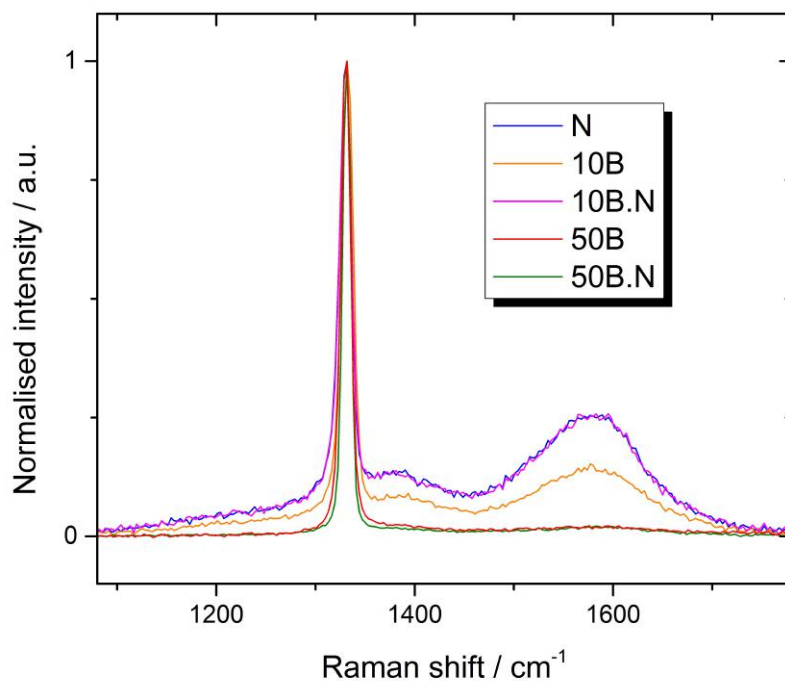
Figure 5.7: Raman spectra of the set of samples grown on hot silicon (h-Si) substrates. The intensities are normalised to the intensity of the $\sim 1332\ \mathrm{cm}^{-1}$ diamond peak.
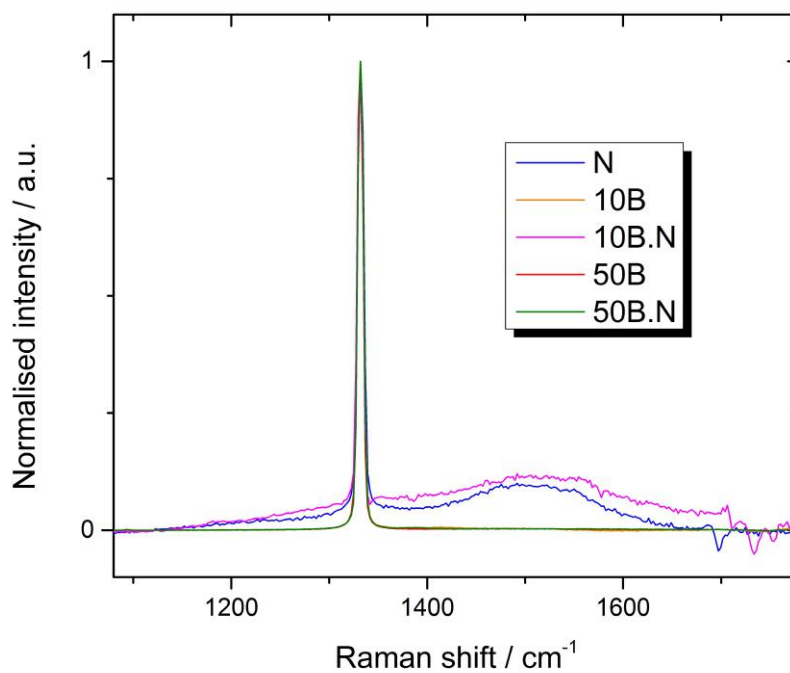
Figure 5.8: Raman spectra of the set of samples grown on polycrystalline (Pc) diamond substrates. The intensities are normalised to the intensity of the $\sim 1332\ \mathrm{cm}^{-1}$ diamond peak.
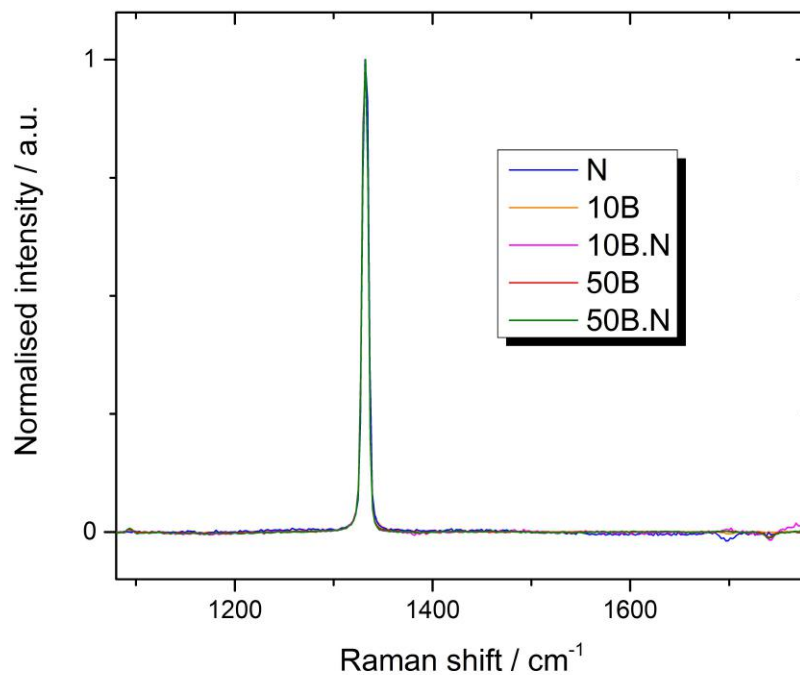
Figure 5.9: Raman spectra of the set of samples grown on single crystal (SC) diamond substrates. The intensities are normalised to the intensity of the ~ 1332 cm^{-1} diamond peak.

crystal constituting the grown layer.

5.4.4 Dopant concentrations

An example SIMS depth profile is presented in figure 5.10, showing both nitrogen and boron concentrations over time. Since they are not collected at equal beam magnifications the etch, or bore, rate will be different; this is assumed not to affect concentration data since they are acquired from ratios of ions and not absolute values. Due to rapid changes in measured concentration, SIMS measurements of the sample surface were deemed unreliable and care was taken to include data from 'beyond' the surface only in the averaged data in the following figures.

One point of note for the data presented here is that CN^-, the ion detected in order to measure nitrogen concentration, has the same mass as $C_2H_2^-$. This means that in every CVD film (which inherently contain hydrogen), there is always some apparent level of nitrogen which may or may not in fact be nitrogen. This is discussed further below. There is no equivalent for B^+, so its detection unequivocally signifies the incorporation of boron.

As is shown by the data in figure 5.11, the incorporation efficiency of boron in the c-Si sample set is approximately 100 %. In contrast to previous HF work [80], both the N-containing and N-free boron doped samples have around the same boron concentration. An incorporation efficiency of 100 % does not imply that the energy barrier to addition
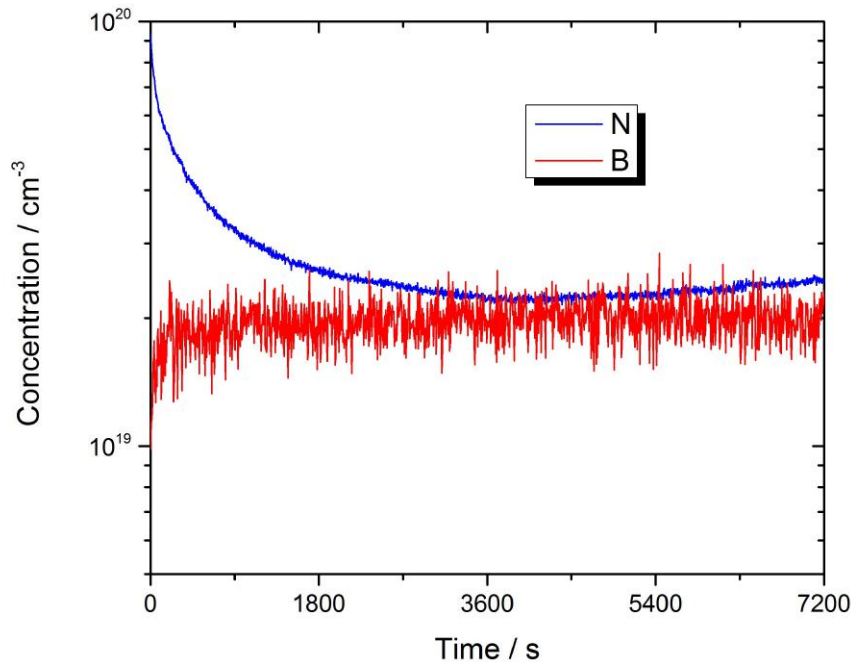
Figure 5.10: Boron and nitrogen concentration against time as measured during a secondary ion mass spectrometry depth profile experiment. This example is for h-Si-50B.N.

of boron to the lattice during growth is the same as that for carbon, but that (given the barrier may be larger) the quantity of incorporable boron species in the plasma compared to diborane added is higher than the incorporable carbon species compared to methane added.

The nitrogen concentrations in c-Si-N and c-Si-10B.N are far higher than those of boron in c-Si-10B and c-Si-10B.N, but their N incorporation efficiencies are only 0.9 and 2.2 % respectively. This is largely due to the small dissociation fraction of N_2 in the near-substrate part of the plasma [114]. Whilst [N] incorporated into c-Si-10B.N is higher than in c-Si-N, c-Si-50B.N has a lower concentration than both with an efficiency of 0.3 %.

Higher temperatures reduce the incorporation probability of dopants such as nitrogen [185], an effect visible when comparing the c-Si data to the h-Si data shown in figure 5.12. The nitrogen incorporation efficiencies here are 0.44, 0.51 and 0.46 % for h-Si-N, h-Si-10.BN and h-Si-50B.N respectively.

Since boron is substituted for carbon with a lower energy barrier than N (see chapter 3), its incorporation is less affected by temperature. Thus the concentrations of boron in h-Si-10B and h-Si-10B.N are similar to those of c-Si-10B and c-Si-10B.N. Although somewhat different to each other, the 50 ppm diborane h-Si samples are in fact also relatively similar to their cold silicon counterparts.
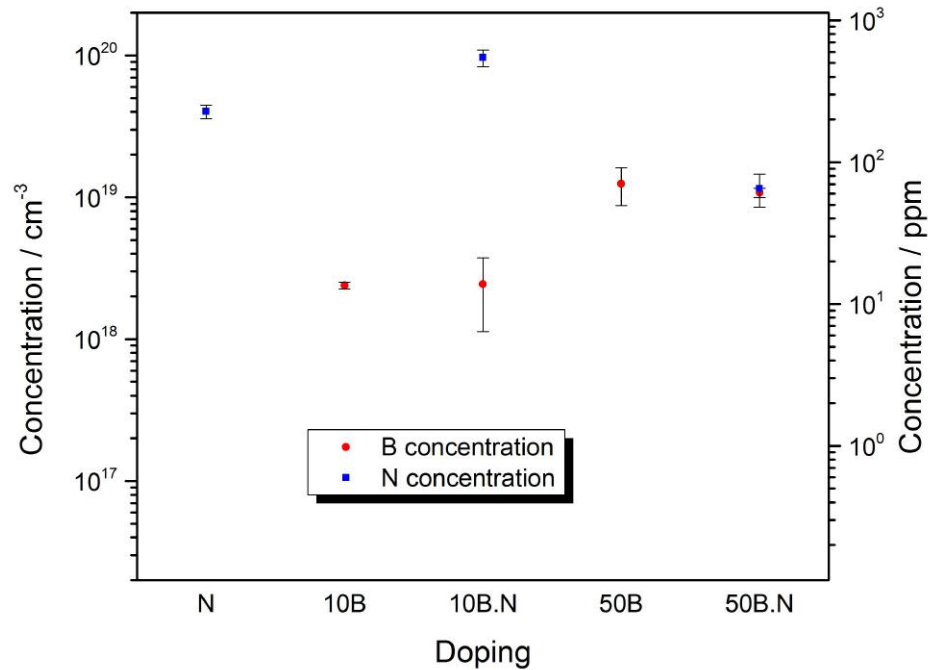
Figure 5.11: Boron and nitrogen concentrations as measured by secondary ion mass spectrometry for samples grown on cold silicon (c-Si) substrates.

The nitrogen and boron contents measured in the Pc sample set are shown in figure 5.13. The nitrogen levels of Pc-N, Pc-10B.N and Pc-50B.N are similar to those of the Si sample sets. As a control, the N concentration of Pc-10B and Pc-50B were examined as well, which turned out to be particularly high compared to what might be expected. If considered to be due to nitrogen (CN$^-$) then incorporation efficiency would be ~ 15,000 % based on a 1 ppm N$_2$ impurity level in the reactor (nominally an overestimate). As mentioned, C$_2$H$_2^-$ detection means that a minimum signal for apparent nitrogen incorporation will exist due to incorporated hydrogen. Hence, for the Pc and SC data a nitrogen concentration of ~1 × 10^{19} cm^{-1} is considered an approximate detection limit, below which nitrogen is insignificant. The trend across the samples N, 10B.N and 50B.N for the Pc set in figure 5.13 is qualitatively similar to that of the c-Si set (grown at similar temperatures) in figure 5.11, implying that trace boron addition could increase the incorporation of nitrogen at low growth temperature. Further samples would be required to confirm this.

Boron content in Pc-10B and Pc-10B.N is similar to that in the Si set, representing a rough incorporation efficiency of 100 % once again. However, the same cannot be said
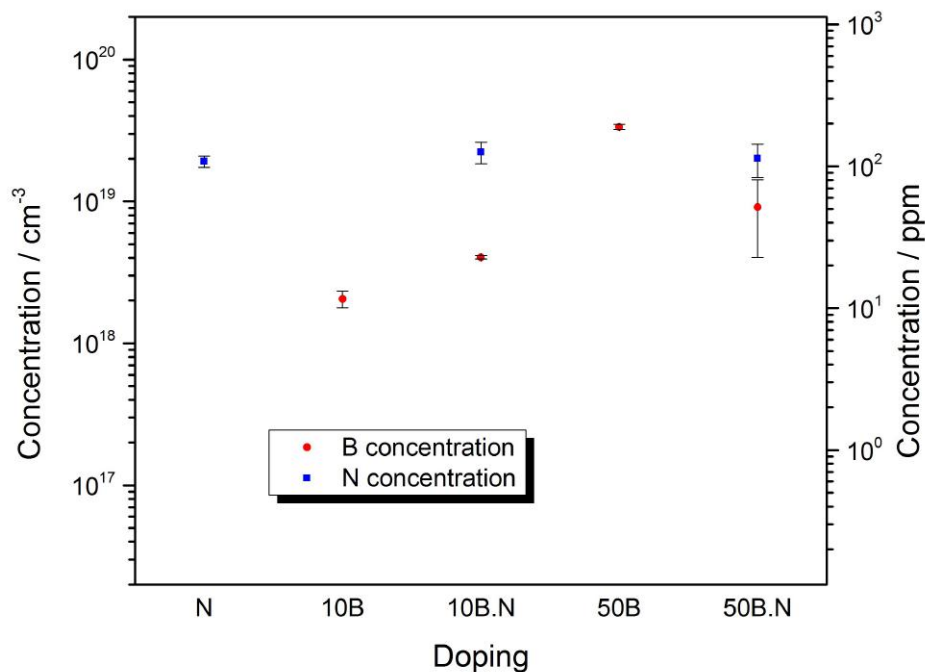
Figure 5.12: Boron and nitrogen concentrations as measured by secondary ion mass spectrometry for samples grown on hot silicon (h-Si) substrates.

for Pc-50B and Pc-50B.N, which both have [B] far lower than expected. Sufficient repeat measurements were carried out on all samples to ensure standard errors were minimal, as is shown by the error bars in the figures. This leaves a systematic error, either with the measurement or the growth of the diamond itself. Given that a similar result is apparent in the SC sample set (see below), it is unlikely to be due to a growth problem. It is possible that the low thickness of 50 ppm diborane samples detrimentally affects the SIMS measurements. Further work, perhaps using samples varying only in their thickness, would be needed to clarify this.

Incorporation of dopants in (100) orientated single crystal diamond is low [178], an effect reproduced by the SC boron and nitrogen concentrations shown in figure 5.14. The levels of nitrogen in the SC-N, SC-10B.N and SC-50B.N are reduced by the increasing diborane in the plasma and even reaching the $C_2H_2^-$ limit with 50 ppm diborane present during growth. This is unexpected considering the result from OES (chapter 4) that showed diborane not reducing NH and N_2 emission intensities over a larger range of process gas concentrations than is explored here. As was also discussed previously, in the plasma there is a large nitrogen reservoir available in N_2, possibly resulting in a
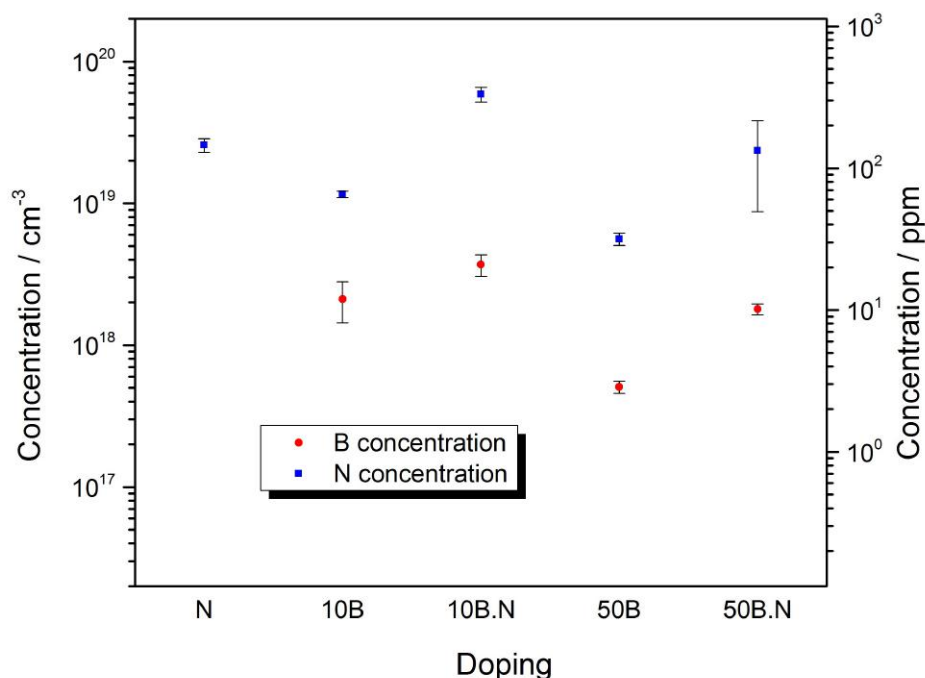
Figure 5.13: Dopant concentrations as measured by secondary ion mass spectrometry for samples grown on polycrystalline (Pc) diamond substrates

minimal influence of boron in the gas phase. This would imply the action of boron on nitrogen incorporation is either in the near-substrate region of the plasma or within the surface of the growing diamond.

Additionally, the boron concentrations in the SC sample set are roughly a factor of 5 below those of the polycrystalline samples. The addition of nitrogen appears to reduce the incorporation of boron, as may also be expected given the discussions of chapter 4. It is not clear why this did not happen for polycrystalline diamond samples; their inherent complexity making interpretation difficult. A possible explanation for this result in polycrystalline diamond is the existence of (111) facets, where the incorporation of dopants is high in comparison to (100). Further experimentation, perhaps using (111) single crystal substrates, is required.

SC-50B has a similar boron concentration to SC-10B, which may be the result of variations within the material since even a significant number of measurements of SC-50B yielded standard errors larger than satisfactory. Even more so than the Pc sample set, the low thickness of the SC set may have some effect on the results causing the 50
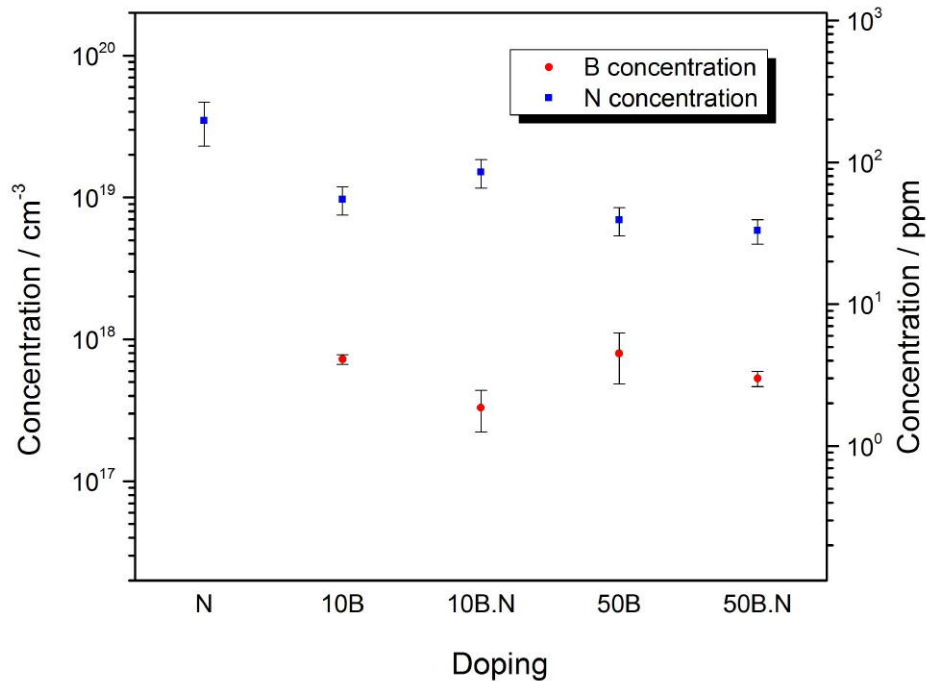
Figure 5.14: Dopant concentrations as measured by secondary ion mass spectrometry for samples grown on single crystal (SC) diamond substrates

ppm diborane doped samples to show unrealistic values; again, this needs clarification by testing samples with different thicknesses.

The N and B concentrations in both SC-10B.N and SC-50B.N are reasonable compared to their respective control samples. Firstly, N content is reduced compared to SC-N, possibly due to boron either in the gas phase or during incorporation. Second, B content is reduced compared to SC-10B and SC-50B, possibly due to similar interactions with nitrogen. With a single facet dominating the growth, the single crystal sample set provides the simplest model system for doping with two dopants; the most simply interpreted results are often presumed the most reliable. As mentioned a further study using (111) orientated substrates as well as (100) would be enlightening, perhaps with a broader range of process gas dopant concentrations.

5.4.5   Temperature-dependent resistivity

In order to produce a consistent Ohmic conducting contact to the diamond for electrical measurements, two methods were chosen. Firstly, titanium and then gold were sputtered
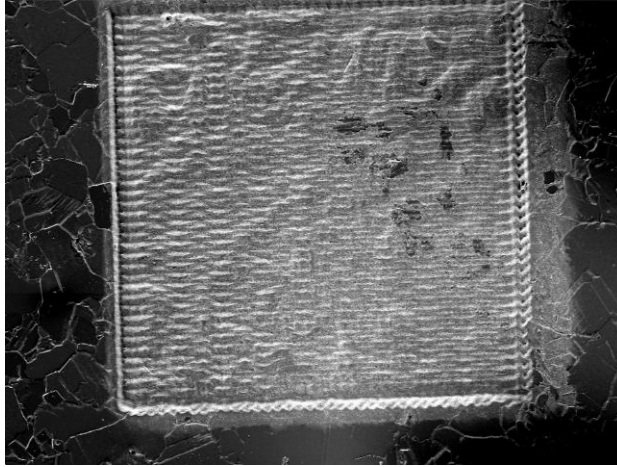
Figure 5.15: A SEM image of a laser-graphitised conducting contact on a sample grown on polycrystalline diamond. The contact is 0.75 × 0.75 mm in size.

onto the Pc and SC samples through a laser-cut silicon mask. These samples were tested by RT VDP before vacuum annealing the samples and testing again. The Ti-Au combination is known to produce low resistance contacts on semiconducting diamond [186, 187]. However, a thickness of ~ 5 nm Au, 200 nm Ti and a 625 °C, 2 minute anneal did not produce Ohmic behaviour in the contacts. Additionally the Ti-Au contact achievable here was not considered robust enough to survive the temperature range required for TVDP measurements.

The second contact type produced on the ten diamond substrate samples was a laser-etched graphitic contact on the diamond surface. This method has the advantage that conductive material is produced in preexisting intimate contact with the sample film [188]. Laser milling apparatus (Oxford Lasers) was used with a low power during a bespoke square milling program adapted for this purpose. The squares, of side length 0.75 or 1.00 mm (for SC or Pc respectively), were milled at gradually increasing input powers until the surface was visually blackened, signifying graphitisation. Figure 5.15 shows a SEM image of an example contact on a Pc sample. These contacts were conducting from room temperature to at least 900 °C.

Temperature dependent VDP resistance measurements were recorded using each Pc and SC sample, the latter resting on a polycrystalline diamond base as a laser-absorbing heater. Sheet resistance R_S was calculated using equation 2.15 and thickness d using SIMS bore times. The resistivity $\rho = R_S d$ can be plotted on a log-scale against the reciprocal temperature, the gradient of which is dependent on the thermal activation energy of majority charge carriers in the sample. As mentioned in section 2.4.3, the donor/acceptor density has a $\frac{3}{2}$ power dependence on T and the mobility has approximately the inverse T dependence. This assumption allows E_A to be estimated from the gradient of the plots,
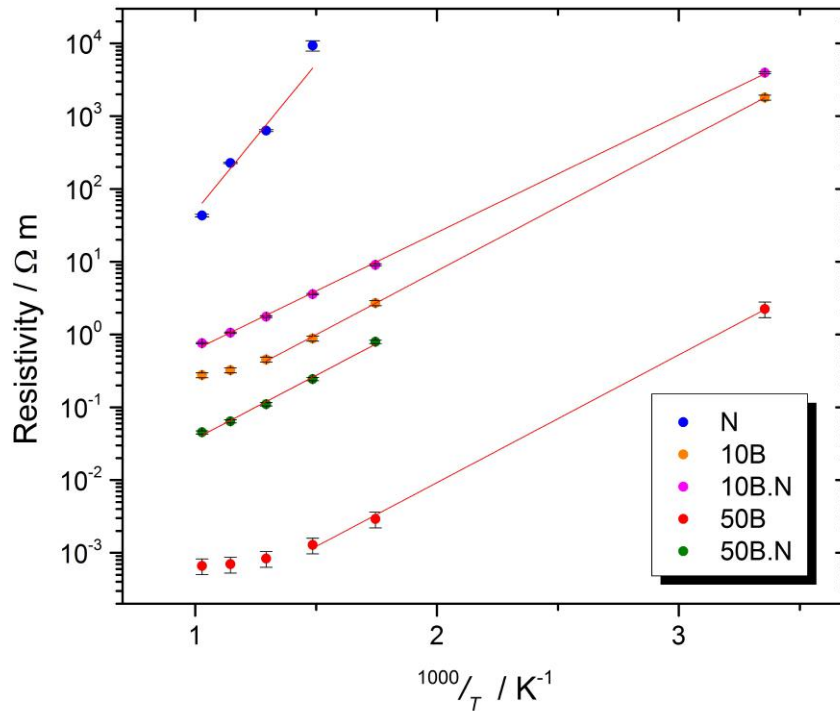
Figure 5.16: Resistivity against reciprocal temperature for samples grown on polycrystalline (Pc) diamond substrates. Red linear fits are drawn over points used in gradient calculations.

which are shown for Pc samples in figure 5.16 and for SC samples in figure 5.17.

The purely nitrogen doped Pc-N and SC-N samples were, somewhat expectedly, the least conductive. Their gradients were large, implying a high carrier excitation energy, in qualitative agreement with the well-known donor level of the N dopant being 1.7 eV below the conduction band minimum [32].

Containing boron, the Pc and SC 10B and 50B samples were predictably less resistive than those doped with only nitrogen. Their fitted gradients are lower than those of the N samples as well, corresponding to the low activation energy of the boron acceptor [28].

It may seem rational that introduction of boron to a sample otherwise containing nitrogen would reduce the energy required to move charge. However, considering the measured concentration of nitrogen in the Pc films is higher than that of boron (and the $C_2H_2^-$ limit), the boron acceptors should be largely compensated. The slope of the 10B.N and 50B.N samples appear similar to those of the boron doped samples, implying carriers with similar excitation energies. In most cases though, the conductivity of films with nitrogen added, 10B.N and 50B.N, is lower than that of the equivalent boron-only film, 10B and 50B, in agreement with previous research [70].

To estimate the excitation energy, some high temperature data points had to be omitted in fitting the TVDP data to equation 2.16. This is due to a conduction regime
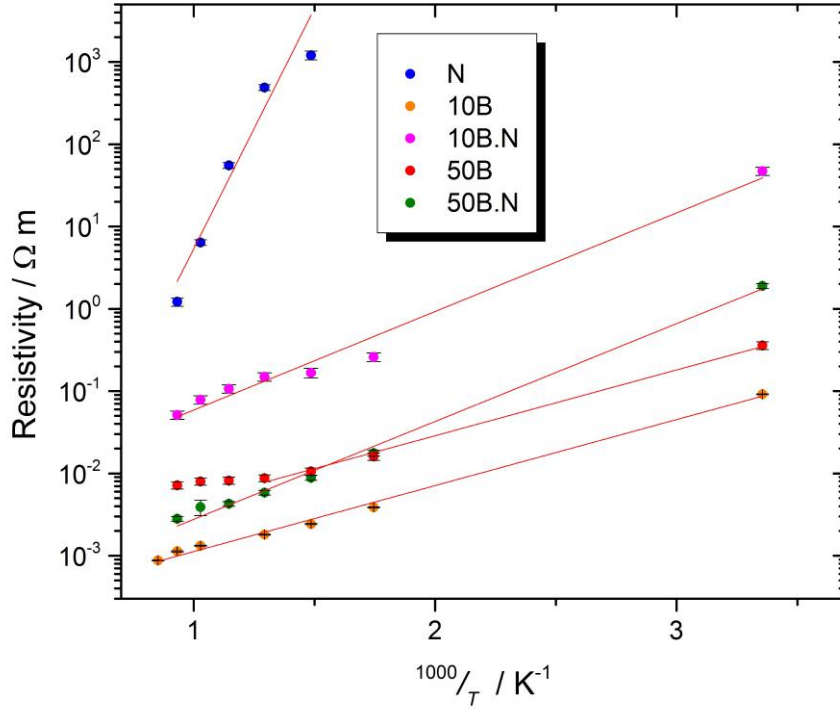
Figure 5.17: Resistivity against reciprocal temperature for samples grown on single crystal (SC) diamond substrates. Red linear fits are drawn over points used in gradient calculations.

change happening in the purely boron-doped samples, which causes the gradient to change at high temperature [128]. Dependent on the impurity activation energy and the defect concentration, at some temperature the movement of charge switches from an ionised impurity-related valence (or conduction) band mechanism to a mid-gap level conduction regime in which carriers hop between impurities. Interestingly, the only samples for which this happened were boron-doped samples, despite not necessarily being the most conductive films; at high temperature SC-50B.N is more conductive than SC-50B.

The estimated E_A values are given in table 5.3. Both the Pc-N and SC-N activation energies are far lower than the expected 1.7 eV. This could be affected in some way by grain-boundaries in the Pc sample, but it is unclear what causes the 1.2 eV value in SC-N. One possible explanation could be that the graphitic contacts are less than perfectly conducting at low temperatures on this generally highly resistive sample, becoming less resistive at elevated temperature and skewing the response of R_S to T. The thickness of these samples was estimated from SIMS bore-times, which may be a suspected factor in these discrepancies, but since E_A is derived from the gradient of a log-plot it is purely the exponent of the resistivity temperature-dependence of importance here. The large errors on E_A for Pc-N and SC-N, which visibly originate from the poor fits in figures 5.16

Table 5.3: Thermal activation energies as estimated from temperature dependent VDP
resistivity measurements. Estimates make the approximation that μ and N in equation
2.16 have equal but inverse T dependence.

Sample	Activation energy, $E_{A,VDP}$ / eV	
doping	Polycrystalline (Pc)	Single crystal (SC)
N	0.8 ±0.2	1.2 ±0.2
10B	0.348 ±0.003	0.159 ±0.004
10B.N	0.319 ±0.003	0.24 ±0.01
50B	0.35 ±0.01	0.14 ±0.01
50B.N	0.35 ±0.01	0.24 ±0.01

and 5.17, could be reduced by repeating the experiment further and at a greater number
of temperatures. This may result in E_A values for nitrogen conduction more in line with
previous findings.

In the Pc sample set, boron induces an activation energy for carriers of 0.32 - 0.35 eV,
in very good agreement with previous work [128, 189]. The presence of nitrogen appears
to make little difference, with Pc-10B.N even showing the lowest activation energy,
an effect explicable with reference to its highest [B] (shown in figure 5.13) whereby
activation energy is reduced with increased concentration [30, 128]. The very fact that
E_A for Pc-10B.N and Pc-50B.N is similar to those of the boron-only samples implies that,
potentially, very little nitrogen is actually active in these samples. This could be true,
however section 5.4.6 presents data may cast doubt on this possibility.

The SC samples show activation energies that are lower than those of the polycrys-
talline diamond set. SC-10B and SC-50B show low activation energies compared to the
rest of the set, with higher boron:nitrogen ratio (as measured by SIMS as well as nomi-
nal) causing the lowest E_A. Those with nitrogen added have higher activation energies,
which could be the result of lower [B] (see figure 5.14), or compensating nitrogen in the
films. Importantly, SC-50B.N has the same E_A as SC-10B.N, which does appear to have
a non-zero concentration of nitrogen incorporated.

5.4.6   Thermionic emission

Thermionic emission can be used to qualitatively assess the semiconducting nature of
diamond. Previous work [39, 40] has made confident fits of data to the theory (see section
2.4.4) without too much consideration of its applicability. As discussed, material-related
drawbacks mean quantitative analysis is precluded. For this reason thermionic emission
is used based on the following factors: to emit electrons a sample must be conductive;
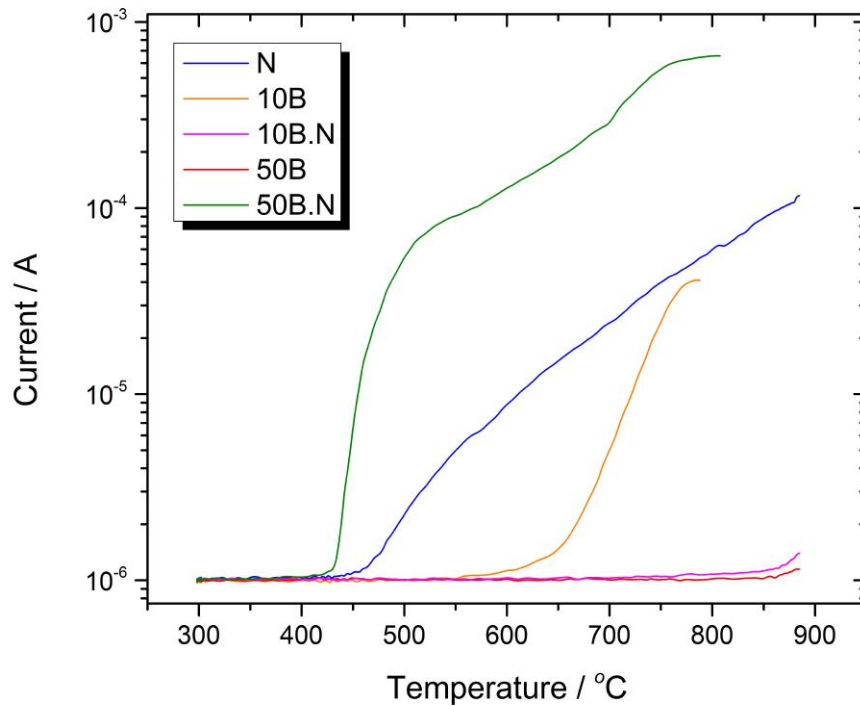
Figure 5.18: Thermionic current against temperature for samples grown on polycrystalline (Pc) diamond substrates.

the sample work function must be small so that sufficient electrons are available for emission (also usually requiring negative electron affinity); to have a small enough work function a sample should be n-type. These assumptions are often made in the previous literature [190]. Thermionic emission has been reported previously for boron-doped (p-type, high work function) diamond [191, 192], but with thermionic currents of < 1 nA at over 1000 °C.

Figure 5.18 shows the thermionic emission data collected for the Pc sample set. Nitrogen is the most common dopant in diamond studied by thermionic emission [39, 132, 193] as it is relatively easily incorporated into diamond films and gives detectable emission in most cases. The emission threshold temperature and maximal current shown here for Pc-N is typical for nitrogen doped microcrystalline diamond in the apparatus used. Judging by the results of section 5.4.5, in which carrier activation energies imply majority carriers provided by boron acceptors, one would not expect significant emission current from any other sample in the Pc set. This is not the case, with both Pc-10B and Pc-50B.N producing significant emission currents at temperatures below 800 °C.

The thermionic emission character shown here appears not to be correlated with conductivity, with the most conductive sample, Pc-50B, not producing more than 1 μA of thermionic current. This cannot be purely a boron-related inability to emit, since Pc-10B emits fairly strongly. Pc-10B does have a high emission threshold temperature compared

to the other two strong emitters, understandable for the one emitter lacking in nitrogen, but still this sample emits much more strongly than similar samples in the literature [192].

Pc-50B.N is, most unexpectedly, the strongest emitter both in threshold temperature, where it outperforms its N-doped counterpart by ~ 25 K, and in emission current, where it outperforms nitrogen by an order of magnitude for almost the whole temperature range examined.

There is no clear reason why Pc-10B and Pc-50B.N emit significantly but Pc-50B and Pc-10B.N do not. However, Pc-10B, which has a lower resistivity than Pc-10B.N, also has a lower B concentration than the sample with nitrogen present. This could mean that the Fermi-level is relatively high whilst maintaining high enough electrical conductivity to replenish charge carriers whilst emitting. Unfortunately, the same argument contrasting Pc-50B with Pc-50B.N would mean the opposite of the results given, with Pc-50B outperforming Pc-50B.N, which is not the case. On the other hand, Pc-10B and Pc-50B.N did contain a very similar concentration of boron, roughly 10 ppm. Perhaps this concentration of boron in polycrystalline diamond causes stronger thermionic emission characteristics than might be expected. Further experiments are required before any firm conclusions can be drawn. Dr Joshua Lay found, through conductive atomic force microscopy (AFM) studies [194], that on the nano-scale some areas of a boron-doped diamond surface can be insulating. This might mean that these areas effectively have a lower work function than the surrounding conductive film, potentially facilitating both emission and charge replenishment. Perhaps conductive AFM could elucidate whether the films here have areas of low work function despite their overall charge carrier majority being boron-related.

5.5 Conclusion

5.5.1 Summary

Nitrogen and boron have been added to the process gas mixture during MP-CVD growth of diamond on silicon, polycrystalline diamond and single crystal diamond substrates. Various types of characterisation of the sample sets yielded significant changes in many growth and material properties, which can largely be related to the differing plasma gas composition.

The control samples containing nitrogen showed fast growth rates between 5 and

$10~\mu$m h^{-1} depending on the temperature and material of the substrate. Their polycrystalline morphology, again dependent on temperature, was dominated by fast (100) facet growth and for cold and hot growths was (111) orientated and (100) orientated respectively. The nitrogen appeared to induce some facet roughening, in agreement with the size of the sp^2 signatures in the N-doped Raman spectra. Si substrates understandably produced nitrogen doped diamond with the most sp^2 content due to the presence of grain boundaries, with Pc and SC sample sets showing respectively lower graphitic peaks. The nitrogen concentration in c-Si-N was $3.9 \pm 0.4 \times 10^{19}$ cm^{-3}, whilst h-Si-N had half that amount due to reduced incorporation at higher growth temperature. Pc-N showed [N] = $2.5 \pm 0.3 \times 10^{19}$ cm^{-3} and SC-N surprisingly incorporated $3.5 \pm 1.2 \times 10^{19}$ cm^{-3} nitrogen, though note the large standard error. The Pc and SC samples showed high resistivities, with large T gradients resulting in thermal carrier activation energies of 0.8 ± 0.2 and 1.2 ± 0.2 eV respectively. This is lower than the literature value of 1.7 eV, possibly due to the limited data-set size used here. The nitrogen doped Pc sample showed typical thermionic characteristics, with an emission threshold temperature of $\sim 450\,^\circ$C and a current at $750\,^\circ$C of $40~\mu$A.

Boron doped control samples, either grown with 10 ppm or 50 ppm diborane in the process gas mixture, showed slower growth than the N samples. On cold and hot silicon, 10 ppm B$_2$H$_6$ resulted in growth rates of 3 and 5 μm h^{-1} respectively, while 50 ppm gave rates of 0.3 and 2.3 μm h^{-1}. This is thought to be due to boron in the gas phase mitigating the growth rate enhancing effect of any present nitrogen, though the mechanism is unclear. Similar rate suppression was found on diamond substrate samples. On silicon, 10 ppm diborane produces diamond with (100) and (110) orientation and (111) facetting, whereas 50 ppm produces apparently random morphology when grown cold, but well-defined (100) and (111) facets at higher temperature. The effect of boron on Raman spectra is a clear reduction in sp^2 signatures by 50 ppm diborane, but for only 10 ppm the broad peak around $1550 - 1600$ cm^{-1} is clearly visible for Si samples. On Pc and SC samples there is no apparent sp^2 character, though it may physically be present in the samples. Concentrations of boron in Si boron doped samples are roughly as expected from a 100 % incorporation efficiency, with slight variability. However, the Pc sample set has unexpectedly low [B] for 50 ppm diborane, a discrepancy with no clear cause. Low concentrations are found for SC samples due to the (100) growth orientation and 10 and 50 ppm both result in $4 - 5$ ppm incorporated in the films. Resistivities of boron doped samples are low over the range of temperature studied, with gradients that show activation energies in agreement with the literature: < 0.4 eV. Linear fits used

to calculate E_A values omitted points due to conduction mechanism switching at the highest temperatures. Surprisingly the Pc-10B sample showed considerable thermionic emission, with a threshold temperature of $\sim 600\,°C$ and a current at $750\,°C$ of $7\,\mu A$.

Co-introduction of boron and nitrogen results in somewhat similarly suppressed growth rates to those of the 10B and 50B samples, with c-Si-10B.N and h-Si-10B.N growing at a rate of 2.6 and 6.5 $\mu m\,h^{-1}$ respectively; nitrogen potentially enhancing the growth rate of the latter but not the former. The Si-50B.N samples have thicknesses almost equalling those if the Si-50B samples, likely owing to the abundance of boron compared to nitrogen, suppressing the enhancement effect. Growth rate trends in the SC sample set are qualitatively similar to those of the Si sets, but with a larger enhancement of SC-10B.N compared to SC-10B, considerably enhancing the rate above that of the boron-only case. Nitrogen addition fails to increase growth rate of SC-50B.N over that of SC-50B. Visually, boron and nitrogen additions cause morphologies most relatable to the respective boron-only samples, with slight variations. These take the form of facet roughening/twinning and slight grain-size increases, apparent in h-Si-10B.N and c-Si-50B.N respectively. The large boron presence with 50 ppm of diborane appears to hinder any significant morphological changes that nitrogen may otherwise cause. The small grains caused by co-doping in c-Si-10B.N manifest in a large graphitic sp^2 signal in its Raman spectrum, higher even than that of c-Si-N. The opposite effect happens for all other additions of boron to the otherwise nitrogen-containing samples (apart from h-Si-10B.N), a known effect due to incorporated boron in the film. Nitrogen incorporation shows similar trends in Pc and c-Si, a flat (boron-independent) trend in h-Si and a reduction in SC upon increased diborane. This variation in trends could be the result of morphological differences and their effect on incorporation efficiency. Boron is largely incorporated as efficiently in B.N samples as in B samples, indicating little interaction in the gas phase. By contrast the SC set sees a reduction in boron concentration in films grown in the presence of nitrogen. The SC sample set is thought to provide a simpler model for incorporation as its growth involves progression in a single lattice direction, hence it has dopant concentrations closer to what might be expected. Boron and nitrogen codoped samples largely had conductivities between those of boron doped and nitrogen doped samples, with temperature dependences close to those of boron. The calculated activation energies confirmed that the majority carriers were the same as those of the boron doped samples, with values also < 0.4 eV. Single crystal E_A values for B.N samples were larger than those of the B samples, in agreement with the lower boron concentration. Despite the apparent dominance of boron in Pc-50B.N, which implies the

material is p-type, its thermionic emission was an order of magnitude higher than that
of Pc-N with a threshold temperature of ~ 425 °C and a current at 750 °C of 345 μA.

5.5.2   Future work

In light of the results presented, this type of study would benefit from further increasing
the sample set size. Data reliability and the consequent conclusions drawn could be
enhanced not only by repeat experiments with new samples grown under the same con-
ditions, but also by growing samples under a broader range of conditions. Concentrating
on h-Si and SC substrates, the process parameter range could be extended to include,
for example, 1, 3 and 25 ppm diborane and 12300, 49200 and 98400 ppm nitrogen.
This would give a comprehensive co-doped sample set which could be used for all the
experimental techniques carried out here, whilst allowing observation of trends across
the doping range. These suggested process gas concentrations would require growth of
30 samples per substrate (before repeats). A limited set may be sufficient and if so the
lower diborane and higher nitrogen concentrations should take priority.

The SC sample set should in the future be the main set used for thermionic emission
experiments. It is well-known that morphology and sp^2 content affect conductivity, so
eliminating these influences from the experiment is imperative. Since the most financially
viable substrate size for single crystal diamond samples is a 3 mm square, the thermionic
apparatus would need some simple modifications. Shown in figure 2.7, the collector would
need to be remade with a smaller diameter, which could be as little as ~ 2 mm, and the
quartz plate would need to be remade with a smaller diameter hole below the diamond
emitter. Additionally, a deposition of nano- (or ultranano-)crystalline diamond on the
underside of the diamond prior to growth of the sample films would provide sufficient
absorption of the 10.6 μm IR laser for the single crystals to be heated without the aid of
a separate absorbing object.

Hall effect measurements are possible using some of the apparatus used here for VDP
measurements, but in ambient conditions and using a 1 T permanent magnet. Conductive
Ohmic contacts are required (even more so than with VDP) for reliable Hall data to be
acquired, so it may be necessary to produce contacts via a method similar to that first
attempted here. The deposition and annealing steps would require optimisation. If this is
possible then the semiconducting properties of the films could be determined, including
whether they are n- or p-type and their charge carrier mobilities. The aforementioned
conductive AFM studies would also be useful to examine the electical properties of the
films on the nano-scale.

With regards to boron-nitrogen clusters, such as those examined in chapter 3, various experimental techniques could be employed. Both X-ray absorption near edge structure (XANES) and electron energy loss near edge structure (ELNES) can provide information on the bonding state of specific elements in bulk materials, but require the use of a synchrotron beam-line or high-resolution transmission electron microscope (TEM) respectively.

Solid state nuclear magnetic resonance (NMR) spectroscopy is a further experimental technique able to provide information on bonding. This requires a nuclear spin, which the 14 baryon nucleus of nitrogen does not possess, so the use of $^{15}N_2$ would be required during growth in order to produce coordinated structures detectable by NMR. The 11 baryon (most common isotope) nucleus of boron has the required nuclear spin to be active in NMR spectroscopy.

Before carrying out experiments that attempt to detect coordinated boron and nitrogen, production of clusters could be attempted by HPHT treatment. This would facilitate migration of dopants provided the temperature reached was above $\sim$ 1400 °C [66]. Considering the large binding energies of boron-nitrogen complexes (as studied in chapter 3), their formation would be quite possible.

6.1 Overview

This thesis presents three aspects of the combination of boron and nitrogen in diamond. Namely, chapter 3 contains a computational study of boron-nitrogen substitutional dopant clusters in the diamond bulk. Chapter 4 presents an optical emission spectroscopy examination of diamond CVD plasmas to which both diborane and nitrogen were introduced. Finally, for chapter 5 various samples of boron-nitrogen co-doped diamond were grown by MP-CVD and characterised by a range of techniques, with results of growth-rates, morphologies, dopant incorporations and electrical characteristics presented.

Density functional theory (DFT) was combined with Hartree-Fock (HF) theory in hybrid HF-DFT calculations of boron-nitrogen clusters. The calculations, performed on single clusters of up to $n = 5$ foreign atoms in supercells totalling 512 atoms, gave structural, energetic and electronic energy level predictions. For comparison, the set of 22 clusters was divided into groups containing: single element clusters ($n \leq 3$), symmetric clusters (a central B or N atom surrounded by up to 4 of the other), and asymmetric clusters (a central B or N atom surrounded by up to 3 of the same atom and one of the other). In addition, comparisons were made between N-rich, B-rich and equal B-N constituted clusters. Nitrogen-rich clusters showed low symmetries, with the characteristic elongation of one C-N bond found in single substitution nitrogen manifesting in clusters of multiple atoms. The asymmetric N-rich clusters were in general more stable

than their symmetric counterparts, and produced electronic energy levels deeper in the band-gap. By contrast, the boron-rich clusters maintained higher symmetry during geometry optimisation and showed lower variance in bond lengths compared to the pure diamond carbon-carbon bond. The electronic levels of the stable symmetric boron-rich clusters were similar to that of the single substitutional boron dopant. Judging by their stability, some of these predicted defects could be present in HPHT treated material containing both boron and nitrogen.

The spectroscopic investigation of diborane- and nitrogen-containing MP-CVD plasmas yielded many results in-line with previous findings. Boron and nitrogen content was varied in N/H, B/H and B/N/H plasmas, giving linear trends in NH, N_2, BH and B emissions and consequently implying linear concentration trends. In B/N/H plasmas, the effect of nitrogen addition was to quench B and BH emissions, most likely due to chemical reactions lowering the concentration of these species. Reactions analogous to those producing C_2H_2 in C/H plasmas could be responsible for the removal of B and BH. On the other hand, NH has a large nitrogen reservoir, N_2, to restore its concentration when removed, resulting in its invariant emission intensity under changes in diborane concentration. Introduction of methane to B/N/H plasmas caused predictable increases in carbon-related emission intensities, as well as increased N_2 intensity. As CH_4 increased, the NH emission became less intense due to formation of HCN and CN [114] and B and BH emissions increased before reaching a plateau. The work of Ma et al. [69, 172] showed a similar increase of B-related emissions, while Rond et al. [167] find a decrease when increasing methane. This discrepancy is explicable with reference to interactions of boron containing species with impurities (oxygen for Ma et al. and nitrogen here) or lack thereof (for Rond et al.). Changes in concentration of nitrogen and diborane in the plasma served mainly to confirm that reactions between N-containing and C-containing species reduce the influence of nitrogen on boron-containing species.

Diamond was grown by MP-CVD on silicon, polycrystalline diamond and single crystal diamond substrates. Additionally, silicon was used at two different temperatures denoted cold and hot. Nitrogen, low-level boron and high-level boron doped control samples were produced for comparison to low-boron+nitrogen and high-boron+nitrogen samples. In general the presence of boron gave low growth rate; caused (111) facetting of the surface at low concentration and less well-defined facets at high concentration; reduced sp^2 signals in the Raman spectra; incorporated boron in SIMS data; low resistivities and activation energies and inexplicably significant thermionic current (for one sample). Nitrogen doped films showed fast growth rate; temperature dependent morphology;

prominent sp^2 Raman character; incorporated nitrogen at concentrations above the limit dictated by detection of $C_2H_2^-$; high resistivity as well as high charge carrier activation energy, but not as high at found by previous research, and moderate thermionic emission current. Co-introduction of nitrogen and diborane offered increases in growth rate above that of low boron doping, but not when the higher boron concentration was present in the growth process gas; altered morphology in each case when B-N co-doped samples are compared to either B or N doped films; Raman spectra that show sp^2 character somewhere between that of B and N doped films; inconsistent changes in incorporated boron and nitrogen concentrations with respect to control samples; resistivities in general between that of the B and N doped controls, with activation energies comparable to the boron acceptor and in the single crystal case perhaps implying fewer active carriers; huge thermionic emission current when high boron was introduced with nitrogen, but negligible current with low boron and nitrogen. Many of these results require further measurements and repeat samples before more robust conclusions can be drawn.

6.2 Future work

Priority directions for iterative progression of this work are detailed in the concluding paragraphs of each results chapter. Nevertheless, there are some comments worth making about co-doping more generally.

Co-introducing a donor defect with an acceptor defect in diamond will produce a compensated semiconductor material. Consequently, little can be gained by simply dispersing the two impurities at random within the bulk. In order to harness the potential of any combination of dopants, the long-term future of experimental co-doping must aim towards overcoming the kinetic barrier to formation of clusters. HPHT treatment is the clear method of choice for this end, since dopants are known to be mobile at the necessary elevated temperatures and the extreme pressure stabilises the diamond phase. Unfortunately, HPHT processing is expensive, requiring a lot of time and consumables to carry out. Low pressure high temperature (LPHT) treatment [195] may be a cheap and simple alternative since it can be performed in a MP-CVD reactor, but large high quality single crystals would be required in order to slow the formation of graphite and loss of material through etching. Collaboration with a diamond research group with an interest in both HPHT and semiconducting diamond might be fruitful, but such groups may be rare.

The approach used here to examine the combination of two dopants might be used in

the future for different elements. Preliminary work for Li-N and Mg-N has been carried out computationally by Drs M. Zamir Othman and Sarah Halliwell, but a complete study of these pairs has not yet been made. Other combinations of dopants, as discussed in chapter 3, have been examined, but most only by the theoretical study of one specific cluster. The introduction of multiple dopants to MP-CVD plasmas is rare, but various combinations of elements could foreseeably benefit from careful study of both the plasma and resulting material. Such pairs might include N-P, B-P, Li-N, Be-N, Al-N and likely many more.

[1] M. W. Chase Jr., "Tables, NIST-JANAF thermochemical," *Journal of Physical and Chemical Reference Data*, p. 1952, 1998.

[2] M. H. Matus and D. J. Grant, "Fundamental thermochemical properties of ammonia borane and dehydrogenated derivatives (BNH_n, $n = 0-6$)," *The Journal of Physical Chemistry C*, vol. 113, no. 37, p. 16553, 2009.

[3] D. Huang and M. Frenklach, "Energetics of surface reactions on (100) diamond plane," *The Journal of Physical Chemistry*, vol. 96, no. 4, p. 1868, 1992.

[4] C. Handapangoda, S. Nahavandi, and M. Premaratne, "Review of nanoscale spectroscopy in medicine," in *Nanoscale Spectroscopy with Applications* (S. M. Musa, ed.), pp. 439–472, CRC Press, 11 2013.

[5] J. Filik, "Raman spectroscopy: a simple, non-destructive way to characterise diamond and diamond-like materials," *Spectroscopy Europe*, vol. 17, no. 5, p. 10, 2005.

[6] A. Croot, G. Wan, A. Rowan, J. Smith, H. Dominguez-Andrade, and N. A. Fox, "Beta radiation enhanced thermionic emission from diamond thin films," *Frontiers in Mechanical Engineering*, vol. 3, p. 17, 2017.

[7] P. J. Heard, K. A. Feeney, G. C. Allen, and P. R. Shewry, "Determination of the elemental composition of mature wheat grain using a modified secondary ion mass spectrometer (SIMS)," *The Plant Journal*, vol. 30, no. 2, p. 237, 2002.

[8] I. Aleksandrov, A. Goncharov, A. Zisman, and S. Stishov, "Diamond at high pressures: Raman scattering of light, equation of state, and high pressure scale," *Zh. eksp. teor. Fiz*, vol. 93, p. 680, 1987.

[9] P. W. May, "CVD diamond: a new technology for the future?," *Endeavour*, vol. 19, no. 3, p. 101, 1995.

[10] K. E. Spear and J. P. Dismukes, *Synthetic diamond: emerging CVD science and technology*, vol. 25.
John Wiley & Sons, 1994.

[11] C. Artini, M. Muolo, and A. Passerone, "Diamond–metal interfaces in cutting tools: a review," *Journal of Materials Science*, vol. 47, no. 7, p. 3252, 2012.

[12] P. Bergonzo, D. Tromson, C. Mer, B. Guizard, F. Foulon, and A. Brambilla, "Particle and radiation detectors based on diamond," *Physica Status Solidi A*, vol. 185, no. 1, p. 167, 2001.

[13] L. Švorc, M. Rievaj, and D. Bustin, "Green electrochemical sensor for environmental monitoring of pesticides: Determination of atrazine in river waters using a boron-doped diamond electrode," *Sensors and Actuators B: Chemical*, vol. 181, p. 294, 2013.

[14] F. P. Bundy, "The P, T phase and reaction diagram for elemental carbon, 1979," *Journal of Geophysical Research: Solid Earth*, vol. 85, no. B12, p. 6930, 1980.

[15] F. Bundy, H. T. Hall, H. Strong, and R. W. Jun, "Man-made diamonds," *Nature*, vol. 176, no. 4471, p. 51, 1955.

[16] H. Bovenkerk, F. Bundy, H. Hall, H. Strong, and R. H. Wentorf jun., "Preparation of diamond," *Nature*, vol. 184, no. 4693, p. 1094, 1959.

[17] I. Kiflawi, H. Kanda, and S. Lawson, "The effect of the growth rate on the concentration of nitrogen and transition metal impurities in HPHT synthetic diamonds," *Diamond and Related Materials*, vol. 11, no. 2, p. 204, 2002.

[18] D. Fisher and S. C. Lawson, "The effect of nickel and cobalt on the aggregation of nitrogen in diamond," *Diamond and Related Materials*, vol. 7, no. 2-5, p. 299, 1998.

[19] A. T. Collins and M. Stanley, "Absorption and luminescence studies of synthetic diamond in which the nitrogen has been aggregated," *Journal of Physics D: Applied Physics*, vol. 18, no. 12, p. 2537, 1985.

[20] W. G. Eversole, "Synthesis of diamond," Apr. 17 1962.
US Patent 3,030,188.

[21] F. G. Celii and J. E. Butler, "Diamond chemical vapor deposition," *Annual Review of Physical Chemistry*, vol. 42, no. 1, p. 643, 1991.

[22] C. Kanai, K. Watanabe, and Y. Takakuwa, "*Ab initio* calculations on etching of graphite and diamond surfaces by atomic hydrogen," *Physical Review B*, vol. 63, no. 23, p. 235311, 2001.

[23] C. J. Wort and R. S. Balmer, "Diamond as an electronic material," *Materials Today*, vol. 11, no. 1-2, p. 22, 2008.

[24] Y. V. Pleskov, "Electrochemistry of diamond: A review," *Russian Journal of Electrochemistry*, vol. 38, no. 12, p. 1275, 2002.

[25] S. J. Cobb, Z. J. Ayres, and J. V. Macpherson, "Boron doped diamond: A designer electrode material for the twenty-first century," *Annual Review of Analytical Chemistry*, vol. 11, pp. 20.1–20.22, 2018.

[26] V. Bormashov, S. Troschiev, A. Volkov, S. Tarelkin, E. Korostylev, A. Golovanov, M. Kuznetsov, D. Teteruk, N. Kornilov, S. Terentiev, S. Buga, and V. Blank, "Development of nuclear microbattery prototype based on Schottky barrier diamond diodes," *Physica Status Solidi A*, vol. 212, no. 11, p. 2539, 2015.

[27] J. Zhang, H. Ma, Y. Jiang, Z. Liang, Y. Tian, and X. Jia, "Effects of the additive boron on diamond crystals synthesized in the system of Fe-based alloy and carbon at HPHT," *Diamond and Related Materials*, vol. 16, no. 2, p. 283, 2007.

[28] N. Fujimori, H. Nakahata, and T. Imai, "Properties of boron-doped epitaxial diamond films," *Japanese Journal of Applied Physics*, vol. 29, no. 5R, p. 824, 1990.

[29] J. F. Prins, "Activation of boron-dopant atoms in ion-implanted diamonds," *Physical Review B*, vol. 38, no. 8, p. 5576, 1988.

[30] G. L. Pearson and J. Bardeen, "Electrical properties of pure silicon and silicon alloys containing boron and phosphorus," *Physical Review*, vol. 75, no. 5, p. 865, 1949.

[31] E. Ekimov, V. Sidorov, E. Bauer, N. Mel'Nik, N. Curro, J. Thompson, and S. Stishov, "Superconductivity in diamond," *Nature*, vol. 428, no. 6982, p. 542, 2004.

[32] R. Farrer, "On the substitutional nitrogen donor in diamond," *Solid State Communications*, vol. 7, no. 9, p. 685, 1969.

[33] J. Mort, M. A. Machonkin, and K. Okumura, "Compensation effects in nitrogen-doped diamond thin films," *Applied Physics Letters*, vol. 59, no. 24, p. 3148, 1991.

[34] Y. Zhang, C. Zang, H. Ma, Z. Liang, L. Zhou, S. Li, and X. Jia, "HPHT synthesis of large single crystal diamond doped with high nitrogen concentration," *Diamond and Related Materials*, vol. 17, no. 2, p. 209, 2008.

[35] S. J. Charles, J. E. Butler, B. N. Feygelson, M. E. Newton, D. L. Carroll, J. W. Steeds, H. Darwish, C. Yan, H. K. Mao, and R. J. Hemley, "Characterization of nitrogen doped chemical vapor deposited single crystal diamond before and after high pressure, high temperature annealing," *Physica Status Solidi A*, vol. 2485, no. 11, p. 2473, 2004.

[36] C. Bradac, T. Gaebel, and J. R. Rabeau, "Nitrogen-vacancy color centers in diamond: Properties, synthesis, and applications," in *Optical Engineering of Diamond* (P. Mildren and J. R. Rabeau, eds.), ch. 5, pp. 143–175, Wiley, 2013.

[37] J. van der Weide, Z. Zhang, P. Baumann, M. Wensell, J. Bernholc, and R. Nemanich, "Negative-electron-affinity effects on the diamond (100) surface," *Physical Review B*, vol. 50, no. 8, p. 5803, 1994.

[38] S. Meir, C. Stephanos, T. H. Geballe, and J. Mannhart, "Highly-efficient thermo-electronic conversion of solar energy and heat into electric power," *Journal of Renewable and Sustainable Energy*, vol. 5, no. 4, p. 043127, 2013.

[39] F. A. M. Koeck, J. M. Garguilo, and R. J. Nemanich, "On the thermionic emission from nitrogen-doped diamond films with respect to energy conversion," *Diamond and Related Materials*, vol. 13, no. 11-12, p. 2052, 2004.

[40] F. A. M. Koeck, R. J. Nemanich, A. Lazea, and K. Haenen, "Thermionic electron emission from low work-function phosphorus doped diamond films," *Diamond and Related Materials*, vol. 18, no. 5-8, p. 789, 2009.

[41] E. Gheeraert, S. Koizumi, T. Teraji, and H. Kanda, "Electronic transitions of electrons bound to phosphorus donors in diamond," *Solid State Communications*, vol. 113, no. 10, p. 577, 2000.

[42] P. W. May, M. Davey, K. N. Rosser, and P. J. Heard, "Arsenic and antimony doping: an attempt to deposit n-type CVD diamond," *MRS Online Proceedings Library Archive*, vol. 1039, 2007.

[43] J. F. Prins, "n-type semiconducting diamond by means of oxygen-ion implantation," *Physical Review B*, vol. 61, no. 11, p. 7191, 2000.

[44] A. S. Barnard, S. P. Russo, and I. K. Snook, "*Ab initio* modelling of band states in doped diamond," *Philosophical Magazine*, vol. 83, no. 9, p. 1163, 2003.

[45] R. Kalish, A. Reznik, C. Uzan-Saguy, and C. Cytermann, "Is sulfur a donor in diamond?," *Applied Physics Letters*, vol. 76, no. 6, p. 757, 2000.

[46] S. Kajihara, A. Antonelli, J. Bernholc, and R. Car, "Nitrogen and potential n-type dopants in diamond," *Physical Review Letters*, vol. 66, no. 15, p. 2010, 1991.

[47] M. Restle, K. Bharuth-Ram, H. Quintel, C. Ronning, H. Hofsass, S. G. Jahn, and U. Wahl, "Lattice sites of ion implanted Li in diamond," *Applied Physics Letters*, vol. 66, no. 20, pp. 2733–2735, 1995.

[48] J. Te Nijenhuis, G. Cao, P. Smits, W. Van Enckevort, L. Giling, P. Alkemade, M. Nesládek, and Z. Remeš, "Incorporation of lithium in single crystal diamond: diffusion profiles and optical and electrical properties," *Diamond and Related Materials*, vol. 6, no. 11, p. 1726, 1997.

[49] H. Katayama-Yoshida, T. Nishimatsu, T. Yamamoto, and N. Orita, "Comparison between the theoretical prediction of codoping and the recent experimental evidences in p-type GaN, AlN, ZnSe, $CuInS_2$ and n-type diamond," *Physica Status Solidi B*, vol. 210, no. 429, p. 429, 1998.

[50] B. D. Yu, Y. Miyamoto, and O. Sugino, "Efficient n-type doping of diamond using surfactant-mediated epitaxial growth," *Applied Physics Letters*, vol. 76, no. 8, p. 976, 2000.

[51] T. Miyazaki, H. Okushi, and T. Uda, "Shallow donor state due to nitrogen-hydrogen complex in diamond," *Physical Review Letters*, vol. 88, no. 6, p. 66402/1, 2002.

[52] D. Segev and S.-H. Wei, "Design of shallow donor levels in diamond by isovalent-donor coupling.," *Physical Review Letters*, vol. 91, no. 12, p. 126406, 2003.

108

[53] J. E. Moussa, N. Marom, N. Sai, and J. R. Chelikowsky, "Theoretical design of a shallow donor in diamond by lithium-nitrogen codoping," *Physical Review Letters*, vol. 108, p. 226404, 2012.

[54] S. C. Halliwell, *Characterisation of co-doped CVD diamond for potential thermionic applications*.
PhD thesis, University of Bristol, 2017.

[55] R. J. Eyre, J. P. Goss, P. R. Briddon, and M. G. Wardle, "Multi-impurity complexes for n-type diamond: A computational study," *Physica Status Solidi A*, vol. 204, no. 9, p. 2971, 2007.

[56] R. Zeisel, C. Nebel, M. Stutzmann, H. Sternschulte, M. Schreck, and B. Stritzker, "Photoconductivity study of Li doped homoepitaxially grown CVD diamond," *Physica Status Solidi A*, vol. 181, no. 1, p. 45, 2000.

[57] W. Lee, J. Yu, and T. Lee, "Study on the Li and B co-doped diamond thin film," *Journal of Materials Science*, vol. 40, no. 20, p. 5549, 2005.

[58] S. C. Halliwell, P. W. May, N. A. Fox, and M. Z. Othman, "Investigations of the co-doping of boron and lithium into CVD diamond thin films," *Diamond and Related Materials*, vol. 76, p. 115, 2017.

[59] M. Z. Othman, P. W. May, N. A. Fox, and P. J. Heard, "Incorporation of lithium and nitrogen into CVD diamond thin films," *Diamond and Related Materials*, vol. 44, p. 1, 2014.

[60] S. C. Eaton, A. B. Anderson, J. C. Angus, Y. E. Evstefeeva, and Y. V. Pleskov, "Diamond growth in the presence of boron and sulfur," *Diamond and Related Materials*, vol. 12, no. 10-11, p. 1627, 2003.

[61] R. Li, X. Hu, H. Shen, and X. He, "Co-doping of sulfur and boron in CVD-diamond," *Materials Letters*, vol. 58, no. 12-13, p. 1835, 2004.

[62] X. J. Hu, R. B. Li, H. S. Shen, Y. Dai, and X. He, "Electrical and structural properties of boron and phosphorus co-doped diamond films," *Carbon*, vol. 42, p. 1501, 2004.

[63] G. Cao, L. Giling, and P. Alkemade, "Growth of phosphorus and nitrogen co-doped diamond films," *Diamond and Related Materials*, vol. 4, no. 5-6, p. 775, 1995.

[64] G. Cao, F. Driessen, G. Bauhuis, L. Giling, and P. Alkemade, "Homoepitaxial diamond films codoped with phosphorus and nitrogen by chemical-vapor deposition," *Journal of Applied Physics*, vol. 78, no. 5, p. 3125, 1995.

[65] Z. Teukam, J. Chevallier, C. Saguy, R. Kalish, D. Ballutaud, M. Barbé, F. Jomard, A. Tromson-Carli, C. Cytermann, J. E. Butler, M. Bernard, C. Baron, and A. Deneuville, "Shallow donors with high n-type electrical conductivity in homoepitaxial deuterated boron-doped diamond layers.," *Nature materials*, vol. 2, no. July, p. 482, 2003.

[66] C. Saguy, "Diffusion of Light Elements in Diamond," *Defect and Diffusion Forum*, vol. 226-228, p. 31, 2004.

[67] Y. Liou, A. Inspektor, R. Weimer, D. Knight, and R. Messier, "The effect of oxygen in diamond deposition by microwave plasma enhanced chemical vapor deposition," *Journal of Materials Research*, vol. 5, no. 11, p. 2305, 1990.

[68] A. Inspektor, Y. Liou, T. McKenna, and R. Messier, "Plasma CVD diamond deposition in C-H-O systems," *Surface and Coatings Technology*, vol. 39, p. 211, 1989.

[69] J. Ma, M. N. R. Ashfold, and Y. A. Mankelevich, "Validating optical emission spectroscopy as a diagnostic of microwave activated $CH_4/Ar/H_2$ plasmas used for diamond chemical vapor deposition," *Journal of Applied Physics*, vol. 105, no. 4, p. 1, 2009.

[70] R. Locher, J. Wagner, F. Fuchs, C. Wild, P. Hiesinger, P. Gonon, and P. Koidl, "Boron doped diamond films: electrical and optical characterization and the effect of compensating nitrogen," *Materials Science & Engineering B*, vol. 29, p. 211, 1995.

[71] S. Sonoda, J. H. Won, H. Yagi, A. Hatta, T. Ito, and A. Hiraki, "Effect of nitrogen incorporation on electrical properties of boron-doped diamond films," *Applied Physics Letters*, vol. 70, no. 19, p. 2574, 1997.

[72] V. I. Polyakov, A. I. Rukovishnikov, N. M. Rossukanyi, and V. G. Ralchenko, "Electrical properties of thick boron and nitrogen contained CVD diamond films," *Diamond and Related Materials*, vol. 10, no. 3-7, p. 593, 2001.

[73] J. A. Freitas, P. B. Klein, and A. T. Collins, "Evidence of donor-acceptor pair recombination from a new emission band in semiconducting diamond," *Applied Physics Letters*, vol. 64, no. 16, p. 2136, 1994.

[74] J. A. Freitas, K. Doverspike, P. B. Klein, Y. L. Khong, and A. T. Collins, "Luminescence studies of nitrogen- and boron-doped diamond films," *Diamond and Related Materials*, vol. 3, no. 4-6, p. 821, 1994.

[75] J. Isoya, H. Kanda, and Y. Morita, "EPR identification of the ⟨100⟩-split [B-N]+ interstitialcy in diamond," *Physical Review B*, vol. 56, no. 11, p. 6392, 1997.

[76] N. Ishii and T. Shimizu, "Cluster-model calculation of hyperfine parameters for the ⟨100⟩-split [B-N]+ interstitial in diamond," *Physical Review B*, vol. 58, no. 19, p. 12533, 1998.

[77] X. J. Hu, Y. B. Dai, H. S. Shen, and X. C. He, "A molecular dynamics simulation on the structural properties of B and N co-existed in diamond," *Physica B: Condensed Matter*, vol. 367, no. 1-4, p. 86, 2005.

[78] S. Sun, X. Jia, Z. Zhang, Y. Li, B. Yan, X. Liu, and H.-a. Ma, "HPHT synthesis of boron and nitrogen co-doped strip-shaped diamond using powder catalyst with additive h-BN," *Journal of Crystal Growth*, vol. 377, p. 22, 2013.

[79] I. Yagi, K. Tsunozaki, A. Fujishima, B. Ohtani, and K. Uosaki, "The effects of nitrogen and plasma power on electrochemical properties of boron-doped diamond electrodes grown by MPCVD," *Journal of the Electrochemical Society*, vol. 149, no. 1, p. E1, 2002.

[80] L. L. G. Silva, V. J. Trava-Airoldi, E. J. Corat, N. Added, and P. T. A. Sumodjo, "Detection of N and B in doped diamond films by ERDA method and related electrochemical characteristics," *Diamond and Related Materials*, vol. 16, no. 1, p. 174, 2007.

[81] Q. Liang, C.-s. Yan, Y. Meng, and J. Lai, "Enhancing the mechanical properties of single-crystal CVD diamond," *Journal of Physics: Condensed Matter*, vol. 21, p. 364215, 2009.

[82] P. Hartmann, R. Haubner, and B. Lux, "Effects of simultaneous boron and nitrogen addition on hot-filament CVD diamond growth," *Diamond & Related Materials*, vol. 6, p. 456, 1997.

[83] A. F. Sartori, M. Fischer, S. Gsell, and M. Schreck, "In-situ boron doping during heteroepitaxial growth of diamond on Ir/YSZ/Si," *Physica Status Solidi A*, vol. 209, no. 9, p. 1643, 2012.

[84] A. F. Sartori and M. Schreck, "Mutual interaction of N, B, and O during heteroepitaxial diamond growth : Triggering the nitrogen induced growth acceleration," *Physica Status Solidi A*, vol. 211, no. 10, p. 2290, 2014.

[85] S. Dunst, H. Sternschulte, and M. Schreck, "Growth rate enhancement by nitrogen in diamond chemical vapor deposition-a catalytic effect," *Applied Physics Letters*, vol. 94, p. 224101, 2009.

[86] Z. Yiming, F. Larsson, and K. Larsson, "Effect of CVD diamond growth by doping with nitrogen," *Theoretical Chemistry Accounts*, vol. 133, no. 2, p. 1432, 2014.

[87] A. Szabo and N. S. Ostlund, *Modern quantum chemistry: introduction to advanced electronic structure theory*.
Courier Corporation, 2012.

[88] E. J. Baerends, D. E. Ellis, and P. Ros, "Self-consistent molecular Hartree-Fock-Slater calculations I. The computational procedure," *Chemical Physics*, vol. 2, no. 1, p. 41, 1973.

[89] J. C. Slater, "A simplification of the Hartree-Fock method," *Physical Review*, vol. 81, no. 3, p. 385, 1951.

[90] J. C. Slater and J. H. Wood, "Statistical exchange and the total energy of a crystal," *International Journal of Quantum Chemistry*, vol. 5, no. 4 S, p. 3, 1970.

[91] R. M. Martin, *Electronic structure: basic theory and practical methods*.
Cambridge University Press, 2004.

[92] P. Hohenberg and W. Kohn, "Inhomogeneous electron gas," *Physical Review*, vol. 136, no. 3B, p. B864, 1964.

[93] W. Kohn and L. J. Sham, "Self-consistent equations including exchange and correlation effects," *Physical Review*, vol. 140, no. 4A, p. A1133, 1965.

[94] P. Geerlings, F. De Proft, and W. Langenaeker, "Conceptual density functional theory," *Chemical Reviews*, vol. 103, no. 5, p. 1793, 2003.

[95] D. C. Langreth and M. Mehl, "Beyond the local-density approximation in calculations of ground-state electronic properties," *Physical Review B*, vol. 28, no. 4, p. 1809, 1983.

[96] D. C. Langreth and M. Mehl, "Easily implementable nonlocal exchange-correlation energy functional," *Physical Review Letters*, vol. 47, no. 6, p. 446, 1981.

[97] J. P. Perdew and Y. Wang, "Accurate and simple analytic representation of the electron-gas correlation energy," *Physical Review B*, vol. 45, no. 23, p. 13244, 1992.

[98] J. P. Perdew, K. Burke, and M. Ernzerhof, "Generalized gradient approximation made simple," *Physical Review Letters*, vol. 77, no. 18, p. 3865, 1996.

[99] Z. Wu and R. E. Cohen, "More accurate generalized gradient approximation for solids," *Physical Review B*, vol. 73, no. 23, p. 235116, 2006.

[100] J. P. Perdew and M. Levy, "Physical content of the exact Kohn-Sham orbital energies: band gaps and derivative discontinuities," *Physical Review Letters*, vol. 51, no. 20, p. 1884, 1983.

[101] A. D. Becke, "A new mixing of Hartree–Fock and local density-functional theories," *The Journal of Chemical Physics*, vol. 98, no. 2, p. 1372, 1993.

[102] J. Heyd, J. E. Peralta, G. E. Scuseria, and R. L. Martin, "Energy band gaps and lattice parameters evaluated with the Heyd-Scuseria-Ernzerhof screened hybrid functional," *The Journal of Chemical Physics*, vol. 123, no. 17, p. 174101, 2005.

[103] J. Heyd, G. E. Scuseria, and M. Ernzerhof, "Hybrid functionals based on a screened Coulomb potential," *The Journal of Chemical Physics*, vol. 118, no. 18, p. 8207, 2003.

[104] J. Paier, M. Marsman, K. Hummer, G. Kresse, I. C. Gerber, and J. G. Ángyán, "Screened hybrid density functionals applied to solids," *The Journal of Chemical Physics*, vol. 124, no. 15, p. 154709, 2006.

[105] J. Paier, R. Hirschl, M. Marsman, and G. Kresse, "The Perdew–Burke–Ernzerhof exchange-correlation functional applied to the G2-1 test set using a plane-wave basis set," *The Journal of Chemical Physics*, vol. 122, no. 23, p. 234102, 2005.

[106] D. Vanderbilt, "Soft self-consistent pseudopotentials in a generalized eigenvalue formalism," *Physical Review B*, vol. 41, no. 11, p. 7892, 1990.

[107] H. J. Monkhorst and J. D. Pack, "Special points for Brillouin-zone integrations," *Physical Review B*, vol. 13, no. 12, p. 5188, 1976.

[108] M. Frenklach, "The role of hydrogen in vapor deposition of diamond," *Journal of Applied Physics*, vol. 65, no. 12, p. 5142, 1989.

[109] S. J. Harris and L. R. Martin, "Methyl versus acetylene as diamond growth species," *Journal of Materials Research*, vol. 5, p. 2313, 1990.

[110] Y. A. Mankelevich and P. W. May, "New insights into the mechanism of CVD diamond growth: Single crystal diamond in MW PECVD reactors," *Diamond and Related Materials*, vol. 17, no. 7-10, p. 1021, 2008.

[111] S. J. Harris, "Mechanism for diamond growth from methyl radicals," *Applied Physics Letters*, vol. 56, no. 23, p. 2298, 1990.

[112] S. J. Harris and D. G. Goodwin, "Growth on the reconstructed diamond (100) surface," *Journal of Physical Chemistry*, vol. 97, p. 23, 1993.

[113] J. Achard, F. Silva, O. Brinza, A. Tallaire, and A. Gicquel, "Coupled effect of nitrogen addition and surface temperature on the morphology and the kinetics of thick CVD diamond single crystals," *Diamond and Related Materials*, vol. 16, no. 4-7, p. 685, 2007.

[114] B. S. Truscott, M. W. Kelly, K. J. Potter, M. N. R. Ashfold, and Y. A. Mankelevich, "Microwave plasma-activated chemical vapor deposition of nitrogen-doped diamond. II: $CH_4/N_2/H_2$ plasmas," *Journal of Physical Chemistry A*, vol. 120, no. 43, p. 8537, 2016.

[115] R. Locher, C. Wild, N. Herres, D. Behr, and P. Koidl, "Nitrogen stabilized ⟨100⟩ texture in chemical vapor deposited diamond films," *Applied Physics Letters*, vol. 65, no. 1, p. 34, 1994.

[116] P. Hartmann, S. Bohr, R. Haubner, B. Lux, P. Wurzinger, M. Griesser, A. Bergmaier, G. Dollinger, H. Sternschulte, and R. Sauer, "Diamond growth with boron addition," *International Journal of Refractory Metals and Hard Materials*, vol. 16, no. 3, p. 223, 1998.

[117] P. Gonon, E. Gheeraert, A. Deneuville, L. Abello, and G. Lucazeau, "Effect of boron incorporation on the "quality" of MPCVD diamond films," *Diamond and Related Materials*, vol. 2, no. 5, p. 742, 1993.

[118] J. Achard, F. Silva, R. Issaoui, O. Brinza, A. Tallaire, H. Schneider, K. Isoird, H. Ding, S. Koné, M. A. Pinault, F. Jomard, and A. Gicquel, "Thick boron doped diamond single crystals for high power electronics," *Diamond and Related Materials*, vol. 20, no. 2, p. 145, 2011.

[119] K. Iakoubovskii, G. J. Adriaenssens, and Y. K. Vohra, "Nitrogen incorporation in CVD diamond," *Diamond and Related Materials*, vol. 10, no. 3-7, p. 485, 2001.

[120] F. Roux, F. Michaud, and M. Vervloet, "High-resolution fourier spectrometry of $14N_2$ violet emission spectrum: extensive analysis of the $C^3\Pi_u$-$B^3\Pi_g$ system," *Journal of Molecular Spectroscopy*, vol. 158, no. 2, p. 270, 1993.

[121] C. R. Brazier, R. S. Ram, and P. F. Bernath, "Fourier transform spectroscopy of the $A^3\Pi$-$X^3\Sigma^-$ transition of NH," *Journal of Molecular Spectroscopy*, vol. 120, no. 2, p. 381, 1986.

[122] W. T. M. L. Fernando and P. F. Bernath, "Fourier transform spectroscopy of the $A^1\Pi$-$X^1\Sigma^+$ transition of BH and BD," *Journal of Molecular Spectroscopy*, vol. 145, no. 2, p. 392, 1991.

[123] M. Zachwieja, "New investigations of the $A^2\Delta$-$X^2\Pi$ band system in the CH radical and a new reduction of the vibration-rotation spectrum of CH from the ATMOS spectra," *Journal of Molecular Spectroscopy*, vol. 170, no. 2, p. 285, 1995.

[124] R. Ram, S. Davis, L. Wallace, R. Engleman, D. R. Appadoo, and P. Bernath, "Fourier transform emission spectroscopy of the $B^2\Sigma^+$–$X^2\Sigma^+$ system of CN," *Journal of Molecular Spectroscopy*, vol. 237, no. 2, p. 225, 2006.

[125] J. E. Butler, Y. A. Mankelevich, A. Cheesman, J. Ma, and M. N. R. Ashfold, "Understanding the chemical vapor deposition of diamond: recent progress," *Journal of Physics: Condensed Matter*, vol. 21, no. 36, p. 364201, 2009.

[126] C. M. Western, "Pgopher: A program for simulating rotational, vibrational and electronic spectra," *Journal of Quantitative Spectroscopy and Radiative Transfer*, vol. 186, p. 221, 2017.

115

[127] C. M. Western and B. E. Billinghurst, "Automatic assignment and fitting of spectra with pgopher," *Physical Chemistry Chemical Physics*, vol. 19, no. 16, p. 10222, 2017.

[128] J.-P. Lagrange, A. Deneuville, and E. Gheeraert, "Activation energy in low compensated homoepitaxial boron-doped diamond films," *Diamond and Related Materials*, vol. 7, no. 9, p. 1390, 1998.

[129] T. Borst and O. Weis, "Electrical characterization of homoepitaxial diamond films doped with B, P, Li and Na during crystal growth," *Diamond and Related Materials*, vol. 4, no. 7, p. 948, 1995.

[130] S. Dushman, "Thermionic emission," *Reviews of Modern Physics*, vol. 2, no. 4, p. 381, 1930.

[131] A. Modinos, *Field, thermionic and secondary electron emission spectroscopy*. Springer Science & Business Media, 2013.

[132] W. Paxton, M. Howell, W. Kang, and J. Davidson, "Influence of hydrogen on the thermionic electron emission from nitrogen-incorporated polycrystalline diamond films," *Journal of Vacuum Science & Technology B, Nanotechnology and Microelectronics: Materials, Processing, Measurement, and Phenomena*, vol. 30, no. 2, p. 021202, 2012.

[133] H. Katayama-Yoshida, T. Nishimatsu, T. Yamamoto, and N. Orita, "Codoping method for the fabrication of low-resistivity wide band-gap semiconductors in p-type GaN, p-type AlN and n-type diamond: prediction versus experiment," *Journal of Physics: Condensed Matter*, vol. 13, p. 8901, 2001.

[134] J. P. Goss, P. R. Briddon, and R. J. Eyre, "Donor levels for selected n-type dopants in diamond: A computational study of the effect of supercell size," *Physical Review B*, vol. 74, p. 245217, 2006.

[135] M. Z. Othman, S. J. Conejeros, A. Croot, K. M. O'Donnell, J. N. Hart, P. W. May, and N. L. Allan, "In preparation,"

[136] T. Evans, Z. Qi, and J. Maguire, "The stages of nitrogen aggregation in diamond," *Journal of Physics C: Solid State Physics*, vol. 14, p. L379, 1981.

[137] J. P. Goss, R. J. Eyre, and P. R. Briddon, "Theoretical models for doping diamond for semiconductor applications," *Physica Status Solidi B*, vol. 245, no. 9, p. 1679, 2008.

[138] W. Kaiser and W. L. Bond, "Nitrogen, a major impurity in common type I diamond," *Physical Review*, vol. 115, no. 4, p. 857, 1959.

[139] E. B. Lombardi, A. Mainwood, K. Osuch, and E. C. Reynhardt, "Computational models of the single substitutional nitrogen atom in diamond," *Journal of Physics: Condensed Matter*, vol. 15, p. 3135, 2003.

[140] R. Dovesi, R. Orlando, A. Erba, C. M. Zicovich-Wilson, B. Civalleri, S. Casassa, L. Maschio, M. Ferrabone, M. De la Pierre, P. D'Arco, Y. Noel, M. Causa, M. Rerat, and B. Kirtman, "CRYSTAL14: A program for the *ab initio* investigation of crystalline solids," *International Journal of Quantum Chemistry*, vol. 114, no. 19, p. 1287, 2014.

[141] J. Heyd, G. E. Scuseria, and M. Ernzerhof, "Hybrid functionals based on a screened Coulomb potential," *Journal of Chemical Physics*, vol. 118, no. 18, p. 8207, 2003.

[142] M. Catti, A. Pavese, R. Dovesi, and V. R. Saunders, "Static lattice and electron properties of $MgCO_3$ (magnesite) calculated by *ab initio* periodic Hartree-Fock methods," *Physical Review B*, vol. 47, no. 15, p. 9189, 1993.

[143] M. F. Peintinger, D. V. Oliveira, and T. Bredow, "Consistent Gaussian basis sets of triple-zeta valence with polarization quality for solid-state calculations," *Journal of Computational Chemistry*, vol. 34, no. 6, p. 451, 2013.

[144] B. G. Pfrommer, M. Cote, S. G. Louie, and M. L. Cohen, "Relaxation of crystals with the quasi-Newton method," *Journal of Computational Physics*, vol. 131, p. 233, 1997.

[145] D. A. Liberman, "Slater transition-state band-structure calculations," *Physical Review B*, vol. 62, no. 11, p. 6851, 2000.

[146] J. P. Goss, R. J. Eyre, and P. R. Briddon, "Bound substitutional impurity pairs in diamond: A density functional study," *Journal of Physics: Condensed Matter*, vol. 20, no. 8, p. 085217, 2008.

[147] S. Clark, M. Segall, C. Pickard, P. Hasnip, M. Probert, K. Refson, and M. Payne, "First principles methods using CASTEP," *Zeitschrift für Kristallographie - Crystalline Materials*, vol. 220, no. 5-6, p. 567, 2005.

[148] K. Czelej, P. Śpiewak, and K. J. Kurzydlowski, "Electronic structure of substitutionally doped diamond: Spin-polarized, hybrid density functional theory analysis," *Diamond and Related Materials*, vol. 75, p. 146, 2017.

[149] Simultaneous losses of multiple atoms are considered kinetically unlikely so are not considered here.

[150] R. MacLeod, S. Murray, J. Goss, P. Briddon, and R. Eyre, "Model thermodynamics and the role of free-carrier energy at high temperatures: Nitrogen and boron pairing in diamond," *Physical Review B*, vol. 80, no. 5, p. 1, 2009.

[151] P. A. Crowther, P. J. Dean, and W. F. Sherman, "Excitation spectrum of aluminum acceptors in diamond under uniaxial stress," *Physical Review*, vol. 154, no. 3, p. 772, 1967.

[152] J. P. Goss and P. R. Briddon, "Theoretical study of Li and Na as n-type dopants for diamond," *Physical Review B*, vol. 75, p. 075202, 2007.

[153] T. Miyazaki and H. Okushi, "A theoretical study of a sulfur impurity in diamond," *Diamond and Related Materials*, vol. 10, no. 3-7, p. 449, 2001.

[154] J. P. Goss, P. R. Briddon, R. Jones, and S. Sque, "Donor and acceptor states in diamond," *Diamond and Related Materials*, vol. 13, no. 4-8, p. 684, 2004.

[155] T. Vandevelde, M. Nesladek, C. Quaeyhaegens, and L. Stals, "Optical emission spectroscopy of the plasma during CVD diamond growth with nitrogen addition," *Thin Solid Films*, vol. 290-291, p. 143, 1996.

[156] A. Gicquel, K. Hassouni, S. Farhat, Y. Breton, C. D. Scott, M. Lefebvre, and M. Pealat, "Spectroscopic analysis and chemical kinetics modeling of a diamond deposition plasma reactor," *Diamond and Related Materials*, vol. 3, no. 4-6, p. 581, 1994.

[157] J. A. Smith, M. A. Cook, S. R. Langford, S. A. Redman, and M. N. R. Ashfold, "Resonance enhanced multiphoton ionization probing of H atoms and CH_3 radicals in a hot filament chemical vapour deposition reactor," *Thin Solid Films*, vol. 368, p. 169, 2000.

[158] J. Ma, J. C. Richley, M. N. Ashfold, and Y. A. Mankelevich, "Probing the plasma chemistry in a microwave reactor used for diamond chemical vapor deposition by cavity ring down spectroscopy," *Journal of Applied Physics*, vol. 104, no. 10, p. 103305, 2008.

[159] T. Vandevelde, M. Nesladek, C. Quaeyhaegens, and L. Stals, "Optical emission spectroscopy of the plasma during microwave CVD of diamond thin films with nitrogen addition and relation to the thin film morphology," *Thin Solid Films*, vol. 309, p. 154, 1997.

[160] T. Vandevelde, T. D. Wu, C. Quaeyhaegens, J. Vlekken, M. D'Olieslaeger, and L. Stals, "Correlation between the OES plasma composition and the diamond film properties during microwave PA-CVD with nitrogen addition," *Thin Solid Films*, vol. 340, no. 1, p. 159, 1999.

[161] A. Chayahara, Y. Mokuno, Y. Horino, Y. Takasu, H. Kato, H. Yoshikawa, and N. Fujimori, "The effect of nitrogen addition during high-rate homoepitaxial growth of diamond by microwave plasma CVD," *Diamond and Related Materials*, vol. 13, no. 11-12, p. 1954, 2004.

[162] A. Tallaire, A. T. Collins, D. Charles, J. Achard, R. Sussmann, and A. Gicquel, "Characterisation of high-quality thick single-crystal diamond grown by CVD with a low nitrogen addition," *Diamond and Related Materials*, vol. 15, p. 1700, 2006.

[163] Q. Liang, J. G. Harrison, and Y. K. Vohra, "Modeling of nitrogen/diborane/methane/hydrogen plasma for nanocrystalline diamond growth : Comparison with experimental data," *Diamond and Related Materials*, vol. 17, no. 12, p. 2067, 2008.

[164] M. Rayar, P. Supiot, P. Veis, and A. Gicquel, "Optical emission study of a doped diamond deposition process by plasma enhanced chemical vapor deposition," *Journal of Applied Physics*, vol. 104, p. 033304, 2008.

[165] J. Ma, J. C. Richley, D. R. W. Davies, M. N. R. Ashfold, and Y. A. Mankelevich, "Spectroscopic and modeling investigations of the gas phase chemistry and composition in microwave plasma activated $B_2H_6/CH_4/Ar/H_2$ mixtures," *Journal of Physical Chemistry A*, vol. 114, no. 37, p. 10076, 2010.

[166] J. Ma, J. C. Richley, D. R. W. Davies, M. N. R. Ashfold, and Y. A. Mankelevich, "Spectroscopic and modeling investigations of the gas-phase chemistry and composition in microwave plasma activated $B_2H_6/Ar/H_2$ mixtures," *Journal of Physical Chemistry A*, vol. 114, no. 7, pp. 2447–2463, 2010.

[167] C. Rond, R. Salem, S. Hamann, G. Lombardi, J. Röpcke, and A. Gicquel, "Chemical analysis of H_2–B_2H_6 and H_2–CH_4–B_2H_6 microwave CVD plasmas used for diamond deposition," *Plasma Sources Science and Technology*, vol. 25, no. 2, p. 025016, 2016.

[168] B. S. Truscott, M. W. Kelly, K. J. Potter, M. Johnson, M. N. R. Ashfold, and Y. A. Mankelevich, "Microwave plasma-activated chemical vapor deposition of nitrogen-doped diamond. I. N_2/H_2 and NH_3/H_2 plasmas," *Journal of Physical Chemistry A*, vol. 119, no. 52, p. 12962, 2015.

[169] D. Franz, M. Hollenstein, and C. Hollenstein, "Diborane nitrogen/ammonia plasma chemistry investigated by infrared absorption spectroscopy," *Thin Solid Films*, vol. 379, p. 37, 2000.

[170] S. Hamann, C. Rond, A. V. Pipa, M. Wartel, G. Lombardi, A. Gicquel, and J. Ropcke, "Spectroscopic study of H_2 microwave plasmas with small admixtures of CH_4 and B_2H_6 used for doped diamond deposition," *Plasma Sources Science and Technology*, vol. 23, p. 045015, 14.

[171] H. Yamada, "Numerical simulations to study growth of single-crystal diamond by using microwave plasma chemical vapor deposition with reactive (H, C, N) species," *Japanese Journal of Applied Physics*, vol. 51, no. 9R, p. 090105, 2012.

[172] J. Ma, A. Cheesman, M. N. R. Ashfold, K. G. Hay, S. Wright, N. Langford, G. Duxbury, and Y. A. Mankelevich, "Quantum cascade laser investigations of CH_4 and C_2H_2 interconversion in hydrocarbon/H_2 gas mixtures during microwave plasma enhanced chemical vapor deposition of diamond," *Journal of Applied Physics*, vol. 106, no. 3, p. 033305, 2009.

[173] C. Moore, "National standard reference data series," *US Natl Bur Stand, NSRDS-NBS*, vol. 35, 1971.

[174] R. Wentorf Jr, "Cubic form of boron nitride," *The Journal of Chemical Physics*, vol. 26, no. 4, p. 956, 1957.

[175] S. Matsumoto, Y. Sato, M. Tsutsumi, and N. Setaka, "Growth of diamond particles from methane-hydrogen gas," *Journal of Materials Science*, vol. 17, no. 11, p. 3106, 1982.

[176] J. Birrell, J. Carlisle, O. Auciello, D. Gruen, and J. Gibson, "Morphology and electronic structure in nitrogen-doped ultrananocrystalline diamond," *Applied Physics Letters*, vol. 81, no. 12, p. 2235, 2002.

[177] R. Samlenski, C. Haug, R. Brenn, C. Wild, R. Locher, and P. Koidl, "Incorporation of nitrogen in chemical vapor deposition diamond," *Applied Physics Letters*, vol. 67, no. 19, p. 2798, 1995.

[178] R. Samlenski, C. Haug, R. Brenn, C. Wild, R. Locher, and P. Koidl, "Characterisation and lattice location of nitrogen and boron in homoepitaxial CVD diamond," *Diamond and Related Materials*, vol. 5, no. 9, p. 947, 1996.

[179] C. Wild, N. Herres, and P. Koidl, "Texture formation in polycrystalline diamond films," *Journal of Applied Physics*, vol. 68, no. 3, p. 973, 1990.

[180] A. C. Ferrari and J. Robertson, "Origin of the 1150 cm^{-1} Raman mode in nanocrystalline diamond," *Physical Review B*, vol. 63, no. 12, p. 121405, 2001.

[181] S. Prawer and R. J. Nemanich, "Raman spectroscopy of diamond and doped diamond," *Philosophical Transactions of the Royal Society of London A*, vol. 362, no. 1824, p. 2537, 2004.

[182] J. Wagner, C. Wild, and P. Koidl, "Resonance effects in Raman scattering from polycrystalline diamond films," *Applied Physics Letters*, vol. 59, no. 7, p. 779, 1991.

[183] K. Ushizawa, K. Watanabe, T. Ando, I. Sakaguchi, M. Nishitani-Gamo, Y. Sato, and H. Kanda, "Boron concentration dependence of Raman spectra on {100} and {111} facets of B-doped CVD diamond," *Diamond and Related Materials*, vol. 7, no. 11-12, p. 1719, 1998.

[184] P. May, W. Ludlow, M. Hannaway, P. Heard, J. Smith, and K. Rosser, "Raman and conductivity studies of boron-doped microcrystalline diamond, facetted nanocrystalline diamond and cauliflower diamond films," *Diamond and Related Materials*, vol. 17, no. 2, p. 105, 2008.

[185] S. Jin and T. Moustakas, "Effect of nitrogen on the growth of diamond films," *Applied Physics Letters*, vol. 65, no. 4, p. 403, 1994.

[186] K. Moazed, R. Nguyen, and J. R. Zeidler, "Ohmic contacts to semiconducting diamond," *IEEE Electron Device Letters*, vol. 9, no. 7, p. 350, 1988.

[187] T. Tachibana, B. E. Williams, and J. T. Glass, "Correlation of the electrical properties of metal contacts on diamond films with the chemical nature of the metal-diamond interface. II. titanium contacts: A carbide-forming metal," *Physical Review B*, vol. 45, no. 20, p. 11975, 1992.

[188] G. Parrini, S. Lagomarsino, A. Scorzoni, F. Fabbrizzi, S. Sciortino, and L. Nunziati, "Laser graphitization for polarization of diamond sensors," *PoS*, p. 017, 2011.

[189] D. Malta, J. Von Windheim, and B. Fox, "Comparison of electronic transport in boron-doped homoepitaxial, polycrystalline, and natural single-crystal diamond," *Applied Physics Letters*, vol. 62, no. 23, p. 2926, 1993.

[190] I.-N. Lin, S. Koizumi, J. Yater, and F. A. M. Koeck, "Diamond electron emission," *MRS Bulletin*, vol. 39, p. 533, jun 2014.

[191] V. S. Robinson, Y. Show, G. M. Swain, R. G. Reifenberger, and T. S. Fisher, "Thermionic emission from surface-terminated nanocrystalline diamond," *Diamond and Related Materials*, vol. 15, no. 10, p. 1601, 2006.

[192] W. F. Paxton, T. Wade, M. Howell, N. Tolk, W. P. Kang, and J. L. Davidson, "Thermionic emission characterization of boron-doped microcrystalline diamond films at elevated temperatures," *Physica Status Solidi A*, vol. 209, no. 10, p. 1993, 2012.

[193] M. Kataoka, C. Zhu, F. A. M. Koeck, and R. J. Nemanich, "Thermionic electron emission from nitrogen-doped homoepitaxial diamond," *Diamond and Related Materials*, vol. 19, no. 2-3, p. 110, 2010.

[194] J. H. Lay, *Nanoscale investigations of the crystal structure and surface electronic properties of polycrystalline boron-doped diamond films*.
PhD thesis, University of Bristol, 2014.

[195] Y.-f. Meng, C.-s. Yan, J. Lai, S. Krasnicki, H. Shu, T. Yu, Q. Liang, H.-k. Mao, and R. J. Hemley, "Enhanced optical properties of chemical vapor deposited single

crystal diamond by low-pressure/high-temperature annealing.," *Proceedings of the National Academy of Sciences*, vol. 105, no. 46, p. 17620, 2008.